STIC FILE COPY

AD-A203 482

# Dynamics of Debris Motion and the Collision
# Hazard to Spacecraft Resulting
# From an Orbital Breakup

V. A. CHOBOTOV, D. B. SPENCER, D. L. SCHMITT,
R. P. GUPTA, and R. G. HOPKINS
Systems and Computer Engineering Division
Engineering Group

and

D. T. KNAPP
Defense and Surveillance Operations
Programs Group
The Aerospace Corporation
El Segundo, CA 90245

January 1988

Final Report

Prepared for

SPACE DIVISION
AIR FORCE SYSTEMS COMMAND
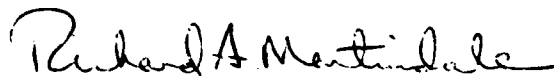Los Angeles Air Force Base
P.O. Box 92960
Los Angeles, CA 90009-2960

DTIC
SELECTE
DEC 2 8 1988
E

This final report was submitted by The Aerospace Corporation, El Segundo, CA 90245, under Contract No. F04701-85-C-0086-P00019 with the Space Division, P.O. Box 92960, Worldway Postal Center, Los Angeles, CA 90009-2960. It was reviewed and approved for The Aerospace Corporation by H. K. Karrenberg, Director, Astrodynamics Department and D. A. Plunkett, Principal Director, ASAT Systems Directorate. The project officer is Major R.A. Martindale, SD/CNA.
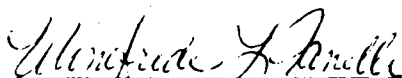
This report has been reviewed by the Public Affairs Office (PAS) and is releasable to the National Technical Information Service (NTIS). At NTIS, it will be available to the general public, including foreign nations.

This technical report has been reviewed and is approved for publication. Publication of this report does not constitute Air Force approval of the report's findings or conclusions. It is published only for the exchange and stimulation of ideas.


RICHARD A. MARTINDALE, Major, USAF
Project Officer
Antisatellite Systems Program Office


FOR THE COMMANDER


WINIFREDE L. FANELLI
Program Manager
Antisatellite Systems Program Office

# REPORT DOCUMENTATION PAGE

| 1a. REPORT SECURITY CLASSIFICATION<br>Unclassified | | | 1b. RESTRICTIVE MARKINGS | | |
|---|---|---|---|---|---|
| 2a. SECURITY CLASSIFICATION AUTHORITY | | | 3. DISTRIBUTION/AVAILABILITY OF REPORT<br>Approved for public release, distribution is unlimited | | |
| 2b. DECLASSIFICATION/DOWNGRADING SCHEDULE | | | | | |
| 4. PERFORMING ORGANIZATION REPORT NUMBER(S)<br>TOR-0086A(2430-02)-1 | | | 5. MONITORING ORGANIZATION REPORT NUMBER(S)<br>SD-TR-88-96 | | |
| 6a. NAME OF PERFORMING ORGANIZATION<br>The Aerospace Corporation | | 6b. OFFICE SYMBOL<br>(If applicable) | 7a. NAME OF MONITORING ORGANIZATION<br>Space Division<br>Air Force Systems Command | | |
| 6c. ADDRESS (City, State, and ZIP Code)<br>2350 E. El Segundo Blvd.<br>El Segundo, CA 90245-4691 | | | 7b. ADDRESS (City, State, and ZIP Code)<br>Los Angeles Air Force Base<br>P. O. Box 92960<br>Los Angeles, CA 90009-2960 | | |
| 8a. NAME OF FUNDING/SPONSORING ORGANIZATION<br>Space Division | | 8b. OFFICE SYMBOL<br>(If applicable) | 9. PROCUREMENT INSTRUMENT IDENTIFICATION NUMBER<br>F04701-85-C-0086-P00019 | | |
| 8c. ADDRESS (City, State, and ZIP Code)<br>See 7b | | | 10. SOURCE OF FUNDING NUMBERS | | |

| | | | PROGRAM ELEMENT NO. | PROJECT NO. | TASK NO. | WORK UNIT ACCESSION NO. |
|---|---|---|---|---|---|---|
| | | | | | | |

11. TITLE (Include Security Classification)
Dynamics of Debris Motion and the Collision Hazard to Spacecraft Resulting from an Orbital Breakup

12. PERSONAL AUTHOR(S)
Chobotov, V.A.; Spencer, D.B.; Schmitt, D.L.; Gupta, R.P.; Hopkins, R.G.; Knapp, D.T.

| 13a. TYPE OF REPORT<br>Final | 13b. TIME COVERED<br>FROM 1985 TO 1987 | 14. DATE OF REPORT (Year, Month, Day)<br>January 1988 | 15. PAGE COUNT<br>162 |
|---|---|---|---|

16. SUPPLEMENTARY NOTATION

| 17. | COSATI CODES | | 18. SUBJECT TERMS (Continue on reverse if necessary and identify by block number) |
|---|---|---|---|
| FIELD | GROUP | SUB-GROUP | Space debris,   Orbital collision; |
| | | | Hypervelocity collision,   Breakup modeling, (eac) |
| | | | Orbital explosions, |

19. ABSTRACT (Continue on reverse if necessary and identify by block number)

This report presents the results of studies conducted at The Aerospace Corporation concerning the dynamics of orbital breakups of space objects and the resultant hazards to spacecraft. Topics considered include the dynamics of orbiting debris clouds, analytical spacecraft breakup models, and the description of program DERBIS which was developed to determine the collision hazard to resident space objects after an orbital breakup event. Keywords: Computer programs; Fragmentation.

| 20. DISTRIBUTION/AVAILABILITY OF ABSTRACT<br>☒ UNCLASSIFIED/UNLIMITED ☐ SAME AS RPT. ☐ DTIC USERS | 21. ABSTRACT SECURITY CLASSIFICATION<br>Unclassified | |
|---|---|---|
| 22a. NAME OF RESPONSIBLE INDIVIDUAL<br>Richard A. Martindale, Major, USAF | 22b. TELEPHONE (Include Area Code)<br>(213) 643-0234 | 22c. OFFICE SYMBOL<br>SD/CNA |

**DD FORM 1473, 84 MAR**       83 APR edition may be used until exhausted.
All other editions are obsolete.

A

## ACKNOWLEDGMENTS

| Accession For | | |
|---|---|---|
| NTIS GRA&I | ☑ | |
| DTIC TAB | ☐ | |
| Unannounced | ☐ | |
| Justification | | |
| By | | |
| Distribution/ | | |
| Availability Codes | | |
| Dist | Avail and/or Special | |
| A-1 | | |

QUALITY INSPECTED 2

1

CONTENTS

CONTENTS (Continued)

CONTENTS (Concluded)

FIGURES

FIGURES (Concluded)

# TABLES

# 1. INTRODUCTION

In support of Space Division's concern about the safety of orbiting pay-
loads, the Space Hazards Section of the Astrodynamics Department was tasked to
develop an analytical model for debris analysis after an orbital breakup. The
results of the model were to be used in developing a computer program which
could examine the collision hazard to any spacecraft from the cloud of parti-
cles resulting from an orbital breakup. The study activity consisted of
defining the requirements, examining the available hypervelocity impact data,
and developing the appropriate breakup models which could be used to determine
the fragment population and velocity distributions for particles in orbiting
debris clouds.

Section 2 and Appendix A, written by V.A. Chobotov, derive the analytical
model for the debris cloud, assuming a breakup or a collision with a space
object in a circular orbit. Linearized equations for relative motion are used
to determine the shape and volume of the debris cloud for an initially iso-
tropic distribution of particle spread velocities. Spatial density is obtained
for two representative breakup models and the collision probability of a parti-
cle and a resident space object determined. The effects of earth's oblateness
on the long-term evolution of the cloud are examined.

Section 3, written by D.B. Spencer, compares the exact with the linear
approximation results from Section 2. It is shown that the linear approxima-
tion solution generally is valid for the case of low particle spread velocities
($\leq$ 100 ft/sec). For greater velocities ($\geq$ 1000 ft/sec), the radial and
tangential position components for orbital plane ejections begin to deteriorate
as time increases. The differences between the exact and linear solutions for
particle trajectories are illustrated.

In Section 4, also written by D.B. Spencer, the volume of the debris
cloud is reexamined with the inclusion of earth's oblateness and atmospheric

11

drag effects. Time-dependent functions are derived which model the changes in the cloud profile as the result of such perturbations. These functions are inputs also to the "DEBRIS" computer simulation which was developed at The Aerospace Corporation for the collision hazard assessment purpose.

Section 5 and Appendix B, contributed by D.L. Schmitt, describe a method for determining the masses and velocities of fragments resulting from a hyper-velocity collision in orbit and compute their orbital parameters. Tabular data are given showing the percentages of fragments that reenter or stay in orbit. Plots of orbital distributions and reentry footprints are illustrated.

Section 6, written by R.P. Gupta, generalizes the fragment mass and velocity computation described in Section 5. The methodology presented in Section 6 can be used to determine number, mass, size, and velocity distribution of fragments for different mass ratios of impacting objects and includes the effects of energy loss due to heat and light generated by impact.

Section 7, authored by D.T. Knapp, develops a new and more flexible model for spacecraft collisions. A system of transfer functions characterizes the collision in terms of the incident object masses and velocities and a set of parameters defined to reflect the several degrees of freedom of the system constrained by conservation of mass, momentum, and energy. This allows sampling of many parametric values for a statistical or sensitivity analysis of the system. Referred to as the Kinematic Model, it overcomes significant limitations of earlier models. It has been used by The Aerospace Corporation to model tests involving on-orbit collisions, and its results have been verified by test data.

In Section 8, contributed by R.G. Hopkins, the description of the program DEBRIS is provided. The program determines the intervals during which a space-craft travels through an expanding cloud and calculates the probability of collision associated with each transit.

12

Finally, Section 9, written by D.B. Spencer, examines the effects of orbital eccentricity on the volume of the debris cloud. Small values of eccentricity are added to the originally circular orbit of the disintegrating body (as was assumed in Section 2); by using a differential correction process, the changes in the cloud volume are determined.

In summary, the results presented in this report represent the theoretical background and description of the DEBRIS program development which can be used to assess the collision hazard for resident space objects following a breakup or a collision of an object in orbit.

# 2. DYNAMICS OF DEBRIS AND THE CONSEQUENCES OF ON-ORBIT BREAKUPS

## 2.1 INTRODUCTION

Continuous use of space over the last 30 years has built up a large number of objects in orbit, the majority of which were generated by explosions of spacecraft or rocket stages. Late 1970s studies at the Johnson Space Center concluded that fragments from collisions between space objects would be a major source of debris (Ref. 1). Studies at The Aerospace Corporation examined the collision hazard to operational spacecraft from space debris including the effects of position uncertainty on the probability of collision between any two objects in orbit (Ref. 2). Other studies, described in Reference 3, considered the distribution of some 5000 NORAD Catalog objects as a function of altitude and orbital inclination. Encounter parameters such as miss distance and relative velocity were examined by computer simulation for low-altitude and geosynchronous orbit spacecraft. Representative space shuttle and geosynchronous mission collision probabilities were determined.

One of the early studies which addressed the evolution of a fragment cloud in orbit is discussed in Reference 4. In that study, the time and place of a satellite disintegration were determined from the orbits of the individual particles (fragments) obtained by observation. Methods of statistical mechanics also were used to study the evolution of the fragment cloud by treating the fragments as an ensemble of noninteracting particles. The spatial density was calculated as a function of position, time, and initial velocity distribution.

This study considers the problem of debris cloud evolution by examining representative particle trajectories. Linearized equations for relative motion in orbit are used to obtain the trajectories of particles with specified initial velocity distributions in three orthogonal planes. The volume of the cloud is computed analytically as a function of time, and the spatial density is calculated for representative breakup models. Long-term effects due to earth's oblateness are evaluated, and the near- and long-term collision hazards for representative spacecraft are examined.

15

## 2.2 ANALYSIS

Consider an explosion or a collision event in a circular orbit such as that illustrated in Figure 1. An orbiting orthogonal reference frame xyz is centered at the origin of the event at time t = 0 such that x is directed opposite to the orbital velocity vector, y is directed along the outward radius, and z completes the triad (along the normal to the orbit plane). The linearized rendezvous equations (Ref. 5) can be used to determine the position of a particle leaving the origin of the coordinate frame with a velocity $\Delta v$; they are of the form

$$
\left.
\begin{aligned}
x &= \left( \frac{-3\theta}{\omega} + \frac{4}{\omega} \sin \theta \right) \dot{x}_o + \frac{2}{\omega}(1 - \cos \theta) \dot{y}_o \\[2em]
y &= \frac{2}{\omega}(\cos \theta - 1) \dot{x}_o + \frac{\dot{y}_o}{\omega} \sin \theta \\[2em]
z &= \frac{\dot{z}_o}{\omega} \sin \theta
\end{aligned}
\right\} \tag{1}
$$

where $\Delta v = (\dot{x}_o^2 + \dot{y}_o^2 + \dot{z}_o^2)^{1/2}$.
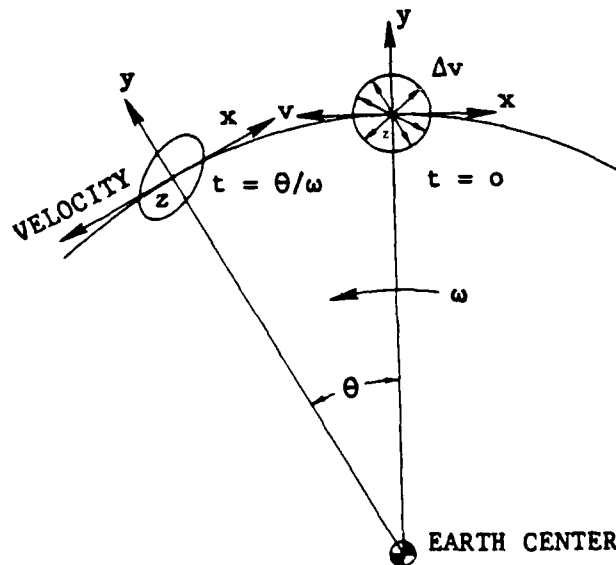


Figure 1. Cloud Dynamics

16

The x,y,z coordinates represent particle position at time $t = \theta/\omega$, where $\theta$ is the in-orbit plane angle and $\omega$ is the angular rate of the circular orbit. The $\dot{x}_0$, $\dot{y}_0$, $\dot{z}_0$ terms are initial velocity components imparted to the particle along the x,y,z axes, respectively. It is assumed that $\Delta v \ll v$.

Equation (1) can be normalized with respect to $\Delta v/\omega$ as follows:

$$\frac{x\omega}{\Delta v} = (-3\theta + 4 \sin \theta)h + 2(1 - \cos \theta)r$$

$$= X$$

$$\frac{y\omega}{\Delta v} = 2(\cos \theta - 1)h + (\sin \theta)r$$

$$= Y \qquad\qquad\qquad (2)$$

$$\frac{z\omega}{\Delta v} = n \sin \theta$$

$$= Z$$

where

$$h = \dot{x}_0/\Delta v, \quad r = \dot{y}_0/\Delta v, \quad n = \dot{z}_0/\Delta v, \quad \text{and} \quad h^2 + r^2 + n^2 = 1 \qquad (3)$$

In matrix form

$$\begin{Bmatrix} X \\ Y \\ Z \end{Bmatrix} = \begin{bmatrix} a_{11} & a_{12} & a_{13} \\ a_{21} & a_{22} & a_{23} \\ a_{31} & a_{32} & a_{33} \end{bmatrix} \begin{Bmatrix} h \\ r \\ n \end{Bmatrix}$$

$$= [M] \begin{Bmatrix} h \\ r \\ n \end{Bmatrix} \qquad\qquad\qquad (4)$$

where

$a_{11} = (-3\theta + 4 \sin \theta)$  $\qquad a_{12} = 2(1 - \cos \theta)$  $\qquad a_{13} = 0$

$a_{21} = 2(\cos \theta - 1)$  $\qquad a_{22} = \sin \theta$  $\qquad a_{23} = 0$

$a_{31} = 0$  $\qquad a_{32} = 0$  $\qquad a_{33} = \sin \theta$

Equations (4) can be plotted as a function of $\theta$ for different values of h, r, and n satisfying condition (3). If, for example, the initial velocity

17

$\Delta v$ distribution for the particles is circular in the x,y plane, then h = cos $\Delta\phi$, r = sin $\Delta\phi$, $0 \leq \Delta\phi \leq 360°$, and $h^2 + r^2 = 1$ with n = 0. The resultant cloud outline is illustrated in Figure 2 for several values of $\theta$.
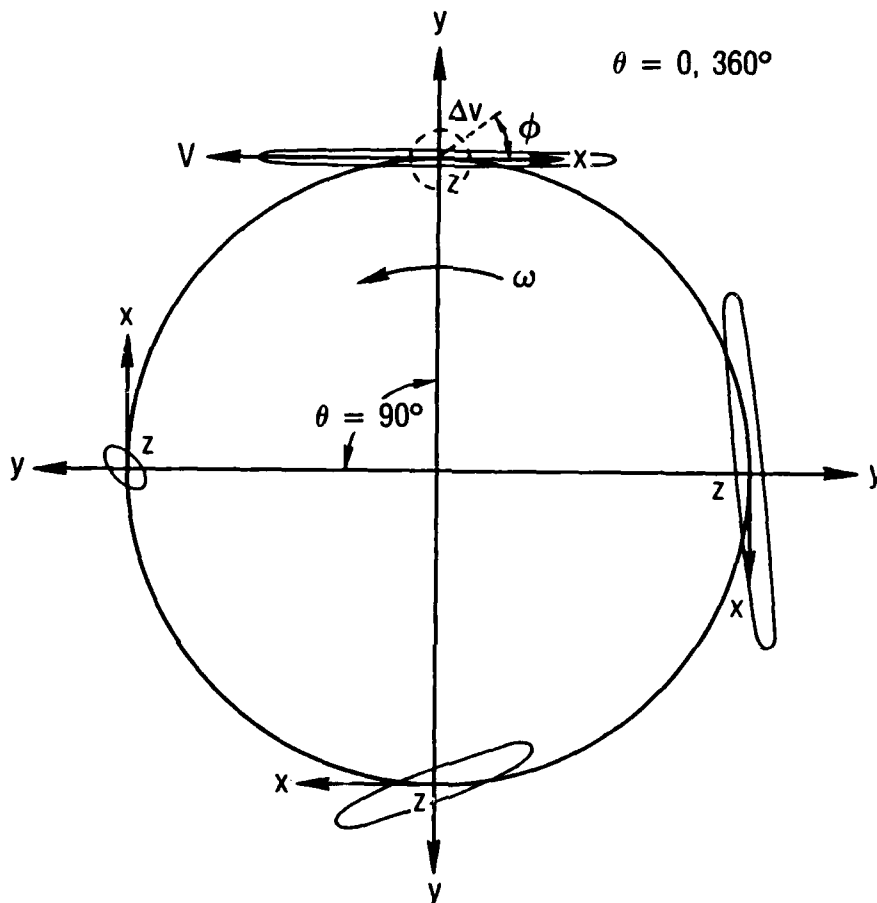


Figure 2. Debris Cloud in Orbit Plane

Representative cloud outlines in nondimensional units are shown in Figure 3. This figure illustrates the cloud outlines in the plane of the orbit (xy) at four different times after breakup. The straight line configuration results after one revolution (period of the nominal circular orbit). It shows that an equal number of particles are leading and lagging as expected from the uniform velocity distribution assumed initially at $\theta = 0°$.
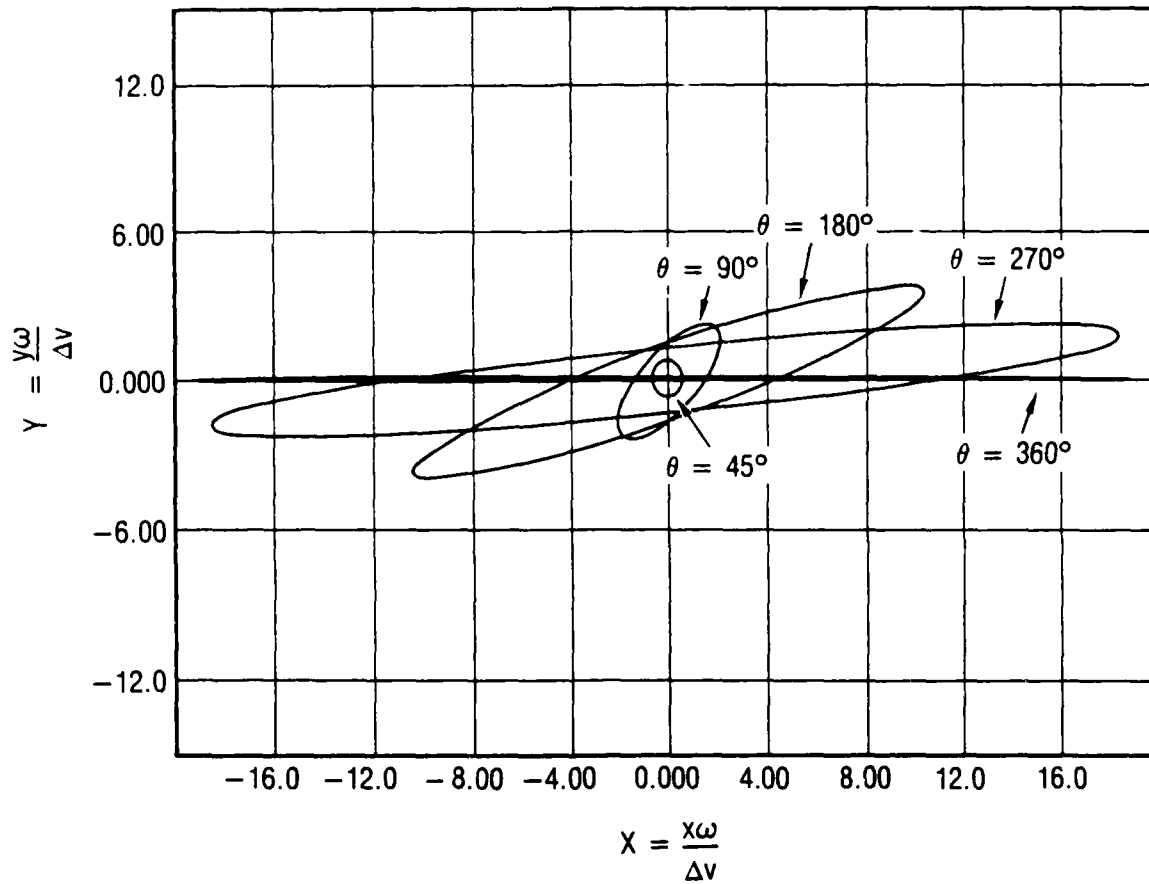
Figure 3. Cloud Contours in Orbit Plane (to scale)

For a velocity distribution that is circular in the xz plane, the cloud outlines in Figure 4 represent the contours in the cross-track (xz) plane. A straight line configuration occurs at $\theta = 180°$ and $360°$ where all particles cross the orbit plane.
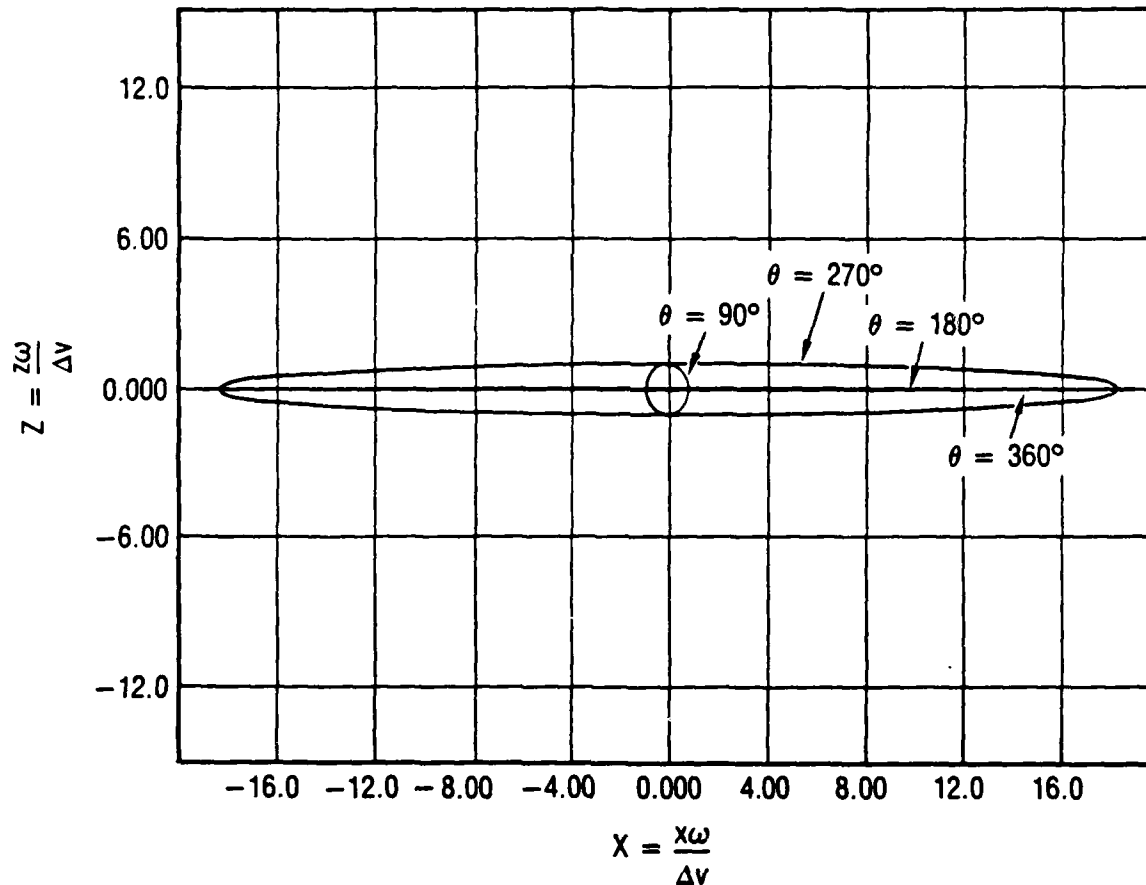
Figure 4. Cloud Contours in Cross-Track Plane (to scale)

## 2.3 VOLUME OF DEBRIS CLOUD

The volume of the debris cloud can be expressed analytically in terms of the elements of the transition matrix M in Eq. (4). If, for example, h,r,n are the orthogonal components of a sphere of unit radius, then the determinant of M represents the volume of the cloud at any time $t = \theta/\omega$. The positive cloud volume, normalized to $(\Delta v/\omega)^3$, is of the form

$$\text{VOLUME} = \frac{4\pi}{3} |\det [M]|$$

$$= \frac{4\pi}{3} |(ad + b^2)d| \qquad (5)$$

20

where $a = a_{11}$, $b = a_{12}$, $d = a_{22}$, and where $4\pi/3$ is the volume of a unit sphere. A further discussion of this theory is presented in Appendix A. Equation (5) is plotted in Figure 5 where a linear approximation for the volume also is shown.

In units of $(\Delta v/\omega)$, the volume becomes

$$VOL = VOLUME \ (\frac{\Delta v}{\omega})^3 \tag{6}$$
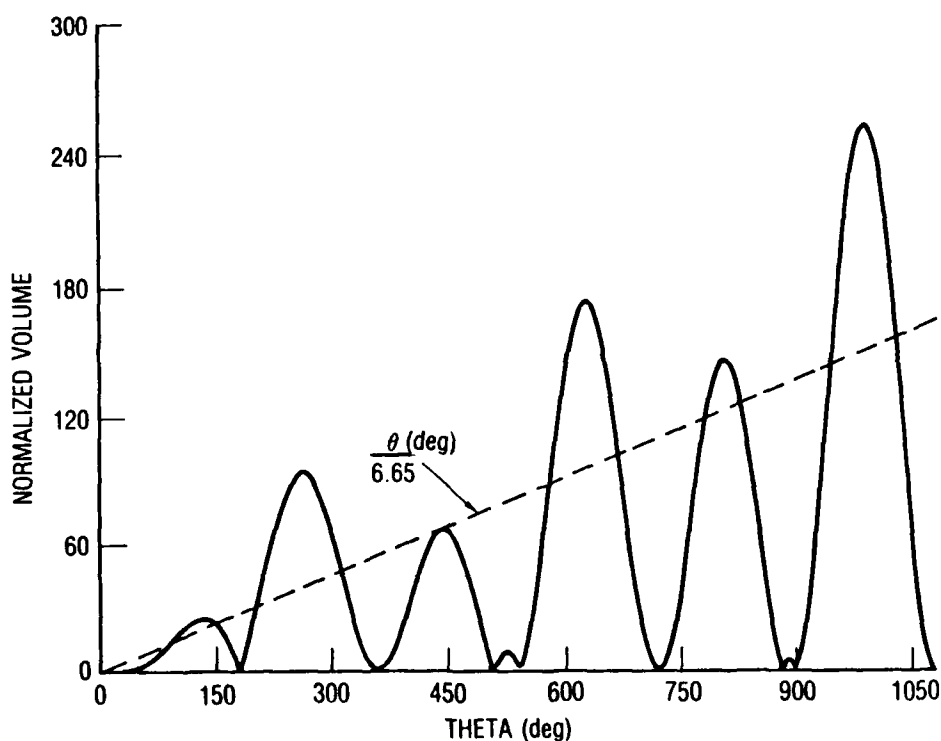


Figure 5. Cloud Volume versus Time

For a circular, low-altitude orbit with $\Delta v$ = 100 and 200 m/s and $\omega = 1.1 \times 10^{-3} \ s^{-1}$, the volume of the debris cloud is illustrated in Figure 6. Note that the volume vanishes at the integral values of $\theta = 2\pi$ and $\theta = \pi$ and for $\theta$ between 500° and 550° and again near $\theta$ = 900°. The latter zeros are

21

caused by the area of the cloud in the orbit (xy) plane collapsing to a line due to the linearization of the equations of motion. A condition that the area not vanish anywhere except at $\theta = 0$, $\pi$, $2\pi$, et cetera, can be satisfied by

$$ad + b^2 > 0 \tag{7}$$

or

$$|ad| + b^2 > 0 \tag{8}$$

which results in the cloud volume function shown in Figure 7 generated using Eq. (5) with $ad > 0$, which ensures that the condition (8) is always satisfied. This approximation for the cloud volume improves as $\theta$ increases when

$$|ad| \gg b^2 \tag{9}$$

## 2.4    SPATIAL DENSITY

Assuming uniform distribution of the particles in the cloud, the number of which is to be determined later, the density is of the form

$$\rho = N/VOL \tag{10}$$

where N is the number of particles in the cloud. The accuracy of this result is reasonably good for low values of the particle spread velocities (e.g., $\Delta v \leq 100$ m/s).

A "mean" value for $\rho$ may, for example, be obtained approximately as

$$\rho_{av} \approx \frac{N}{(VOL)_{av}} \tag{11}$$

where

$$(VOL)_{av} = \frac{\theta(deg)}{6.65} \left(\frac{\Delta v}{\omega}\right)^3$$

22
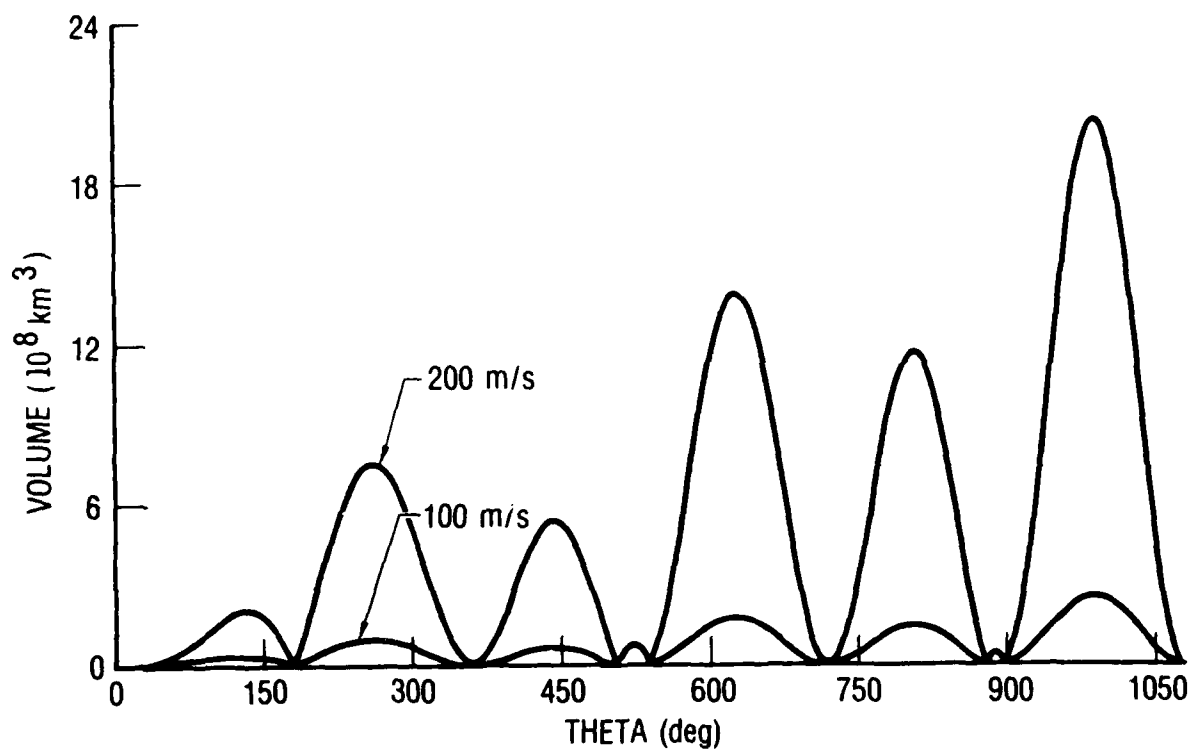
Figure 6. Cloud Volume in Low Earth Orbit
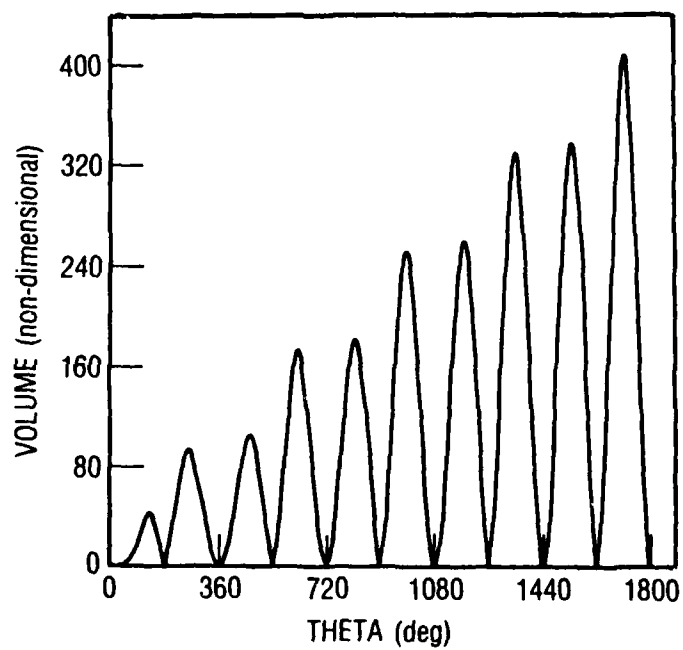


Figure 7. Cloud Volume versus Time (corrected)

23

is an arbitrarily assumed linear function of $\theta$, as can be seen from Figure 5. The volume of the initial spherical cloud in this case increases linearly with time. Such an approximation is valid up to a quarter revolution ($\theta = 90°$) when the "mean" volume is

$$(VOL)_{av} = 13.53 \left(\frac{\Delta v}{\omega}\right)^3 \tag{12}$$

Thus, for example, if $\Delta v = 100$ m/s, $\omega = 1.1 \times 10^{-3}$ s$^{-1}$, then

$$(VOL)_{av} = 1.016 \times 10^7 (km)^3 \tag{13}$$

For $\Delta v = 200$ m/s, the volume is a factor of $(2)^3$ greater. For $\Delta v = 100$ m/s, the spherical cloud diameter at 1/4 revolution ($\theta = 90°$) is 269 km which compares with 285 km if obtained as a linear function of $\Delta v$.


## 2.5 SHORT-TERM COLLISION HAZARD

The probability that a spacecraft will collide with a fragment while passing through a debris cloud is proportional to the spatial density in the cloud, $\rho_{av}$, spacecraft projected area, A, spacecraft velocity relative to the cloud, $V_R$, and the time, t, spent in the cloud. Thus

$$p(col) = \rho_{av} A V_R t \tag{14}$$

where $p(col)$ = collision probability per pass.

The product $V_R t$ is the path length through the cloud. It is the diameter D of a spherical cloud for a spacecraft passing through the center of the cloud. The probability of collision, then, is of the form

$$p(col)/A = \rho_{av} D \tag{15}$$

24

where

$$D = \sqrt[3]{\frac{6(VOL)_{av}}{\pi}}$$

Evaluation of Eq. (15) requires knowledge of N and $\Delta v$ to obtain $\rho_{av}$ and $(VOL)_{av}$. Laboratory hypervelocity impact experiments, such as are described in Reference 6, for example, have shown that the number versus size distribution for ejecta fragments is of the form

$$N = 0.4478\left(\frac{M}{M_e}\right)^{-0.7496} \tag{16}$$

where N is the cumulative number of ejecta with mass M or greater and $M_e = M_p v^2$ where $M_p$ is the mass of the smaller body (projectile) and v is the collision velocity.

Equation (16) and Figure 8 from Reference 6, which illustrate fragment velocity distribution from one laboratory test with an impact velocity of 3.5 km/s, were used to obtain the distributions of fragments in Table 1 from an assumed collision of two objects in orbit. Each of the three clouds corresponds to a different particle size.

A second distribution is illustrated in Table 2 which specifies a range of particle sizes for each spread velocity group.

The probability of collision of a spacecraft and a debris particle based on Eq. (15) is shown in Figure 9. The curves labeled NASA and Aerospace correspond to the distributions of debris particles in Tables 1 and 2, respectively.

The results show that the collision hazard decreases rapidly after the event ($\theta = 0$ in Fig. 9), but that the magnitude of the hazard is greatly dependent on the assumed distribution. The probabilities for each of the three cloud distributions in Tables 1 and 2 were added to obtain the results in Figure 9.

25
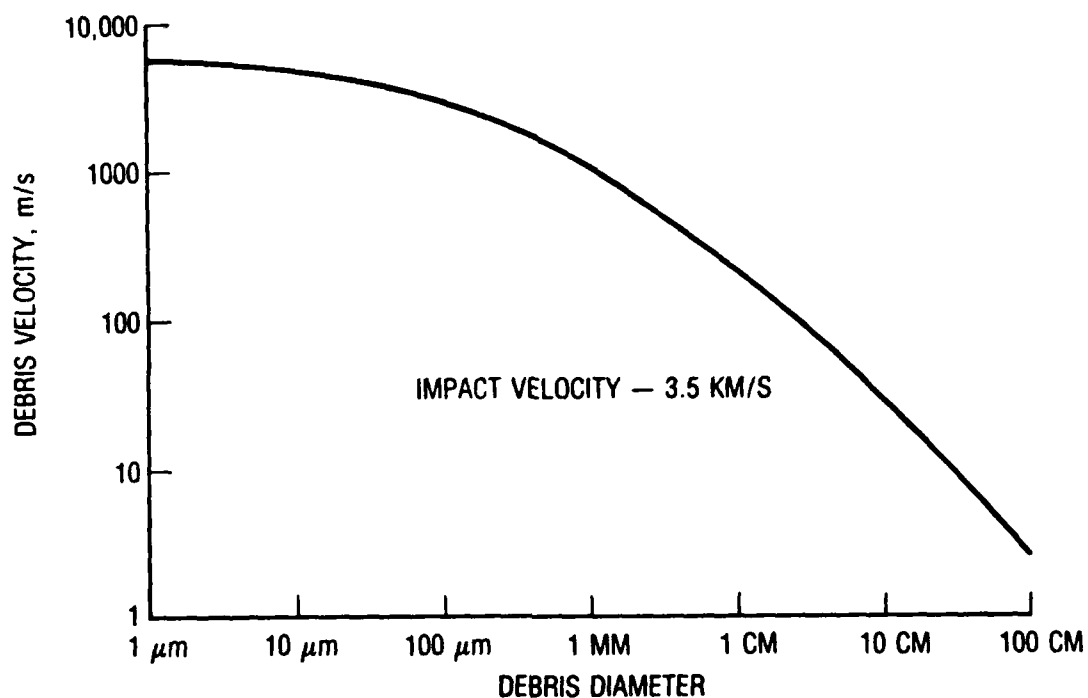
Figure 8. Velocity Distribution (Ref. 6)


Table 1. NASA--Velocity Distribution

| Cloud | Number of Particles (N) | Spread Velocity $\Delta v(m/s)$ | Particle Size d(cm) |
|-------|-------------------------|--------------------------------|---------------------|
| 1     | 200                     | 20                             | 10                  |
| 2     | 20000                   | 200                            | 1                   |
| 3     | 3000000                 | 1000                           | 0.1                 |


Table 2. The Aerospace Corporation--Velocity Distribution (Kinematic model)

| Cloud | Number of Particles (N) | Spread Velocity $\Delta v(m/s)$ | Particle Size d(cm) |
|-------|-------------------------|--------------------------------|---------------------|
| 1     | 200000                  | 0 to 100                       | 0.1 to 120          |
| 2     | 500000                  | 0 to 800                       | 0.1 to 60           |
| 3     | 1000000                 | 0 to 2000                      | 0.1 to 6            |

0.000012

0.00001

8E-6

6E-6

4E-6

2E-6

0

PROBABILITY/UNIT AREA (m$^2$)

AEROSPACE

NASA

0     150    300    450    600    750    900    1050

THETA (deg)
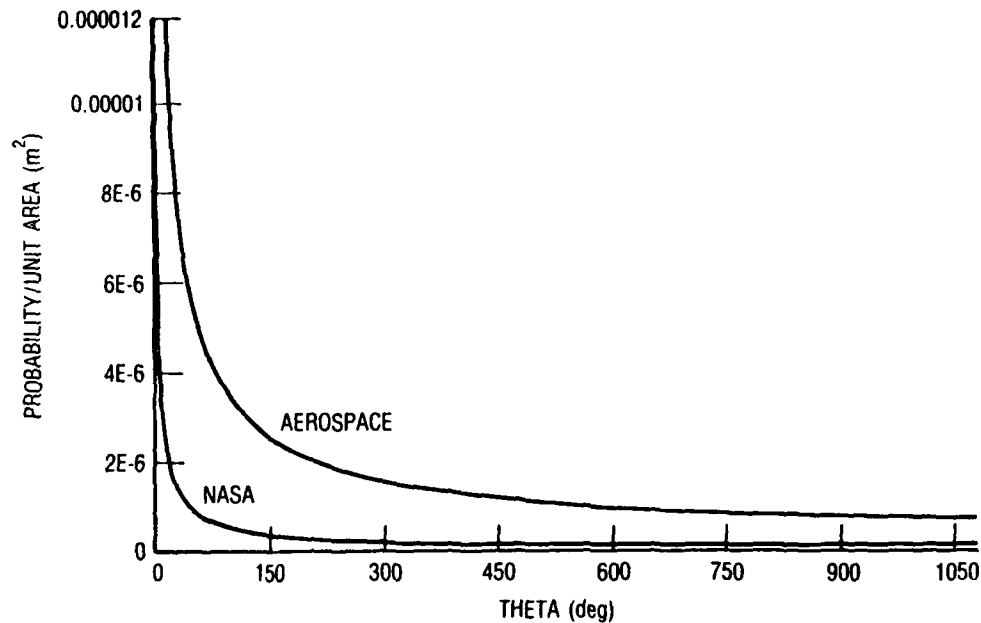
Figure 9.   Probability of Collision per Pass

## 2.6   LONG-TERM EFFECTS

The debris particles in the cloud tend to spread along the circumference of the nominal orbit, in time assuming the shape of a torus with two "pinch" points as illustrated in Figure 10. The pinch points result from the orbital intersections of the debris particles where, theoretically, the volume of the cloud becomes zero. All particles pass through the point of disintegration ($\theta = 0$) at different times. They also pass through the orbit plane at $\theta = 180°$ along a line on the radius vector. The probability of collision near the pinch points can be much greater where the cloud volume initially is very small. The effect of orbit perturbations (e.g., earth's oblateness, air drag, etc.) is to slowly increase the volume at the pinch points and thus decrease the probability of collision. In the long term, the motion of the line of apsides and nodal drift tend to widen the pinch points and spread the cloud envelope until it completely envelops the earth. In this steady-state condition, the collision hazard is reduced to a minimum and can be compared with the existing background environment, i.e., micrometeoroids, man-made debris, and so forth. An evaluation of the apsidal and nodal drifts is considered in the following sections.

27
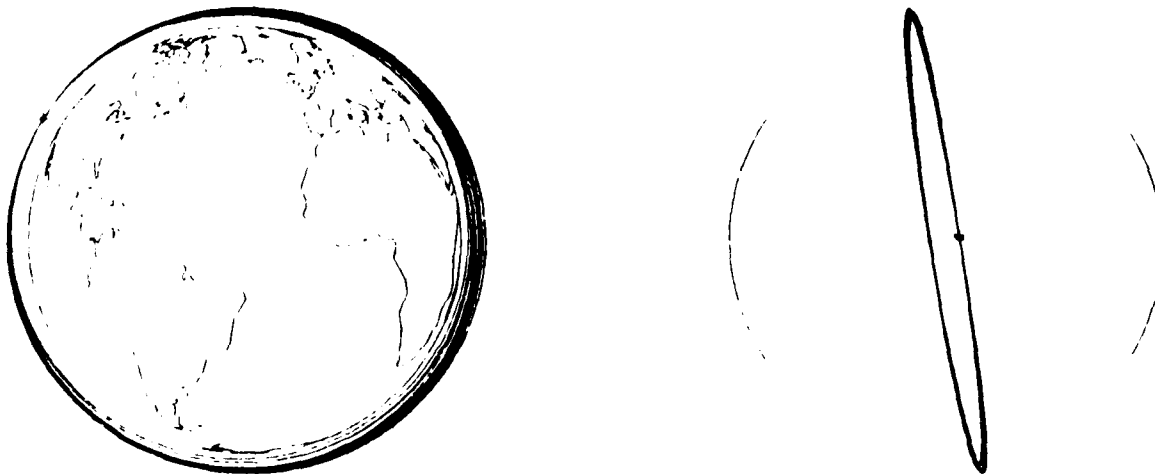
Figure 10. Representative Orbits of a Number of Debris Particles

## 2.7 CLOUD STRUCTURE

If the particles' individual orbital parameters are unknown, the expected mean values for these parameters can be obtained probabilistically for any specified spread velocity distribution. A change in the particle semi-major axis $\Delta a$ can be computed as a function of the spread velocity vector, $\Delta \vec{v}$, and the orbital velocity $\vec{v}$ geometry. This can be done from a functional relationship between $\Delta a$, $\Delta v$, and $\phi$, the angle between $\vec{v}$ and $\Delta \vec{v}$, as follows.

Consider the specific energy of a particle orbit of the form

$$E = - \frac{\mu}{2a} \tag{17}$$

where $\mu$ = gravitational constant. Taking differentials

$$\Delta E = \frac{\mu \, \Delta a}{2a^2}$$

$$= \frac{-E}{a} \Delta a \tag{18}$$

28

and

$$\frac{\Delta E}{E} = \frac{-\Delta a}{a} \qquad (19)$$

This equation requires an explicit expression for $\Delta E$ which is the change in the particle orbit energy as a result of the change in its velocity $\vec{\Delta v}$. This is of the form

$$\Delta E = \frac{1}{2}(\vec{v} + \vec{\Delta v})^2 - \frac{1}{2}(\vec{v})^2$$

$$= \frac{1}{2}(\vec{v} + \vec{\Delta v}) \cdot (\vec{v} + \vec{\Delta v}) - \frac{\vec{v} \cdot \vec{v}}{2}$$

$$= v \, \Delta v \, \cos \phi + \frac{(\Delta v)^2}{2}$$

$$\approx v \, \Delta v \, \cos \phi \qquad \text{for } \frac{\Delta v}{v} \ll 1 \qquad (20)$$

Thus, from Eqs. (17) and (18)

$$\frac{\Delta E}{E} = -\frac{\Delta a}{a}$$

$$\approx \frac{v \, \Delta v \, \cos \phi}{E} \qquad \text{for } \frac{\Delta v}{v} \ll 1$$

$$= \frac{2av \, \Delta v \, \cos \phi}{-\mu} \qquad (21)$$

or

$$\frac{\Delta a}{2a} \approx \frac{av \, \Delta v \, \cos \phi}{\mu}$$

$$\approx \frac{\Delta v}{v} \cos \phi \qquad (22)$$

since $v = (\mu/a)^{1/2}$.

A general approximate relationship between $\Delta a$, $\Delta v$, and $\phi$ for small values of $\delta v$, therefore, is of the form

$$\delta a \approx \delta v \, \cos \phi \qquad (23)$$

where

$$\delta a = \frac{\Delta a}{2a}$$

$$\delta v = \frac{\Delta v}{v}$$

Equation (23) describes the internal structure of the cloud. For an exact relationship, the $(\Delta v)^2/2$ term in Eq. (20) must be retained.

## 2.8 PROBABILITY DISTRIBUTION

The functional relationship between $\Delta v$, $v$, and $\phi$ expressed in Eq. (23) is plotted in Figure 11. Equation (23) or Figure 11 can be used to obtain
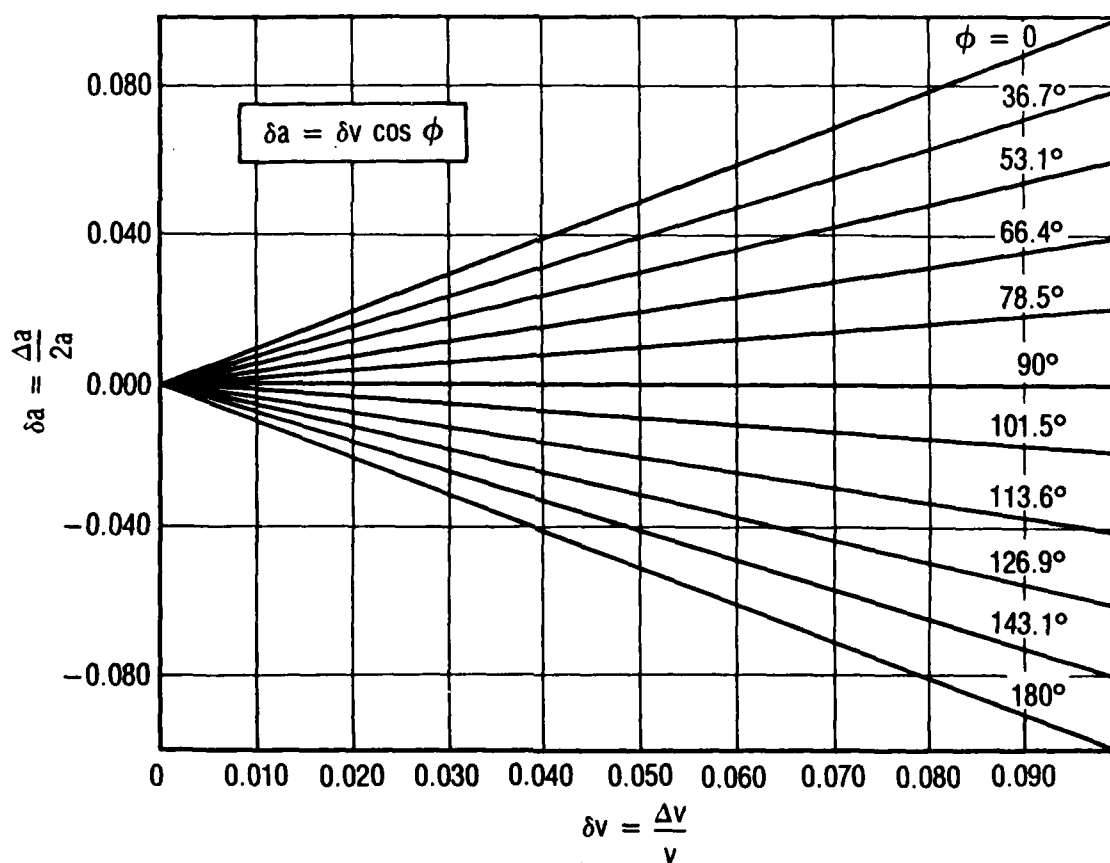


Figure 11. Internal Structure of Cloud

30

orbital parameter probability distributions for groups of particles with
specified spread velocity ranges. If, for example, an isotropic spread
velocity distribution is assumed as shown in Figure 12, then the probability
that $\vec{\Delta v}$ will be within an angle $\phi$ of $\vec{v}$ is

$$p = \frac{2A_Z}{A_{SPH}}$$

$$= \frac{4\pi \ v^2 \ (1 - \cos \ \phi)}{4\pi \ v^2}$$

$$= 1 - \cos \ \phi \tag{24}$$

where $A_Z$ is the area of a spherical zone defined by the cone angle $\phi$, and $A_{SPH}$
is the area of the sphere of radius v.
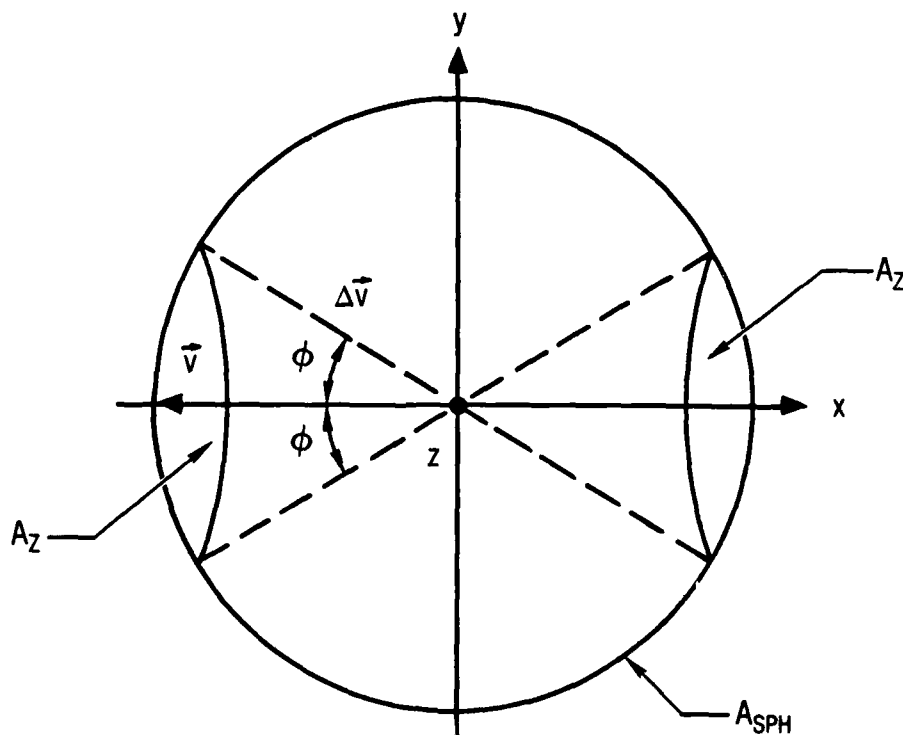


Figure 12. Isotropic Spread Velocity Distribution

Using Eqs. (23) and (24), we find that the probability distribution function is of the form

$$p \approx 1 - \frac{\delta a}{\delta v} \qquad (25)$$

or

$$\delta a = (1 - p)\delta v \qquad (26)$$

Thus, the mean or the "expected" change (corresponding to p = 0.5) in $\delta a$ is

$$\delta a = \pm \frac{\delta v}{2} \qquad (27)$$

where $\pm$ corresponds to whether $\phi$ is less or greater than $\pi/2$. One-half of the particle orbits, therefore, will have a change in the semi-major axes of

$$\langle \Delta a \rangle \approx \pm a\left(\frac{\Delta v}{v}\right) \qquad (28)$$

Equation (25) is plotted in Figure 13 with $\delta v$ as a parameter.
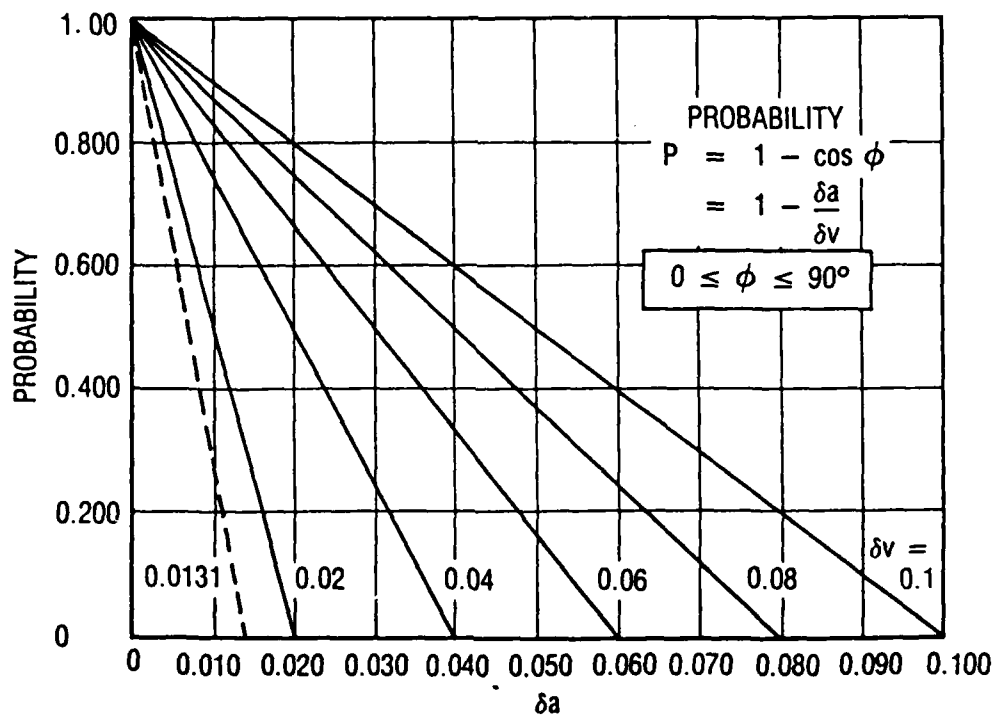


Figure 13. Probability Distribution for $\delta a = \Delta a/2a$

32

## 2.9 EARTH'S OBLATENESS EFFECTS

The primary, long-term orbit perturbation effect on the evolution of the debris cloud is earth's oblateness. The $J_2$ term in the earth's gravitational potential accounts for earth's oblateness and causes apsidal and nodal rotation. This in turn results in a constantly increasing volume of the cloud. In order to determine the cloud growth rate due to $J_2$, it is necessary to determine the inclination i, semi-major axis a, and eccentricity e for each particle orbit. The apsidal rotation $\dot{\omega}$ and nodal regression $\dot{\Omega}$ are then given by the equations

$$\dot{\omega} = K(2 - \frac{5}{2} \sin^2 i) \tag{29}$$

$$\dot{\Omega} = -K \cos i \tag{30}$$

where

$$K = \frac{9.9639}{(1 - e^2)^2} \left(\frac{R_e}{a}\right)^{3.5} \quad \text{deg/day}$$

$$R_e = \text{earth equatorial radius} \tag{31}$$

The initial, pinched ring shape of the cloud (such as is shown in Fig. 10) eventually spreads around the earth due to particle orbit apsidal and nodal rotation effects. The rate at which this steady-state condition is approached can be obtained from the mean expected values $\langle\dot{\omega}\rangle$, $\langle\dot{\Omega}\rangle$ for the apsidal and nodal rotation rates, respectively.

Consider, for example, the case of isotropic spread velocity distribution in a low-altitude circular orbit with the following parameters:

$$
\begin{aligned}
\Delta v &= 100 \text{ m/s} \\
a &= 6924 \text{ km} \\
v &= 7.63 \text{ km/s} \\
i &= 98°
\end{aligned}
\tag{32}
$$

For this case, $\delta v = \Delta v/v = 0.0131$, and the probability density distribution for $\delta a$ is as shown by the dashed line in Figure 14 (see Section 3). From Figure 14 or Eq. (28)

$$\langle \Delta a \rangle = \pm a \, \delta v$$

$$= \pm 90.7 \text{ km} \tag{33}$$

Particles with the positive mean change of the semi-major axis (one-half of all fragments) have orbits with higher energy than that of the parent body, while those with negative have lower energy. The corresponding mean apsidal and nodal rotation rates from Eqs. (24) through (31) are

$$K_{\pm} = 9.963 \left( \frac{R_e}{a \mp \langle a \rangle} \right)^{3.5}$$

$$K+ = 7.79 \text{ deg/day} \tag{34}$$

$$K- = 7.11 \text{ deg/day}$$

$$\langle \dot{\omega}_+ \rangle = 7.79(2 - 2.5 \sin^2 98°)$$

$$= -3.52 \text{ deg/day}$$

$$\langle \dot{\omega}_- \rangle = 7.11(2 - 2.5 \sin^2 98°)$$

$$= -3.21 \text{ deg/day}$$

$$\langle \dot{\Omega}_+ \rangle = -7.79 \cos 98°$$

$$= 1.08 \text{ deg/day}$$

$$\langle \dot{\Omega}_- \rangle = -7.11 \cos 98°$$

$$= 0.989 \text{ deg/day} \tag{35}$$

The relative mean apsidal and nodal rotation rates for the two groups of particles are

$$\langle \Delta \dot{\omega} \rangle = \langle \dot{\omega}_+ \rangle - \langle \dot{\omega}_- \rangle$$

$$= -0.31 \text{ deg/day}$$

$$\langle \Delta \dot{\Omega} \rangle = \langle \dot{\Omega}_+ \rangle - \langle \dot{\Omega}_- \rangle$$

$$= 0.091 \text{ deg/day} \qquad (36)$$

Relative closure of the two groups of particles occurs when $\langle \Delta \dot{\omega} \rangle$ and $\langle \Delta \dot{\Omega} \rangle$ are 180°.

The corresponding mean periods are

$$T_\omega = \frac{180°}{|\langle \Delta \dot{\omega} \rangle|}$$

$$\approx \frac{180°}{0.31} = 581 \text{ days} = 1.6 \text{ years}$$

$$T_\Omega \approx \frac{180°}{\langle \Delta \dot{\Omega} \rangle}$$

$$\approx \frac{180°}{0.091} = 1978 \text{ days}$$

$$= 5.4 \text{ years} \qquad (37)$$

## 2.10  SUMMARY AND CONCLUSIONS

A new and simple method has been described in the report which can be used to examine the short-term collision hazard for a spacecraft passing through a cloud of particles resulting from a breakup of an object in orbit. The method uses linearized equations for relative motion to compute the volume of the cloud of particles as a function of the initial spread velocities, orbital angular rate, and time.

35

A representative short-term collision hazard for a spacecraft passing through the center of the cloud was computed under certain simplifying assumptions. The results showed that the greatest hazard occurs at or shortly after the breakup event when the cloud volume is small and the density large. The collision hazard was found to decrease rapidly with time.

The effects of earth's oblateness on the evolution of the cloud also were examined. The results showed that the initially toroidal debris cloud becomes a spherical shell due to nodal and apsidal rotation effects of the particle orbits.

The long-term collision hazard thus is seen to be greatly reduced over a period of several years. A more general case of a spacecraft entering an expanding debris cloud is considered in Section 8. The probabilities of collision with a particle in the cloud are calculated using program DEBRIS, where the spacecraft path through the cloud is determined and the corresponding probabilities of collision are obtained.

# 3. COMPARISONS OF EXACT AND LINEAR SOLUTIONS

## 3.1  INTRODUCTION

Whenever a dynamical problem is evaluated, the question arises of whether to use the exact equations of motion or the linearized set. The primary concern when using the linearized version is the violation of the assumptions made; for if the assumptions remain valid over the range of interest, then the linearized solution should be an accurate portrayal of what is actually happening. In this section, the dynamical equations of relative motion between two bodies are studied, both the linearized version and exact version, and the solutions are compared for accuracy. Also, when the most accurate of these results is used to determine the position of many particles relative to a rotating reference point, an approximate volume in space can be found which could represent the region of space occupied by debris from an on-orbit breakup of a spacecraft.

## 3.2  ANALYSIS

Assume the satellite in orbit as a point moving in a known gravity field. At any given time, the position and velocity vectors, in an earth-based inertial frame, are known from telemetric measurements. When the orbital breakup begins, a multitude of particles will move away from their previous position (the center of mass, or CM) at some velocity. This is similar to a probe being ejected from a host ship at a known initial velocity. This ejecta now moves in its own, unique orbit.

By propagating the $\vec{\Delta v}$ vector in all directions and in three dimensions, one can determine the maximum distances from the former center of mass. When the debris volume is approximated as a growing torus, as shown in Figure 14, the time-varying volume is approximately equal to

$$V(t) = \frac{\pi}{4} R\left(y_{max} - y_{min}\right)\left(z_{max} - z_{min}\right)\left[\sin^{-1}\left(\frac{x_{max}}{R}\right) - \sin^{-1}\left(\frac{x_{min}}{R}\right)\right] \qquad (38)$$

37

where

$x_{max}$ = maximum distance in the −x direction (leading CM)

$x_{min}$ = maximum distance in the +x direction (trailing CM)

$y_{max}$ = maximum distance in the +y direction (outside CM)

$y_{min}$ = maximum distance in the −y direction (inside CM)

$z_{max}$ = maximum distance in the +z direction (above CM)

$z_{min}$ = maximum distance in the −z direction (below CM)

R    = distance from the center of the earth to CM
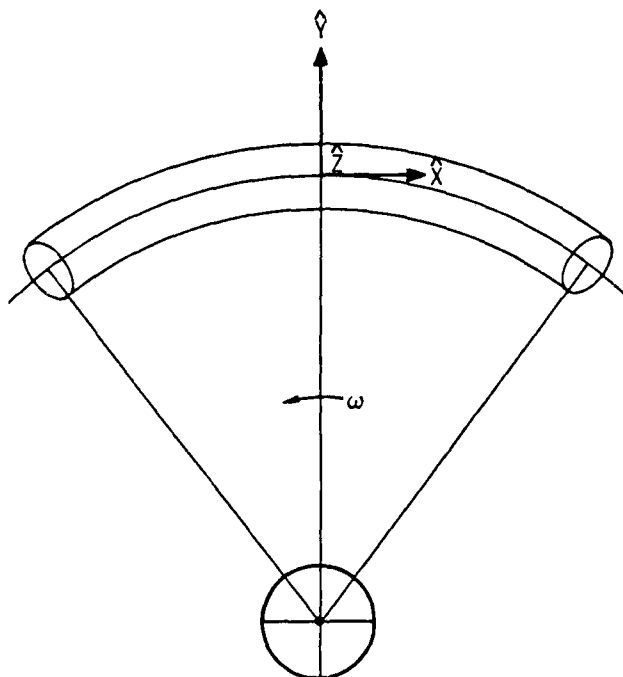
Figure 14.   Torus Model

Analytical expressions, on the other hand, allow for simplified solutions to complex problems.  For circular orbits, an approximate solution describing relative motion between two bodies revolving about the same gravitational attracting mass is the Clohessy-Wiltshire equations.  In matrix form, the analytical solution is

38

$$\begin{Bmatrix} x \\ y \\ z \\ \dot{x} \\ \dot{y} \\ \dot{z} \end{Bmatrix} = \left| \begin{array}{ccc|ccc} 1 & 6(\omega t - \sin \omega t) & 0 & -3t + \dfrac{4}{\omega} \sin \omega t & \dfrac{2}{\omega}(1 - \cos \omega t) & 0 \\ 0 & 4 - 3\cos \omega t & 0 & \dfrac{2}{\omega}(-1 + \cos \omega t) & \dfrac{1}{\omega} \sin \omega t & 0 \\ 0 & 0 & \cos \omega t & 0 & 0 & \dfrac{1}{\omega} \sin \omega t \\ \hline 0 & 6\omega(1 - \cos \omega t) & 0 & -3 + 4\cos \omega t & 2 \sin \omega t & 0 \\ 0 & 3\omega \sin \omega t & 0 & -2 \sin \omega t & \cos \omega t & 0 \\ 0 & 0 & -\omega \sin \omega t & 0 & 0 & \cos \omega t \end{array} \right| \begin{Bmatrix} x_0 \\ y_0 \\ z_0 \\ \dot{x}_0 \\ \dot{y}_0 \\ \dot{z}_0 \end{Bmatrix} \qquad (39)$$

$$\begin{Bmatrix} X \\ \dot{X} \end{Bmatrix} = [\Phi(t,0)] \qquad\qquad\qquad \begin{Bmatrix} X_0 \\ \dot{X}_0 \end{Bmatrix} \qquad (40)$$

Since the particles are at the origin of the coordinate frame at $t = 0$, the initial state vector is

$$\begin{Bmatrix} X_0 \\ \dot{X}_0 \end{Bmatrix} = \{0,\ 0,\ 0,\ \dot{x}_0,\ \dot{y}_0,\ \dot{z}_0\}^T \qquad (41)$$

Thus, if position information is all that is desired, then the system reduces to

$$\begin{Bmatrix} x \\ y \\ z \end{Bmatrix} = \left| \begin{array}{ccc} -3t + \dfrac{4}{\omega} \sin \omega t & \dfrac{2}{\omega}(1 - \cos \omega t) & 0 \\ \dfrac{2}{\omega}(-1 + \cos \omega t) & \dfrac{1}{\omega} \sin \omega t & 0 \\ 0 & 0 & \dfrac{1}{\omega} \sin \omega t \end{array} \right| \begin{Bmatrix} \dot{x}_0 \\ \dot{y}_0 \\ \dot{z}_0 \end{Bmatrix} \qquad (42)$$

$$\{X\} = [\phi_{12}]\ \{X_0\} \qquad (43)$$

where $[\phi_{12}]$ is the submatrix in the upper right-hand position of the transition matrix $\Phi(t,0)$ and is similar to Eq. (4). The volume enclosed in this space is found by the determinant of $\phi_{12}$ multiplied by $4\pi/3$ [an expansion of Eq. (5)]

$$V = \frac{4\pi}{3} \left| \sin \theta \left[ (-3\theta + 4 \sin \theta) \sin \theta + 4(1 - \cos \theta)^2 \right] \right| \left( \frac{\Delta v}{\omega} \right)^3 \qquad (44)$$

39

where $\theta = \omega t$, and $\Delta v$ is the particle relative velocity.

$$\Delta v = (\dot{x}_o^2 + \dot{y}_o^2 + \dot{z}_o^2)^{1/2} \tag{45}$$

Applying what is now known to the problem of on-orbit breakup of a spacecraft, one can determine the range of validity of the Clohessy-Wiltshire equations.

## 3.3 RESULTS

The range of validity can be determined by comparing the effects of many different $\vec{\Delta v}$ vectors on the exact and linear solutions of the problem. In each case studied, the $\Delta v$ vector was propagated in six directions: positive and negative, tangential, radial, and out of plane. The orbit in study is a low-altitude orbit, with an angular rate, $\omega$, of $1.1 \times 10^{-3}$ rad/sec. Allowing the magnitude of $\vec{\Delta v}$ to range from 1 to 1000 ft/sec gave a wide range of results which are summarized below.

A good comparison between the exact and linear solutions is to look at the absolute difference between the two solutions. Figures 15 through 19 show the differences. The ordinate is the log to the base 10 of the deviation in nautical miles, while the abscissa is the number of orbit revolutions.

Figures 15 and 16 are deviations in x versus time and y versus time, respectively, for a radial ejection. The z versus time has been left out, since the out-of-plane component for the linear solution is zero. Generally, for spread velocities less than 100 ft/sec, the maximum deviation is on the order of magnitude of 1 nmi after two orbits. Figures 17 and 18 examine the same scenario, except now, for a tangential (parallel to the velocity vector) ejection. For spread velocities of less than 100 ft/sec, the deviation is on the order of magnitude of 10 nmi after two orbits. The deviation in z is left out for similar reasons as before.

40

Figure 19 is the deviation in z versus time for an out-of-plane ejection. For a spread velocity of 100 ft/sec, the deviation grows to about 0.1 nmi in approximately two orbits.

The comparison of the torus model to the Clohessy-Wiltshire volume model is shown in Figure 20. Clohessy-Wiltshire has a greater volume, generally, over the first orbit. The torus model has two more zero points than the linear model; however, the two models do have their common zero points at approximately the same time.

## 3.4    SUMMARY

For small changes in relative velocities ($\leq$ 100 ft/sec), the Clohessy-Wiltshire equations prove to be adequate for at least the first couple of orbit revolutions. However, as time increases, the equations degrade as the nonlinear terms, previously neglected, begin to have a larger effect. When large velocity changes are considered ($\geq$ 1000 ft/sec), the radial and tangential position components for orbital plane ejections begin to deteriorate quickly as time progresses. However, the out-of-plane component of position for an out-of-plane ejection was quite accurate for both the linear and exact equations.

When considering large time periods (days), however, one must necessarily use the exact equations, since the linear equations are good only for a short time following the ejection.
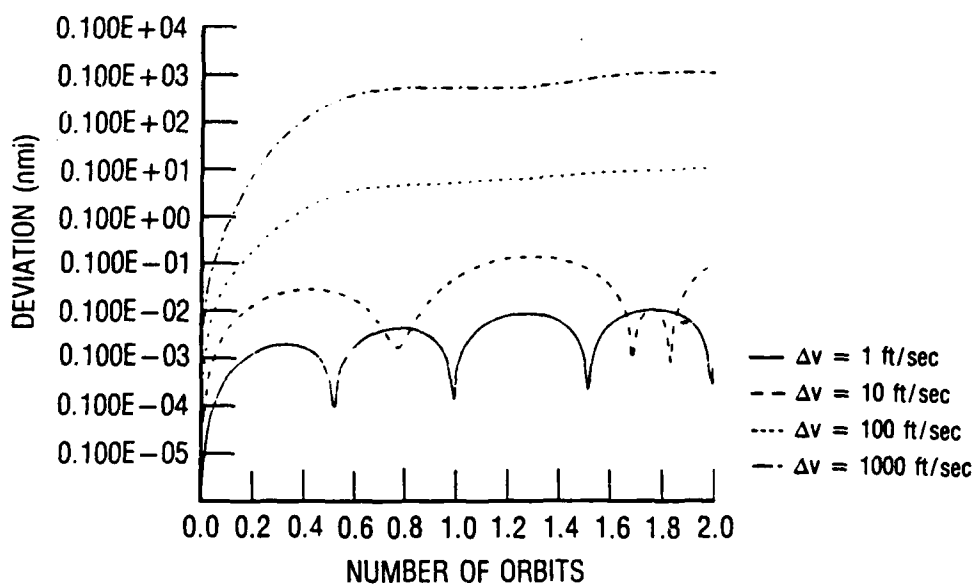
Figure 15.  Deviation Between Exact and Linear Solution:
x versus Time; Radial Ejection
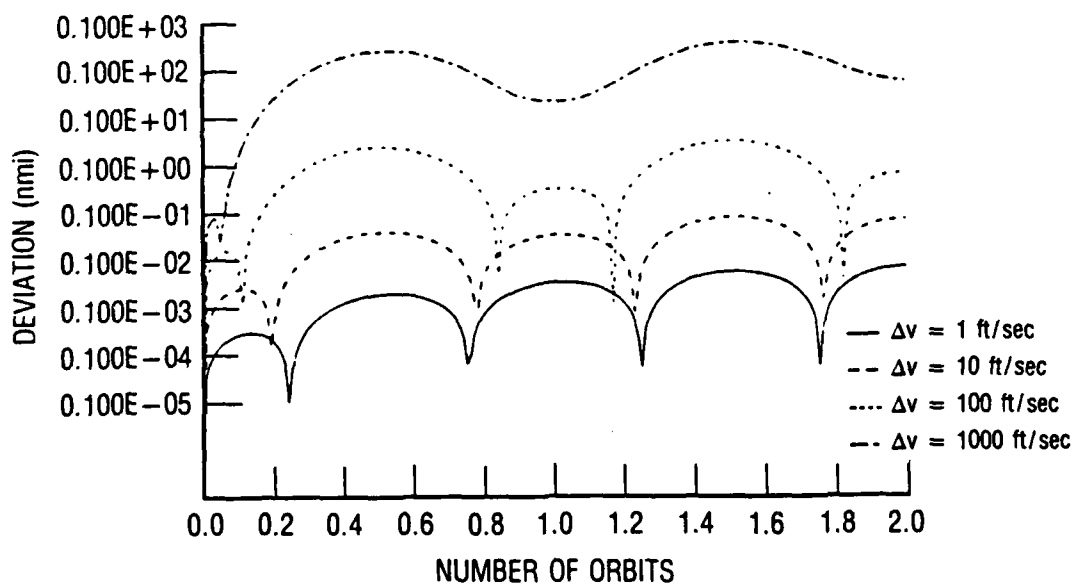


Figure 16.  Deviation Between Exact and Linear Solution:
y versus Time; Radial Ejection
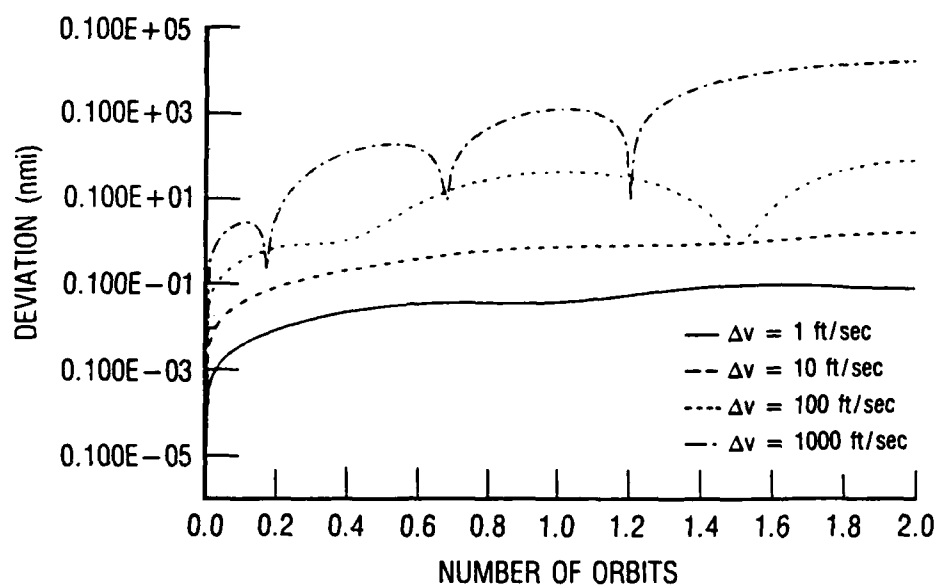
Figure 17.  Deviation Between Exact and Linear Solution: x versus Time; Tangential Ejection
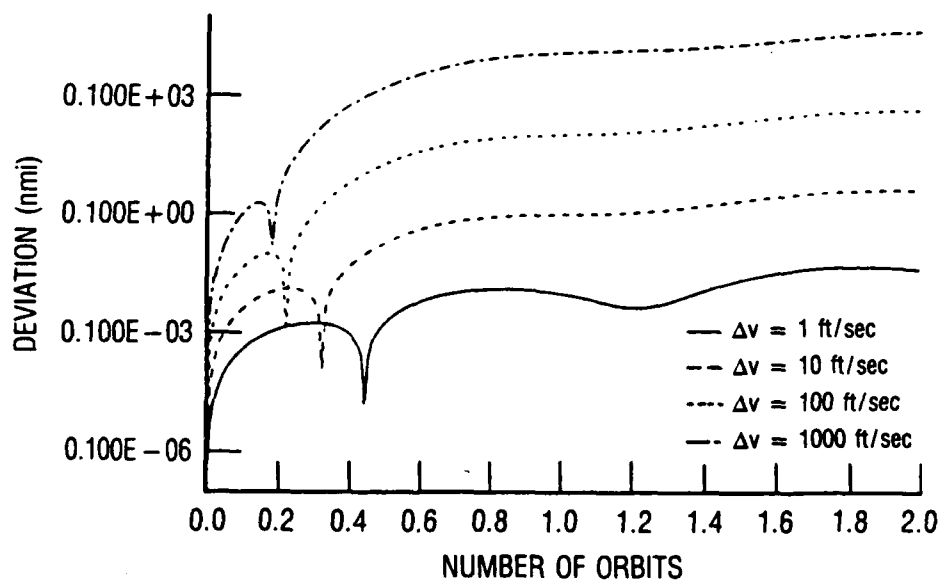


Figure 18.  Deviation Between Exact and Linear Solution: y versus Time; Tangential Ejection
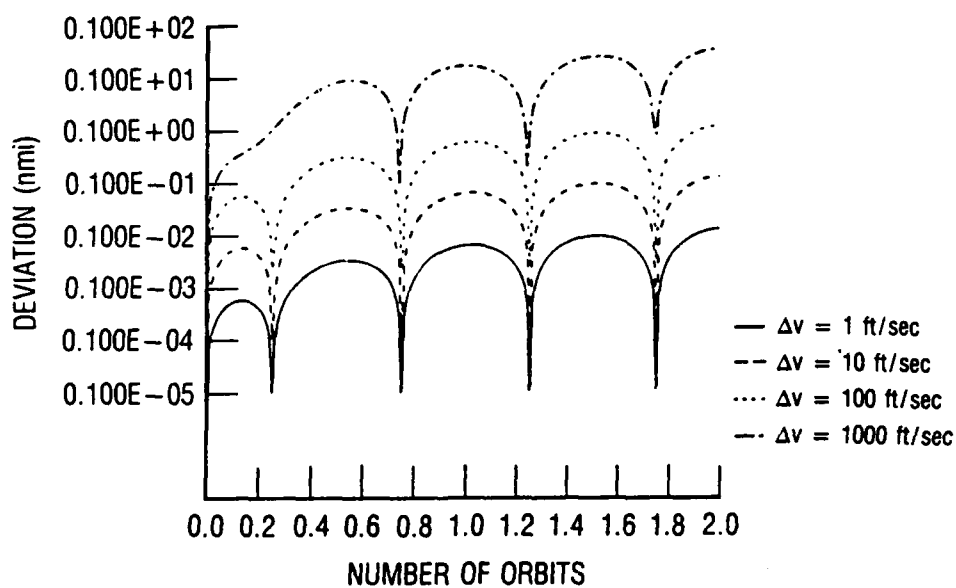
Figure 19. Deviation Between Exact and Linear Solution: z versus Time; Out-of-Plane Ejection
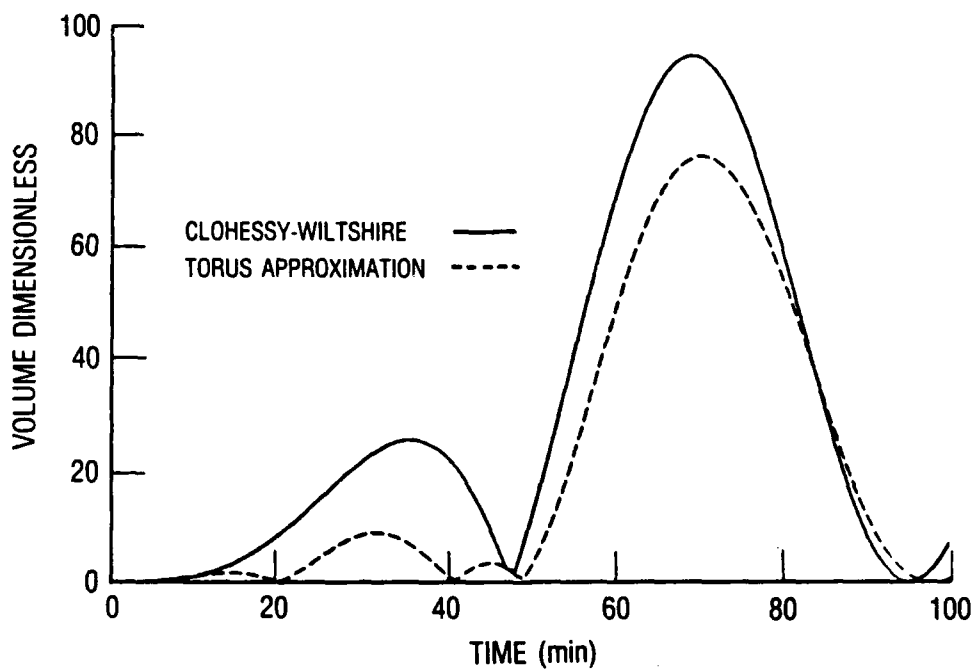


Figure 20. Volume versus Time, Clohessy-Wiltshire and Torus Approximation

44

## 4. THE EFFECTS OF PERTURBATIVE FORCES
## ON THE DEBRIS CLOUD EVOLUTION

### 4.1   INTRODUCTION

In previous sections, the volume of a debris cloud following an on-orbit breakup of a spacecraft assumed an inverse-square gravitational field and failed to include any additional external forces acting upon the individual debris particles.  In actuality, there are always external forces acting in addition to higher order harmonic terms in the gravity field.  This section reexamines the effects of one such harmonic term, $J_2$ (earth oblateness term), and a potentially important external force, atmospheric drag, on the shape and size of a debris cloud.  The approach used is based upon a simplified, first-order formulation which provides a cursory but timely estimate of the propagation time for the cloud to cover the entire globe as well as an early estimate of volume effects used for density calculations.

### 4.2   BACKGROUND

As shown in Sections 2 and 3, the linearized Clohessy-Wiltshire equations provide an adequate solution for the relative motion between two objects in space with low initial relative velocities.  However, there exist solutions to the linearized volume equations that produce a "pinch point" or a point of zero volume.  This point occurs at integer number of revolutions after the orbital breakup begins.  Because of this pinch point, the density of debris becomes infinite (number of particles divided by the volume) and thus produces an unacceptable collision hazard.  However, since this volume is initially infinitesimal, there is very little chance of a collision with another spacecraft.

In the true situation, there will not be an exact regrouping of the debris.  External forces plus variations in the earth's gravity field will cause the volume to be perturbed, thus relieving the singularity in density at integer number of revolutions.  Therefore, accounting for some of these perturbations will provide a better understanding of what actually happens to this debris cloud.

45

## 4.3 ANALYSIS

As shown in Section 2, the dimensionless volume of a debris cloud is

$$V = \frac{4\pi}{3} \left| \text{determinant } [M] \right| \tag{46}$$

where

$$M = \begin{bmatrix} a_{11} & a_{12} & 0 \\ -a_{21} & a_{22} & 0 \\ 0 & 0 & a_{33} \end{bmatrix} \tag{47}$$

$$a_{11} = -3\theta + 4 \sin \theta$$

$$a_{12} = -a_{21} = 2(1 - \cos \theta)$$

$$a_{22} = \sin \theta$$

$$a_{33} = \sin \theta \tag{48}$$

where $\theta$ is the angle swept out by the rotating reference frame with respect to the inertial frame. The matrix [M] is the state transition matrix relating relative position to initial velocity.

In this section, the elements of [M] are slightly perturbed by $J_2$ and atmospheric drag, and the results are compared to those obtained in the linearized solution.

The first step is to perturb the functions $a_{ij}$. One possible formulation is

$$a_{11} = -3\theta + 4 \sin \theta$$

$$a_{12} = -a_{21} = 2[1 + f_1(t)] - 2 \cos \theta[1 - f_1(t)]$$

$$a_{22} = \sin \theta[1 - f_2(t) + f_2(t)/|\sin \theta|]$$

$$a_{33} = g(t) + |\sin \theta| \tag{49}$$

These functions have initial values of zero and steady-state values of

$$f_1(t_f) = 1$$

$$f_2(t_f) = 1$$

$$g(t_f) = \frac{a \sin i}{\frac{\Delta v}{\omega}}$$

where i is the inclination of the target spacecraft, $\omega$ is the rate of increase of $\theta$, and $t_f$ is the ending time of the approximation.

Assume a nearly linear relationship for the functions $f_1(t)$, $f_2(t)$, and $g(t)$, such that

$$f_1(t) = C_1 t + C_4(\theta - \sin \theta)$$

$$f_2(t) = C_2 t + C_5(\theta - \sin \theta)$$

$$g(t) = C_3 t \qquad (50)$$

where the constants $C_i$, i=1,2,...,5 are to be determined, and depend upon the orbital elements (altitudes at apogee and perigee, and inclination) of the debris source.

The functions $f_1(t)$ and $f_2(t)$ spread the debris out in the radial direction; they come directly from the spreading due to atmospheric drag and the rotation of the line of apsides of the individual particle orbits. The function $g(t)$ is an out-of-orbit plane change, this time due to a shifting in the right ascension of ascending nodes of the debris particle orbits. However, the right ascension of ascending nodes rotates about the polar axis of the earth, and not the normal axis to the orbit.

## 4.4 $J_2$ EFFECTS

The constants $C_1$, $C_2$, and $C_3$ are due to the imperfections in the earth's gravitational field; i.e., the zonal harmonic term $J_2$. The $C_1$ and $C_2$ terms relate the shifting in the line of apsides, while the $C_3$ term relates the shift in the line of nodes of the orbit.

First, take the equation for the shifting of the line of apsides at an altitude h as

$$\dot{\omega} = \frac{9.96399}{(1 - e^2)^2} \left[ \frac{R}{(R + h)} \right]^{3.5} [2 - \frac{5}{2} \sin^2(i)] \frac{deg}{mean\ solar\ day} \tag{51}$$

This is with respect to an earth-centered, inertial reference frame. Assume as a center of a rotating reference frame (with respect to the inertial frame) the position of an object before it breaks up in orbit. After the breakup occurs, groups of particles will be traveling with a greater $\dot{\omega}$ than the satellite, had the breakup not occurred. Likewise, there are groups of particles with smaller $\dot{\omega}$ values. Statistically, by finding the average greater $\dot{\omega}$ and the average lesser $\dot{\omega}$, one can find a relative shifting in the line of apsides. For a greater $\dot{\omega}$, the semi-major axis decreases. This probabilistic change ($\Delta a$) in the semi-major axis, a, is a function of the change in velocity as per Eq. (28)

$$<\Delta a> = a\ (\Delta v/v) \tag{52}$$

where v is the orbital velocity at breakup with respect to an earth-centered inertial reference frame. The relative shift in the line of apsides for a circular orbit is

$$<\dot{\Delta\omega}> = \Delta K\ [2 - \frac{5}{2} \sin^2(i)] \tag{53}$$

where

$$\Delta K = K_+ - K_-$$

48

and, converting to appropriate units

$$K_+ = 2.01 \times 10^{-6} \left(\frac{R}{a - \langle \Delta a \rangle}\right)^{3.5} \frac{rad}{sec} \tag{54}$$

and

$$K_- = 2.01 \times 10^{-6} \left(\frac{R}{a + \langle \Delta a \rangle}\right)^{3.5} \frac{rad}{sec} \tag{55}$$

Similarly, for the rotation of the line of nodes, the equation

$$\dot{\Omega} = \frac{-9.9639}{(1 - e^2)^2} \left(\frac{R}{a}\right)^{3.5} \cos(i) \frac{deg}{mean\ solar\ day} \tag{56}$$

relates the change in nodes as a function of orbital elements.

Again, we are interested in a relative rotation in the line of nodes, so

$$\langle \Delta \dot{\Omega} \rangle = |\Delta K \cos(i)| \tag{57}$$

The time that it takes the line of nodes to shift 180° is

$$T_\Omega = \frac{\pi}{\langle \Delta \dot{\Omega} \rangle} \tag{58}$$

and the time it takes the line of apsides to shift 180° is

$$T_\omega = \frac{\pi}{\langle \Delta \dot{\omega} \rangle} \tag{59}$$

49

The constants $C_1$, $C_2$, and $C_3$ are therefore

$$C_1 = \frac{2}{T_\omega}$$

$$C_2 = \frac{1}{T_\omega}$$

$$C_3 = \frac{a}{T_\Omega \left(\frac{\Delta v}{\omega}\right)} \sin(i) \qquad (60)$$

where $\sin(i)$ is called a volume limit factor with limits on the functions as

$$f_1(t) = C_1 t \leq 1$$

$$f_2(t) = C_2 t \leq 1$$

$$g(t) = C_3 t \leq \frac{a \sin i}{\left(\frac{\Delta v}{\omega}\right)} \qquad (61)$$

## 4.5   ATMOSPHERIC DRAG

The effects of atmospheric drag affect only the radial and tangential components of the position.  This is an additive effect and is unrelated to $J_2$.  We can now assume a new expression for the perturbation functions $f_1(t)$ and $f_2(t)$.  The function $g(t)$ remains unchanged, since this is the out-of-plane function.  As in Eq. (50), assume

$$f_1(t) = C_1 t + C_4 (\theta - \sin \theta)$$

$$f_2(t) = \frac{f_1(t)}{2} \qquad (62)$$

The constant $C_4$ is now to be determined.

From Reference 7, the drop in altitude due to atmospheric drag is

$$\Delta h = \frac{\mu \rho g}{W/C_D A} \ (\theta - \sin \theta) \tag{63}$$

where

$\mu$ = gravitational constant

$\rho$ = atmospheric density

$g$ = acceleration due to gravity at sea level

$W$ = weight of debris particle

$C_D$ = drag coefficient

$A$ = cross-sectional area of debris particle

For a group of particles with a certain $\Delta v$, assuming an isotropic expansion, half of the particles would move into a higher energy orbit, and half would move into a lower energy orbit. Therefore, the immediate consequence is that the particles with a lower energy orbit will be affected more by the atmosphere than those at a higher energy level. Multiplying by a statistical factor of 0.5 and nondimensionalizing. Eq. (63) becomes

$$\Delta h' = \frac{0.5 \mu \rho g}{\left(\frac{\Delta v}{\omega}\right) W/C_D A} \ (\theta - \sin \theta) \tag{64}$$

where $\Delta h'$ is a nondimensional drop in altitude. The factor $C_4$ is the average over one revolution

$$C_4 = \frac{1}{2\pi} \int_o^{2\pi} \frac{0.5 \mu \rho g}{\left(\frac{\Delta v}{\omega}\right) B_C} \ d\theta \tag{65}$$

where $B_C = W/C_D A$ (ballistic coefficient).

A useful expression for the atmospheric density is (Ref. 8)

$$\rho = K e^{-h/c} \tag{66}$$

51

where

$K$ = reference density = $4.80711 \times 10^{-8}$ lb/ft$^3$

$h$ = altitude

$c$ = reference altitude = 12.58 nmi

The altitude function $h$ is dependent upon $\theta$, while everything else is approximately independent of $\theta$. By definition

$$h = r - R = a_N(1 - e_N \cos \theta) - R \tag{67}$$

The values $a_N$ and $e_N$ are semi-major axis and eccentricity of the new lower energy orbit, respectively, with

$$a_N = a \left[ 1 - (\Delta v / v) \right] \tag{68}$$

and

$$e_N = \frac{(\Delta v / v)}{1 - (\Delta v / v)} \tag{69}$$

where $a$ is the circular radius of the object orbit that is breaking up. Assembling the various expressions, Eq. (65) becomes

$$C_4 = \frac{1}{2\pi} \frac{0.5 \mu g}{\left( \frac{\Delta v}{\omega} \right) B_c} K \int_0^{2\pi} \exp\{-[a_N(1 - e_N \cos \theta) - R]/c\} d\theta \tag{70}$$

Integrating Eq. (70)

$$C_4 = \left( \frac{1}{2\pi} \right)^{3/2} \frac{0.5 \mu K g}{\left( \frac{\Delta v}{\omega} \right) B_c} \left[ \frac{c}{a(\Delta v / v)} \right]^{1/2} \exp\{[R - a_N(1 - e_N)]/c\} \tag{71}$$

and, as before,

$$C_5 = \frac{C_4}{2}$$

52

## 4.6    RESULTS

Take, for example, the following two cases.

Case 1:  Assume that the object breaking up is at an altitude of
200 nmi, inclined at 45° with respect to the equator.  Figures 21 and 22 show
the constants $C_i$, i = 1,2...5, for an applied $\Delta v$.  Assuming a $\Delta v$ of 100 m/s,
we note that Figure 23 shows the volume versus time profile with $J_2$ only, drag
only, no perturbations, and drag and $J_2$.  At $\theta = 2\pi$, the volume (in non-
dimensional form) is 4.7 x $10^{-3}$ (dimensionalizing, V = 3200 $km^3$).  In this case,
it will take 322 days for the line of apsides to shift 180°, and 5.7 years for
the cloud to envelop the earth.

Case 2:  Again, we have a circular orbit with an altitude of 500 nmi,
with an inclination of 45°.  Figures 24 and 25 show the constants $C_i$, i = 1,
2...5 for breakup.  Figures 26 show the volume versus time profile with $J_2$
only, drag only, no perturbations, and $J_2$ drag.  At $\theta = 2\pi$, the nondimensional
volume is 6.5 x $10^{-5}$ (dimensionally, V = 63 $km^3$) which produces a finite density
at $\theta = 2\pi$.  For this example, it will take 410 days for the line of apsides to
rotate 180°, and 7.2 years for the cloud to envelop the earth.

## 4.7    SUMMARY

The addition of atmospheric drag into the volumetric equations spreads
the cloud's shape into a plane at the integer orbit pinch points.  Only with
the addition of $J_2$ do we have a spreading out in the out-of-orbit direction,
thus creating a volume at the pinch points.  Although the volumes at the pinch
points in the first few revolutions are small, they are not zero and thus yield
a more accurate assessment of the potential collision hazard.  Also, as
expected, for a higher altitude orbital breakup, the atmospheric drag has less
of an effect than for a lower orbit breakup.
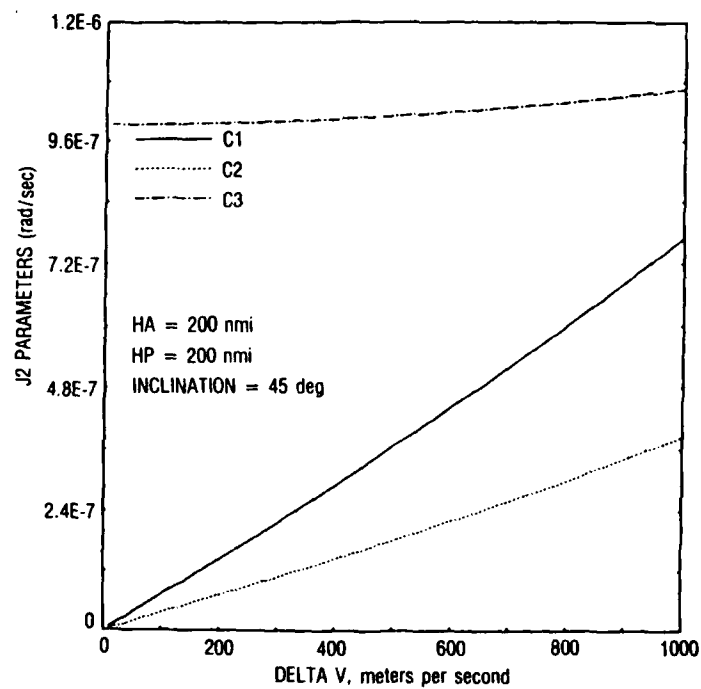
Figure 21.  $J_2$ Parameters, $C_1$, $C_2$, $C_3$, versus $\Delta v$;
200-nmi Circular Orbit
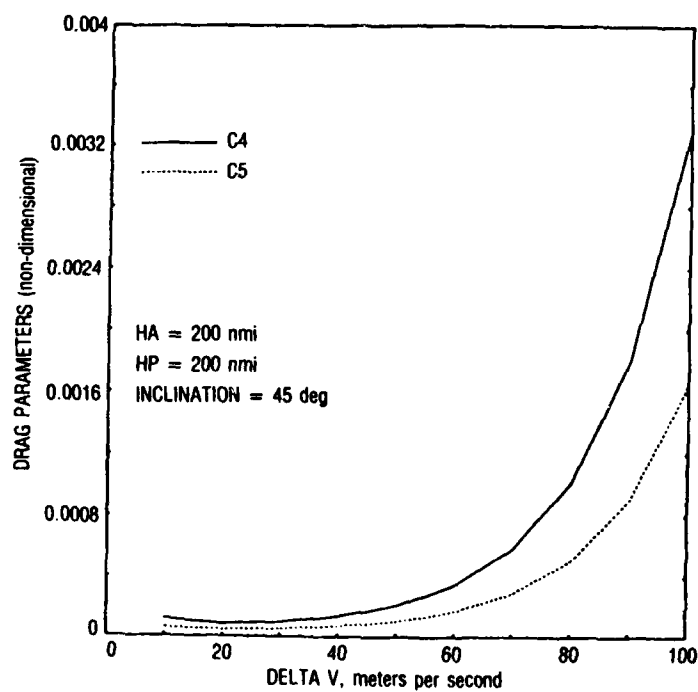


Figure 22.  Drag Parameters, $C_4$, $C_5$, versus $\Delta v$;
200-nmi Circular Orbit
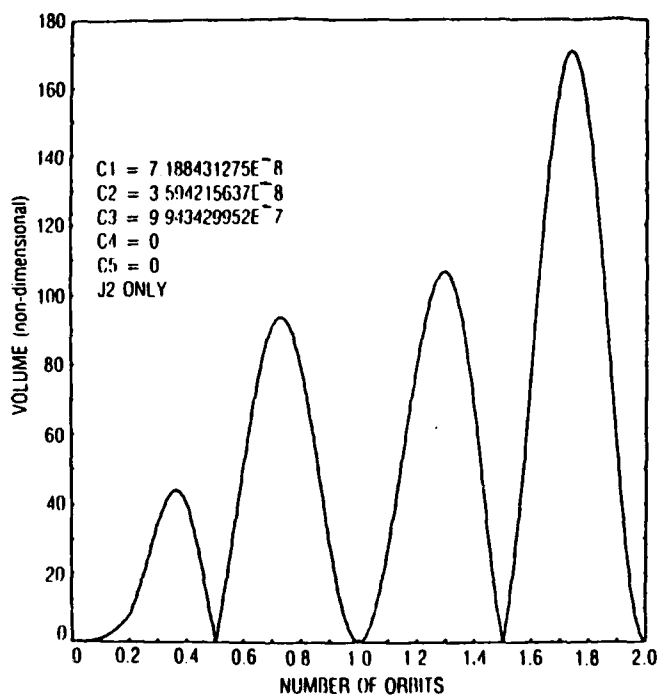
Figure 23a.   Volume versus Time for Breakup at 200-nmi Altitude, $J_2$ Only
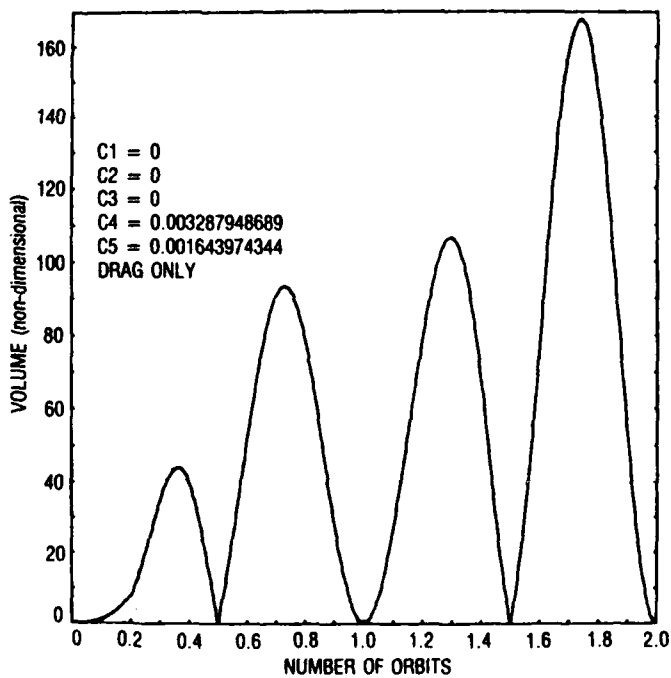


Figure 23b.   Volume versus Time for Breakup at 200-nmi Altitude, Drag Only
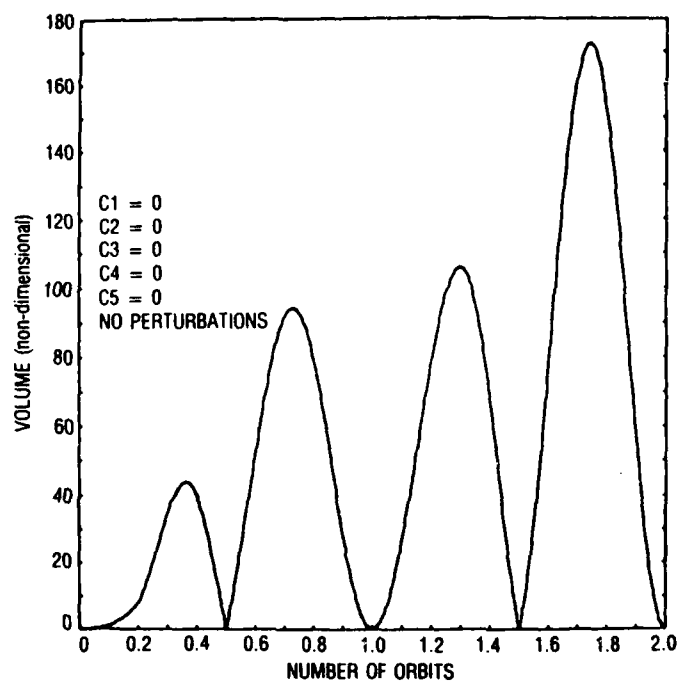
Figure 23c.  Volume versus Time for Breakup at 200-nmi Altitude,
No Perturbations
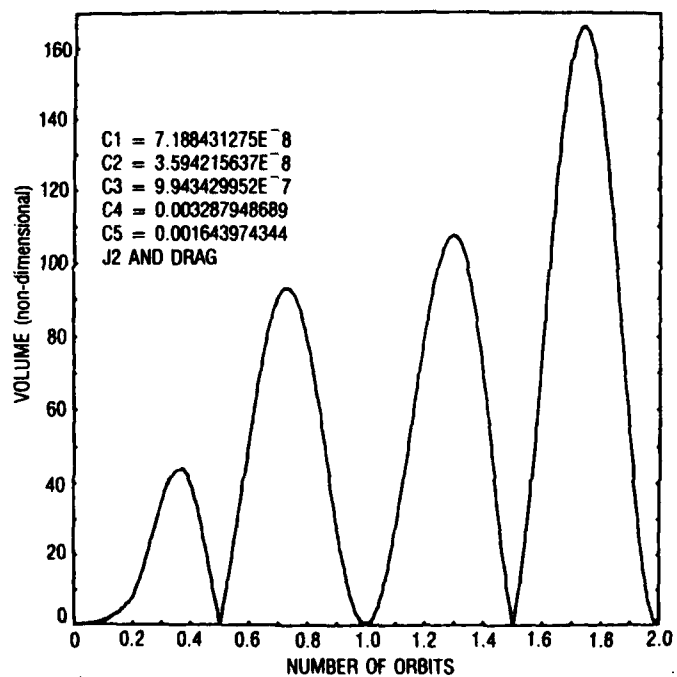


Figure 23d.  Volume versus Time for Breakup at 200-nmi Altitude,
$J_2$ and Drag
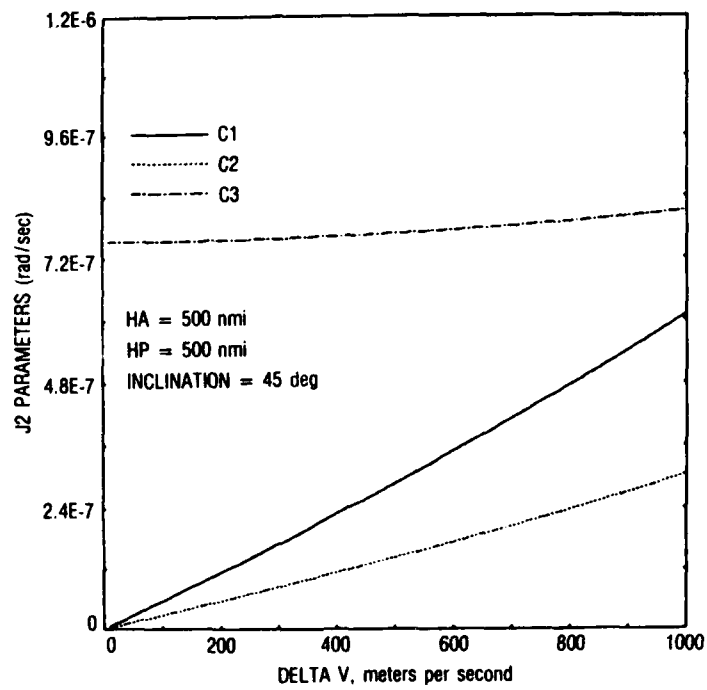
Figure 24. $J_2$ Parameters, $C_1$, $C_2$, $C_3$, versus $\Delta v$;
500-nmi Circular Orbit
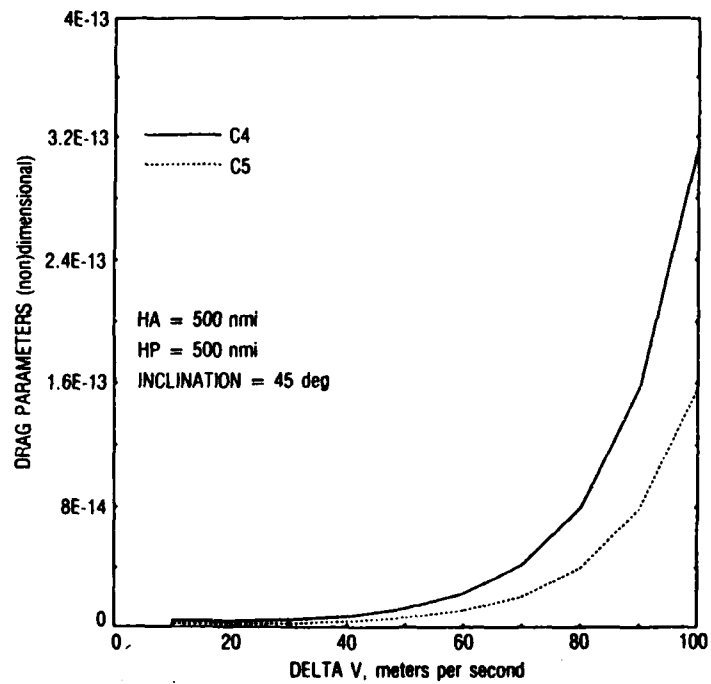


Figure 25. Drag Parameters, $C_4$, $C_5$, versus $\Delta v$;
500-nmi Circular Orbit

57
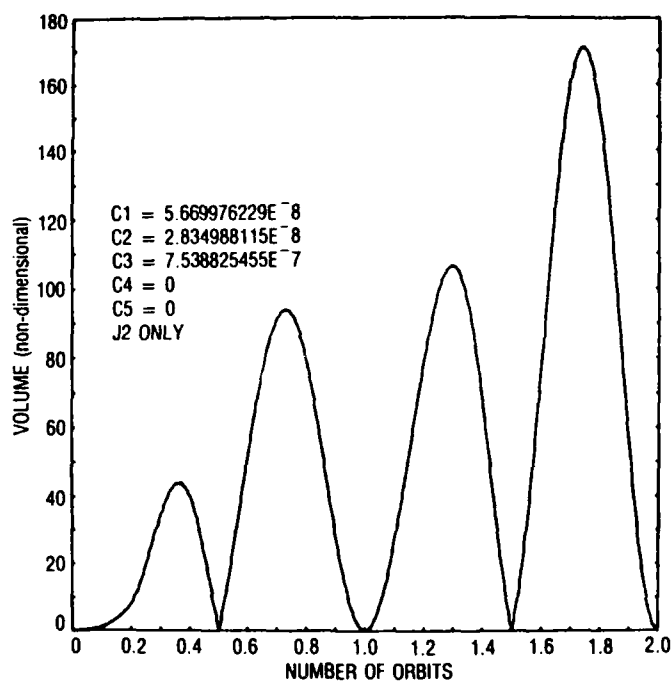
Figure 26a.   Volume versus Time for Breakup at 500-nmi Altitude, $J_2$ Only
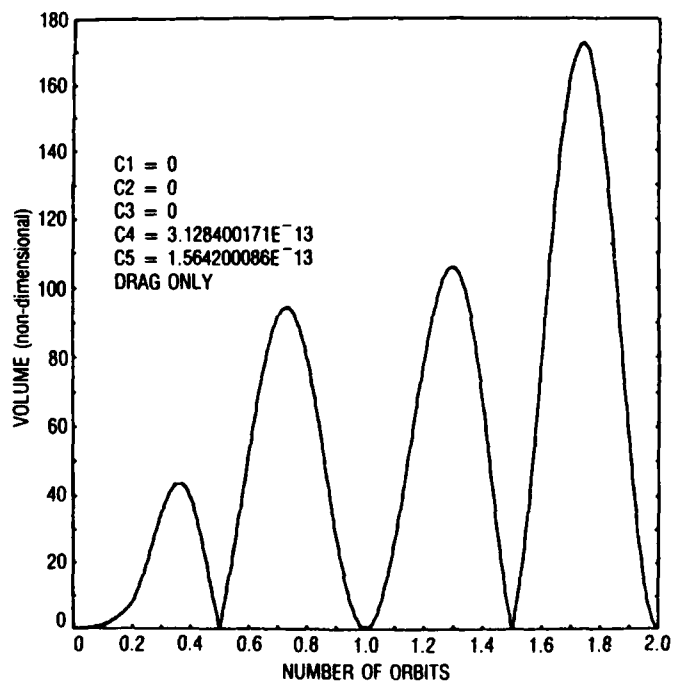


Figure 26b.   Volume versus Time for Breakup at 500-nmi Altitude, Drag Only
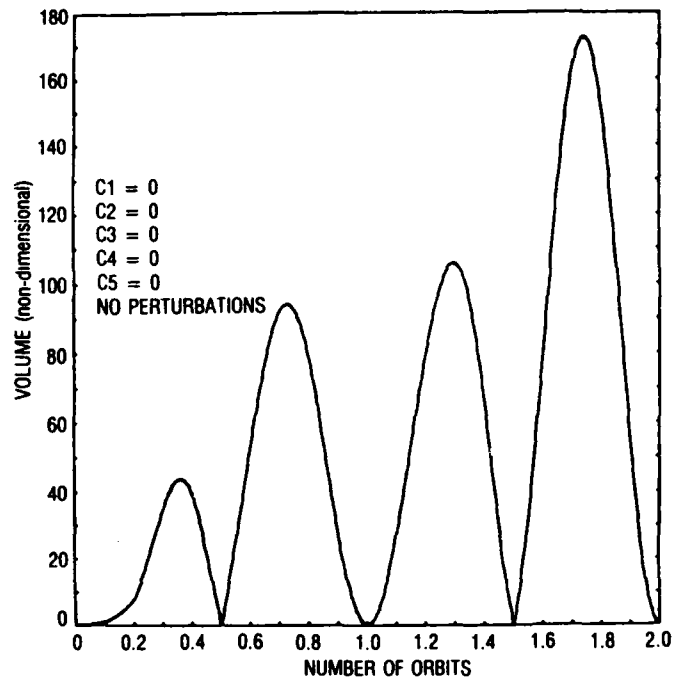
Figure 26c. Volume versus Time for Breakup at 500-nmi Altitude, No Perturbations
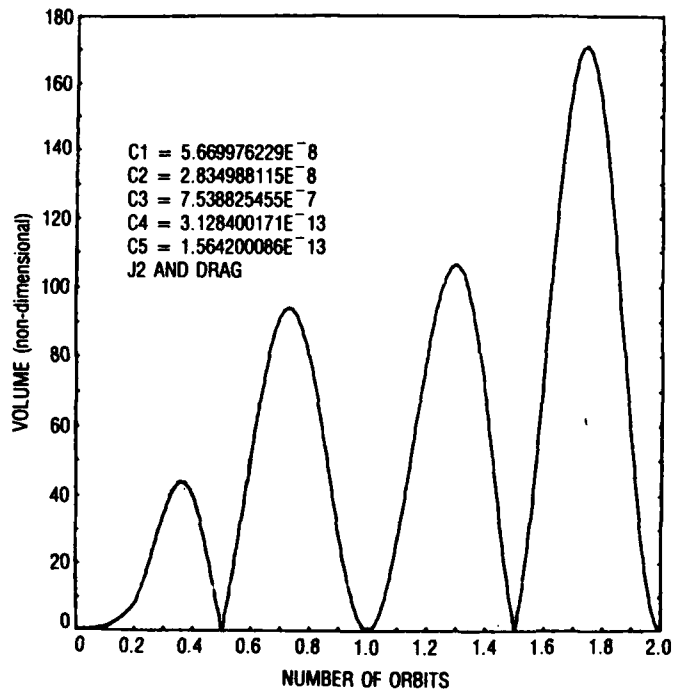


Figure 26d. Volume versus Time for Breakup at 500-nmi Altitude, $J_2$ and Drag

## 5. COMPUTING FRAGMENT DIRECTIONS AND ORBITS AFTER COLLISION

### 5.1 INTRODUCTION

Section 6 describes a method for determining the masses and velocities of fragments that result from a hypervelocity collision. The velocities derived are relative to the center of mass (CM). This section calculates the center of mass velocity vector and determines the fragments' directions relative to the center of mass. Both sets of results are then used to determine the fragments' orbits. An example is used to illustrate the method. The results are tabularized and graphed.

### 5.2 METHOD OF ANALYSIS AND EQUATIONS

There are three steps in the methods of analysis to determine the fragment orbits: (a) to determine the orbit of the center of mass of the two objects colliding; (b) to calculate the masses, velocities (Section 6), and directions of the fragments relative to the center of mass; and (c) to input the above results into an orbit element conversion program to compute orbital properties of the fragments. Figure 27 summarizes these three points and illustrates the center of mass orbit of two intersecting orbits.

### 5.2.1 Coordinates of Center of Mass

To find the coordinates for the center of mass of the two objects, let $\vec{r}$ be the position vector of the two objects at intersection, and let $\vec{v}_1$ and $\vec{v}_2$ be their respective velocity vectors (as shown in Fig. 27) such that

$$\vec{r} = r_x \hat{i} + r_y \hat{j} + r_z \hat{k} \tag{72}$$

$$\vec{v}_1 = v_{1x} \hat{i} + v_{1y} \hat{j} + v_{1z} \hat{k} \tag{73}$$

$$\vec{v}_2 = v_{2x} \hat{i} + v_{2y} \hat{j} + v_{2z} \hat{k} \tag{74}$$

The conservation of angular momentum is then applied in which the total angular momentum of the system at the intersection point, $\vec{P}$, is equal to the

# METHOD OF ANALYSIS

- DETERMINE CENTER OF MASS ORBIT OF TWO VEHICLES

- CALCULATE VELOCITIES AND DIRECTIONS OF FRAGMENTS
  RELATIVE TO CENTER OF MASS

- DETERMINE ORBITAL ELEMENTS OF DEBRIS



$\vec{r}$ = radius vector of encounter point   $\vec{V}_2$ = velocity vector of Object 2

CM = center of mass of Objects 1 and 2   $\vec{V}_{CM}$ = velocity vector of center of mass

$\vec{V}_1$ = velocity vector of Object 1
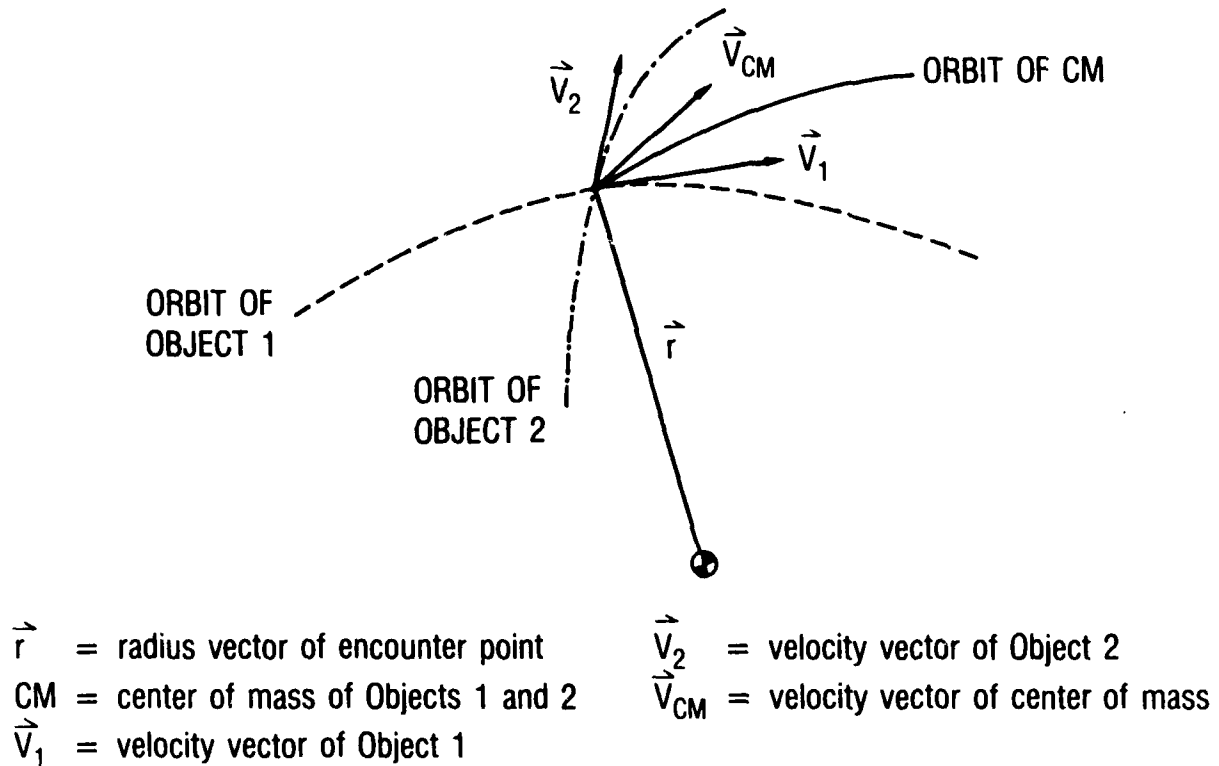
Figure 27.  Center of Mass Vector from Two Intersecting Objects

62

sum of the angular momenta of the two objects, $\vec{P}_1 + \vec{P}_2$. The quantity, $\vec{P}$, refers to the total angular momentum as if it were concentrated at the center of mass. This is precisely what we want, since we are trying to find the velocity of the center of mass. Using the conservation principle, we get

$$\vec{P} = \vec{P}_1 + \vec{P}_2 \tag{75}$$

where

$$\vec{P}_1 = \vec{r} \times m_1 \vec{v}_1 \tag{76}$$

$$\vec{P}_2 = \vec{r} \times m_2 \vec{v}_2 \tag{77}$$

$$\vec{P} = \vec{r} \times M \vec{v}_{CM} \tag{78}$$

$$M = m_1 + m_2 \tag{79}$$

$$\vec{v}_{CM} = v_x \hat{i} + v_y \hat{j} + v_z \hat{k} \qquad \text{(center of mass velocity)} \tag{80}$$

Solving Eq. (75), using the rest of the relations, yields the components of the center of mass velocity vector

$$v_x = (m_1 v_{1x} + m_2 v_{2x})/M \tag{81}$$

$$v_y = (m_1 v_{1y} + m_2 v_{2y})/M \tag{82}$$

$$v_z = (m_1 v_{1z} + m_2 v_{2z})/M \tag{83}$$

Thus, the center of mass velocity is expressed in terms of mass of the two objects and their velocities.

### 5.2.2  Fragment Velocity Relative to the Center of Mass

The kinetic energy of the colliding objects and the center of mass are used to compute the fragment velocities.

The total kinetic energy of the two objects before collision is given by

$$KE \text{ (before collision)} = (m_1 v_1^2 + m_2 v_2^2)/2 \qquad (84)$$

After the collision, the total kinetic energy of the system can be expressed by the sum of the kinetic energy of the total mass moving with the velocity of the center of mass and that due to the motions of the individual particles relative to the center of mass (Ref. 9). The following equation expresses this as

$$KE \text{ (after collision)} = \left[ (m_1 + m_2) v_{CM}^2 + \sum_{i=1}^{n} m_i \dot{p}_i^2 \right] \Big/ 2 \qquad (85)$$

where

$m_i$ = mass of i-th fragment

$\dot{p}$ = velocity magnitude of i-th fragment
    relative to the center of mass

$n$ = number of fragments

If the collision is assumed to not conserve kinetic energy, then Eqs. (84) and (85) can be related in Eq. (86) (canceling the 1/2's)

$$m_1 v_1^2 + m_2 v_2^2 = (m_1 + m_2) v_{CM}^2 + \sum_{i=1}^{n} m_i \dot{p}_i^2 + KE_{LOST} \qquad (86)$$

where $KE_{LOST}$ = twice the amount of kinetic energy lost in the collision.

The unknowns in Eq. (86) are $m_i$, $\dot{p}_i$, and n. Thus, rearranging Eq. (86) yields

$$\sum_{i=1}^{n} m_i \dot{p}_i^2 = m_1 v_1^2 + m_2 v_2^2 - (m_1 + m_2) v_{CM}^2 - KE_{LOST} \qquad (87)$$

As mentioned earlier, Section 6 describes a method for determining the number of fragments, n, the fragment masses, $m_i$, and velocities, $\dot{p}_i$, that solve Eq. (87).

### 5.2.3 Determining Fragment Directions

Conservation of momentum is used to determine fragment direction. A random direction relative to the center of mass was given to the first fragment. The second fragment was given a direction (relative to the center of mass) opposite the first. In this way, the momentums imparted to the first two fragments relative to the center of mass cancel. This assumes that these fragments have the same mass and velocity. The process is repeated until all fragments have been assigned directions. The directions are chosen randomly from the uniform directions derived in Appendix B.

### 5.2.4 Determining Fragment Orbits

After completion of the previous analysis in Sections 5.2 and 6, the center of mass position and velocity should be known and the fragments should all have assigned velocities and directions relative to the center of mass. The velocity of the center of mass and the fragment velocities relative to it can be vectorially added to obtain the inertial velocity of each of the fragments. At this point, orbit element conversions are used to convert the elements from earth centered inertia (ECI) to other coordinate systems in order to determine the orbital properties of the fragments. In this analysis, the On-Line Orbital Mechanics (OLOM) program (Ref. 10) was used to perform the conversions.

### 5.3 DATA GENERATION

Once the orbit elements of the fragments have been determined, the data can be presented in various ways. In our analysis we presented data, typically, in three formats. The first is a table showing the percentage of fragment perigees above 100 nmi, the percentage between 0 and 100 nmi, and the percentage below the earth's surface. Thus, the table shows how many fragments will remain in orbit and reenter sometime later, and those that will reenter

immediately. An example is shown in Table 3. In this example, the colliding bodies have a mass ratio of 15. The heavier object is in low earth orbit, and the relative velocity at collision is 23,183 ft/sec. The first three columns are the result of the analysis in Section 6.

The second way to present data is to plot the fragment apogee and perigee altitudes versus the fragment periods. An example of this plot is shown in Figure 28. The 0 nmi altitude represents the earth's surface. The figure resembles two wings that meet at a point. The upper wing shows the apogee altitudes, and the lower wing shows the perigee altitudes versus the periods. Thus, two points are plotted for each fragment. Note the correspondence between the perigees plotted in Figure 28 and the percentages listed in Table 3. The APL graphics package, EZPLOT (Ref. 11), was used in conjunction with OLOM to generate Figure 28. It would be possible also to plot any of the fragment orbital elements.

Notice in Figure 28 that the right side of the upper wing and the left side of the lower wing are not straight. They have a slight bow in them. This bow is only noticeable with the high spread velocities. This example used spread velocities of over 5000 ft/sec. In Figure B-4 of Appendix B, these parts of the wings appear straight; the spread velocity used for Appendix B's example is 1000 ft/sec. If the spread velocity is large enough, the bow appears regardless of whether the fragment spread is from a circular or an eccentric orbit and regardless of the position within the eccentric orbit.

The third method of presenting data is to plot footprints that show the region on the earth over which reentering debris will fall. The ECI coordinates of the reentering fragments are input to the program PECOS (Parametric Examination of the Cost of Orbit Sustenance, Ref. 12) and propagated until a specified altitude is reached. PECOS will print out the latitude and longitude of the fragments at the specified altitude. Any program can be used that can accurately propagate the orbital elements under the influence of drag. The latitudes and longitudes are then plotted onto a map using EZPLOT.

Table 3. Fragment Distribution for Mass Ratio of 15

| Number of Fragments | Fragment Mass (lb) | Δv (ft/sec) | No. of Perigees Below 0 nmi | No. of Perigees Between 0 and 100 nmi | No. of Perigees Above 100 nmi |
|---|---|---|---|---|---|
| 4 | 20 | 697 | 4 | 0 | 0 |
| 8 | 10 | 876 | 8 | 0 | 0 |
| 20 | 5 | 1034 | 19 | 1 | 0 |
| 30 | 2 | 1305 | 28 | 0 | 2 |
| 40 | 1 | 3558 | 24 | 4 | 12 |
| 50 | 0.8 | 3916 | 32 | 4 | 14 |
| 60 | 0.6 | 4094 | 41 | 6 | 13 |
| 80 | 0.4 | 4273 | 53 | 1 | 26 |
| 100 | 0.2 | 5596 | 68 | 8 | 24 |
| 200 | 0.1 | 7241 | 129 | 11 | 60 |
| 400 | 0.05 | 11068 | 281 | 26 | 93 |
| 992 | | | 687 (69.3%) | 61 (6.1%) | 244 (24.6%) |

Mass ratio is of colliding bodies
Δv is relative to the center of mass
Spacecraft orbit: Low altitude circular
Relative velocity of collision: 23183 ft/sec

67
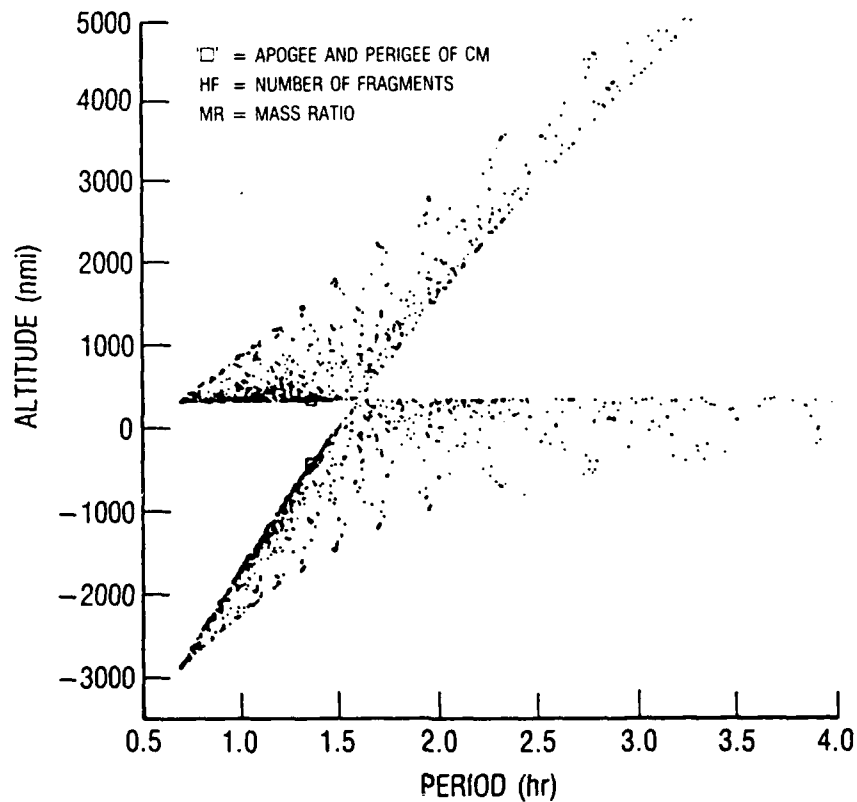
Figure 28.  Apogee and Perigee Altitudes of Each Fragment
versus Its Period; MR = 15; NF = 992

Since the concern of our analysis was the extent of the footprint and
not the distribution of fragments within it, it was not necessary to propagate
the elements of all the fragments.  In this analysis, only seven fragment
directions (per mass group) that would define the contour of the footprint
(for that particular group) are propagated.  All the directions used lie in
the plane defined by the velocity vector of the center of mass, $\vec{v}_{CM}$, and the
cross product of the position and velocity vectors, $\vec{r} \times \vec{v}_{CM}$ (Fig. 29).  More
specifically, the directions chosen were in the uprange half of the figure (180
to 360°--the shaded region).

Figure 30 shows a typical footprint that includes three contours. There is one contour for each mass group (0.1, 1, and 10 lb). Each contour was formed by connecting seven "x's." The seven x's are the latitude/longitude "impact" locations that result from the seven fragment directions propagated by PECOS. The three contours are centered over the groundtrack of the orbiting object. The 10-lb and heavier fragments would be contained within the smallest contour, 1.0-lb and heavier in the middle contour, and 0.1-lb and heavier in the largest contour.

Note that the figure does not show how many of the fragments will survive reentry (if any) and that the masses listed are the masses before reentry, not at impact. Thus, even though the curves show regions over which fragments of various "preentry" masses may impact, no fragments may actually reach the ground. Further analysis in this area is needed in order to assess the actual threat on the ground to impacting debris.

## 5.4    SUMMARY

This section explained the three steps used to determine the orbital elements of the fragments resulting from two colliding objects. First, calculate the center of mass velocity vector from equations presented. Then determine the fragment masses, velocities, and directions relative to the center of mass. Finally, use the results from the first two steps to determine the orbit properties of the fragments.

Three methods of presenting the data also were shown: (a) tabular data showing the percentages of fragments that reenter or stay in orbit, (b) graphs of the orbital elements that show the distribution, and (c) a footprint showing the regions on the earth in which fragments would be expected to impact (if they survive reentry).
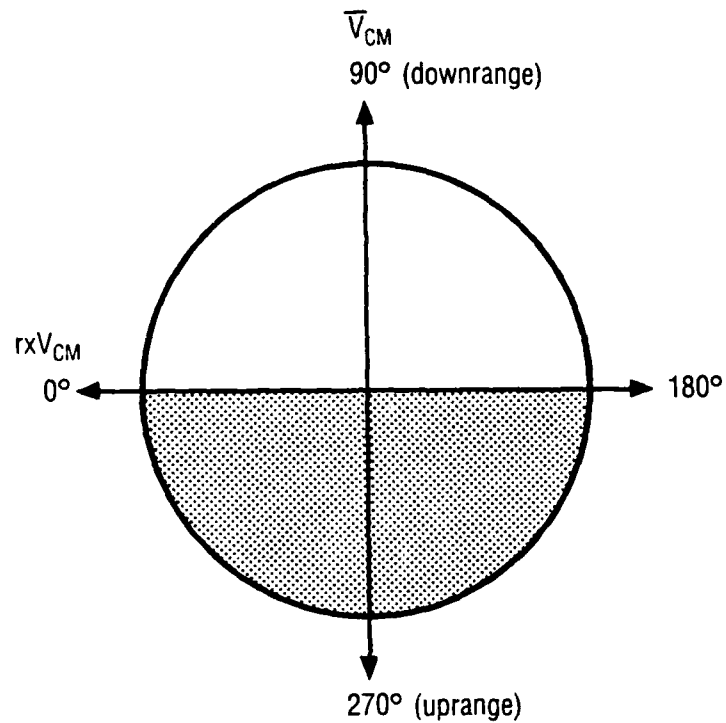
Figure 29.   Plane Defined by $\vec{v}_{CM}$ and $\vec{r} \times \vec{v}_{CM}$ Vectors (directions
typically used in PECOS propagation to generate
fragment footprint lie in shaded region)
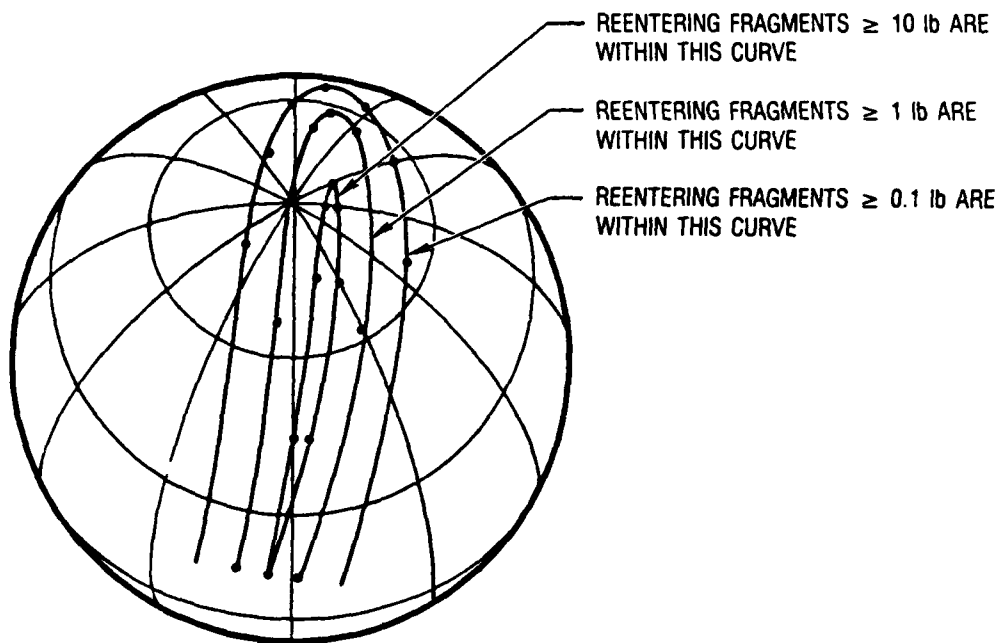


Figure 30.   Reentering Debris Footprint for Colliding
Objects with Mass Ratio of 15

# 6. DEBRIS GENERATION AT HYPERVELOCITY COLLISION IN SPACE

## 6.1    INTRODUCTION

Increase in debris as a result of collisions and explosions in space has been recorded.  Some of the collisions and explosions are involuntary and some are deliberate.  The debris can cause damage to other satellites in space.

The number and velocity of fragments generated by collision between two objects in space depends on the relative velocity of impact; the masses of colliding objects; and the material properties such as density, elastic limit, melting point, ultimate stress coefficient, and the impact scenario.  For example, in the case of hypervelocity, catastrophic impact, both objects will fragment.  In some other cases, there will be a crater formed in one object, whereby the ejected mass will fragment leaving the rest of the object intact. In the case of oblique impact, a part of the object will shear, leaving the remaining portion intact.  In this section, only the hypervelocity, catastrophic impact will be discussed.

This section presents a method for determining the number of fragments, their masses, and spread velocities created as a result of collision between two objects in space.

An analysis of debris generation at hypervelocity collision in space has been performed assuming conservation of momentum and energy.  A methodology has been developed to determine the mass of fragments and their spread velocities about the center of mass.  Size of a fragment with a given mass has been calculated assuming certain shape and density.

## 6.2    ANALYSIS

When two masses collide at near-hypervelocity or hypervelocity, internal pressurization develops which, in turn, generates internal shock waves. Nebolsine, et al. (Ref. 13) have studied the kinetic energy mechanism at Physical Sciences, Incorporated (PSI).  Figure 31 shows the shock wave

71

generation at impact. The expressions for pressure, velocity, and impulse of the shock wave are given below:

$$P_s = \rho v_p^2 \left(\frac{d}{R}\right)^3 \tag{88a}$$

$$v_s = v_p \left(\frac{d}{R}\right)^{3/2} \tag{88b}$$

$$I_s = \frac{\rho v_p R}{10} \left(\frac{d}{R}\right)^{3/2} \tag{88c}$$

where $P_s$ is pressure, $v_s$ is the velocity of shock wave, $I_s$ is impulse per unit area, $\rho$ is density of material, $v_p$ is relative velocity of impact, d is diameter of projectile, and R is radius of shock wave front which increases with time. Shock wave-related parameters are shown in Figure 31. For fragmentation, $I_s > \sigma_u t / a_t$ where $a_t$ is the speed of sound, t is the thickness of material, and $\sigma_u$ is the ultimate stress coefficient.
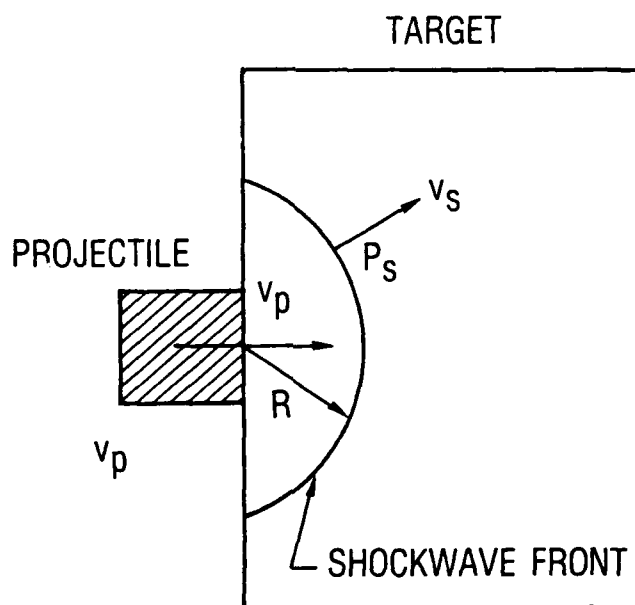


Figure 31. Shock Wave Propagation

72

Consider a case where two masses $m_1$ and $m_2$ moving at velocities $\vec{v}_1$ and $\vec{v}_2$ collide. From the conservation of momentum we get

$$m_1\vec{v}_1 + m_2\vec{v}_2 = (m_1 + m_2)\vec{v}_{cm} \tag{89}$$

where $\vec{v}_{cm}$ is the velocity of the center of mass.

Conservation of kinetic energy will yield the following equation:

$$\frac{1}{2} m_1 v_1^2 + \frac{1}{2} m_2 v_2^2 = \frac{1}{2}(m_1 + m_2)v_{cm}^2 + Q \tag{90}$$

where Q is the available energy for the spread of fragments created by impact. The term Q is related to fragment mass and spread velocity in the following manner:

$$Q = \frac{1}{2} \sum_i m_i v_i^2 + E' \tag{91}$$

where E' is the loss in energy due to heat and light generated at impact, $v_i$ is the spread velocity of i-th fragment with respect to the center of mass, and $m_i$ is the mass of that fragment. The center of mass is moving with velocity $v_{cm}$; at the same time, fragments are spreading with respect to the center of mass. For the case when E' = 0, Q (the energy available to spread the fragments about the center of mass) depends on the relative velocity of impact and the ratio between the two colliding masses and is given by

$$Q = F \cdot (KE)_{rel} \tag{92}$$

where $(KE)_{rel} = 1/2\, m_1 v_{rel}^2$, $v_{rel}$ = relative velocity at the time of collision. Fraction F is the ratio between Q and the relative kinetic energy, $(KE)_{rel}$, and is related to mass ratio $R(R = m_2/m_1)$ as shown in Figure 32 (Ref. 13). For a given mass ratio, one can obtain F and then use Eq. (92) to determine Q. Once the value of Q is determined, the problem is to determine fragment mass and assign the spread velocity to satisfy Eq. (91). This is discussed in the following sections.

73
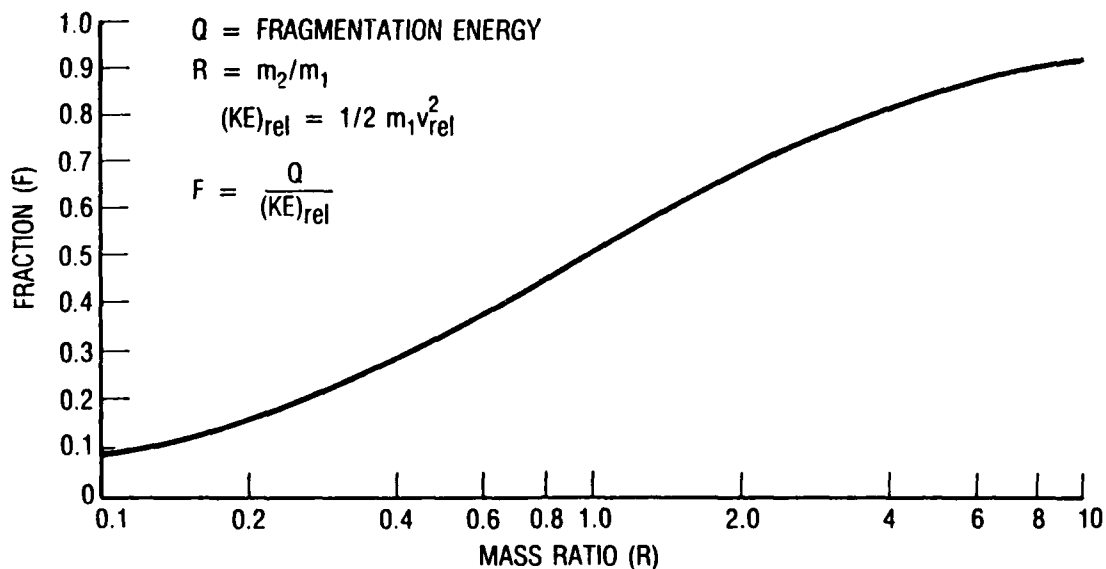
Figure 32.   Inelastic Collison Energy Fraction F
versus Mass Ratio R

## 6.2.1   Determination of Fragment Number

To determine the number of fragments of a given mass, the equation obtained by Kessler, et al. (Ref. 1) has been used.  This equation is empirical and was obtained on the basis of fragments generated in some test experiments.  This equation is given by

$$N = K\left(\frac{m}{M_e}\right)^n \tag{93}$$

where N is the number of fragments of mass m and greater; $M_e$ is the total mass fragmented after impact, $n = -0.75$; and K is a constant which depends on the rigidity of the material.  For a rigid material, $K = 0.4$; for a nonrigid material, $K = 0.8$.  A rigid material will fragment in pieces with a larger mass, and a nonrigid material will fragment in pieces with a smaller mass under the same impulse.  For collision between satellites, NASA has determined that $K \simeq 0.45$ is a good value to be used, because there is a fairly good agreement between predicted and observed results if this value of K is used.  Equation (93) can be used to obtain the number of fragments and their masses generated by hypervelocity impact and not by explosion.

74

Figure 33 has been taken from Reference 1 and is based on the result of a laboratory experiment. In this experiment, a 237-gm projectile was used to impact a target of 25 kg mass at a relative velocity of 3.3 km/sec. The cumulative number of fragments versus the diameter of the fragment is shown in this plot.

The fragments generated by explosion have a different distribution as a function of size than the fragments generated by collision. The following equations can be used to determine the number of fragments generated by explosion or breakup*:

$$N = 1.71 \times 10^{-4} \ M_e \exp(-0.02056 \ m^{1/2}) \text{ for } m > 1936 \text{ gm} \qquad (94a)$$

and

$$N = 8.69 \times 10^{-4} \ M_e \exp(-0.05756 \ m^{1/2}) \text{ for } m \leq 1936 \text{ gm} \qquad (94b)$$

where $M_T$ is the mass of target in grams, $M$ = the mass of fragment in grams, and N is the cumulative number of fragments with mass greater than M grams.
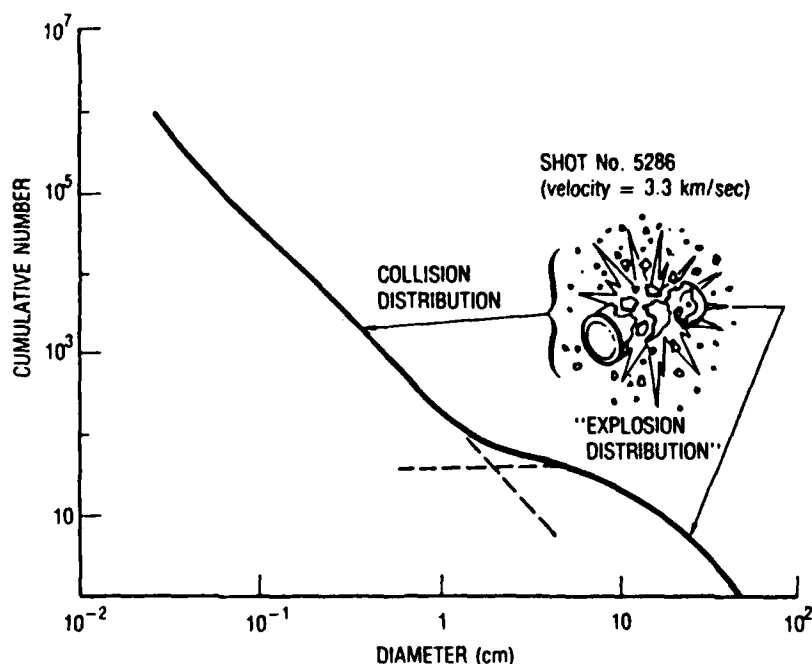


Figure 33.   Number of Fragments Produced from
            237-gm Projectile

---

*See Ref. 18.

Size of the fragment will depend on the mass density. For satellite structures, the density could vary between 0.1 to 5 gm/cm$^3$. It can be assumed that the small-sized fragments (0.1 cm diameter and smaller) will be spherical in shape; medium-sized fragments (between 0.1 and 20 cm diameter) will be cubical in shape; and large-sized fragments (20 cm and larger) will have a disk shape. The fragment mass density distribution will vary, depending on the colliding objects.

6.2.2  Determination of Fragment Spread Velocity

To obtain a relationship between a smaller mass of fragment and its velocity to a larger mass of fragment and its velocity, it has been assumed that the kinetic energies are equally imparted such that

$$\frac{1}{2} m_1 v_1^2 = \frac{1}{2} m_2 v_2^2 \tag{95a}$$

or

$$\frac{v_2}{v_1} = \left( \frac{m_1}{m_2} \right)^{1/2} \tag{95b}$$

where $m_1$ and $m_2$ are arbitrary debris particles with velocities of $v_1$ and $v_2$, respectively. This assumption is based on the consideration that when a shock wave travels, it applies equal pressure along the front at a given time. It causes the material to break up in unequal sizes but imparts equal kinetic energy. However, this assumption is not valid for smaller-sized fragments (0.1 cm and smaller), because as the area on which pressure is applied by the shockwave becomes very small, the effectiveness of the shockwave is reduced. For large-sized fragments, this assumption is in agreement with the test results performed by PSI and produced by NASA (Fig. 34). Three curves are shown in this plot. One of them is for the nominal case, and the other two curves are for extreme cases showing the upper and lower limits of the spread velocities of the fragments. In general, the nominal behavior can be assumed.

76
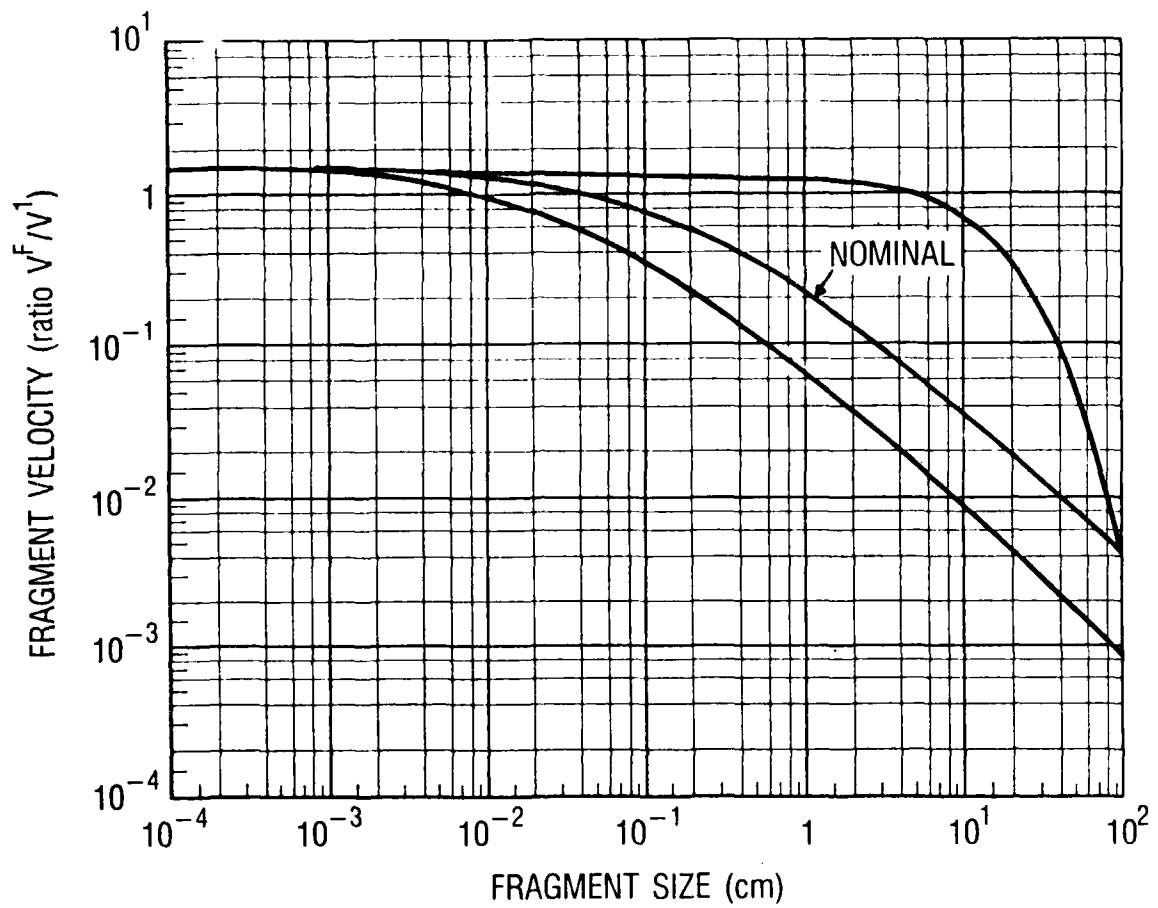
$V^F$ = fragment velocity

$V^1$ = relative velocity at impact

Figure 34. Model: On-Orbit Debris Total Velocity for Body-to-Body Impact

It is also important to account for the total mass involved before and after the collision. This methodology can be used to determine the number of fragments, their masses, and corresponding velocities. Size is determined using mass density criterion for a fragment of given mass and shape.

## 6.3 SUMMARY

The methodology presented in this analysis can be used in determining the number of fragments, their masses, and corresponding spread velocities as well as sizes. This, in turn, allows a better estimate of the collision probability posed by these debris particles.

## 6.4 PROGRAM IMPACT

The algorithms presented in Sections 4, 5, and 6 have been coded into a user-friendly, menu-driven IBM PC software package, entitled IMPACT. This program. guides the user through the breakup phase of several different scenarios. It allows the user to specify such things as energy dissipated in a breakup (percent of kinetic energy converted to heat and light), initial conditions in several forms of orbital elements, and masses of objects breaking up. Throughout the duration of the execution, the user is allowed to view tabular and graphical outputs, such as the relationships between numbers of particles, sizes, spread velocities, and particle orbital parameters, which are very useful to the analyst. The resulting output of this program is a properly formatted input file for the program DEBRIS (to be discussed in Section 8). The utility of this software is that numerous calculations, previously done on an ad hoc basis, are combined into an integrated, easy to use, software package.

## 7. SPACE VEHICLE BREAKUP DYNAMICS IN HYPERVELOCITY COLLISION--A KINEMATIC MODEL

Development of a hazard model for on-orbit breakups must necessarily be approached with great discipline and care, since abstractness of the results and difficulty in gathering physical evidence make it likely that very gross errors in the model may pass undetected, even after the event. This is particularly true in the case of near-term hazards, i.e., those extant during the first few hours and days after the breakup. The transient hazards in localized regions (near the "pinch points") typically run up to several orders of magnitude above the long-term average. Furthermore, their magnitude, location, and duration are highly sensitive to the initial characterization of the breakup and the number and distribution of initial fragment state vectors resulting from the breakup.

Sections 5 and 6 provide, in principle, a representation of a very simple breakup model originally developed by NASA which, until now, has been used extensively in the orbital debris community. (We shall therefore refer to this subsequently as the "NASA" model, although this is an Aerospace interpretation.) This model is based on an assumption that collision results are adequately represented by a spherically symmetric distribution of fragment velocities about the system center of mass velocity of the two colliding objects. An inverse relation is assumed to exist (Fig. 34) between fragment size and velocity relative to the center of mass. However, experimental observations have exhibited, in general, a more complex structure to the fragment cloud formation than this representation is able to reflect. Furthermore, in many cases, large fragments would have to survive enormous accelerations to arrive at velocities near the center of mass, a behavior which is not supported in theory or observation.

These differences became important in the characterization of hyper-velocity collisions of extended bodies, such as spacecraft, and the calculation of the resultant hazards. While these differences are largely washed out in the very long-term projections of fragment populations, overlooking details of the initial conditions of breakup can lead to significant understatement and/or

mislocation of peak fragment densities and resultant hazards in the near term. In this section, we present a new collision model, referred to as the Aerospace kinematic model, which provides an improved characterization of such collisions. We further explore results of incorporating the kinematic model in a cohesive hazard model for such events and contrast these with results obtained using the older model.


## 7.1    BACKGROUND

Hypervelocity collisions of space vehicles present a problem whose study has been limited by the difficulty in accurately modeling such events. Elaborate hydrocode models are required for direct analysis of collisions between even the simplest of objects; the results generally have large uncertainties. When the colliding objects are extended and complex in structure and mass properties, such models tend to become unmanageable. However, if one is interested only in the far-field effects of the collision, some insight may be obtained by examining the collision dynamics qualitatively to identify degrees of freedom and gross constraints on the mechanical properties of the collision. The problem is thereby simplified to one of managing the system's available momentum, energy, and mass within identifiable constraints. One can then evaluate sensitivity of the post-collision states to variation of parameters associated with the assumed degrees of freedom. To accomplish this, a transfer function must be defined relating the pre- and post-collision states in terms of these parameters as constrained by the conservation laws. In this way, the range of possible outcomes of an event can be examined without the necessity of modeling each condition individually, and parametric values can be sampled randomly for statistical analysis of the system. If the model parameters have been carefully chosen to have clear physical significance, then improved knowledge of the collision dynamics can easily be incorporated in the form of revised limits.

Consider the general properties of a collision depicted schematically in Figure 35. The volume of the larger object (target) is divided into two regions, shown in simplified cross section. The central region (unshaded) is the collision volume; i.e., the volume of material which participates directly

in the collision. The shaded region is the surrounding or noninvolved target volume. At initial contact, a set of hemispherical shock waves is generated over the collision interface, radiating in all directions from the locus of contact points. As long as collision velocities exceed the elastic wave propagation velocity in the medium, the advancing material overtakes the shock front ahead of it, and the materials of both objects are subjected to intense pressures at their interface. The local collision phenomena at this point are exceedingly complex and are dependent on the material properties, structure, and dynamics involved. However, certain gross properties seem to be common to all such collisions, strongly influencing the far-field distribution of resultant fragments. Local and near-field phenomena are then important only insofar as they are capable of shaping the far-field results.
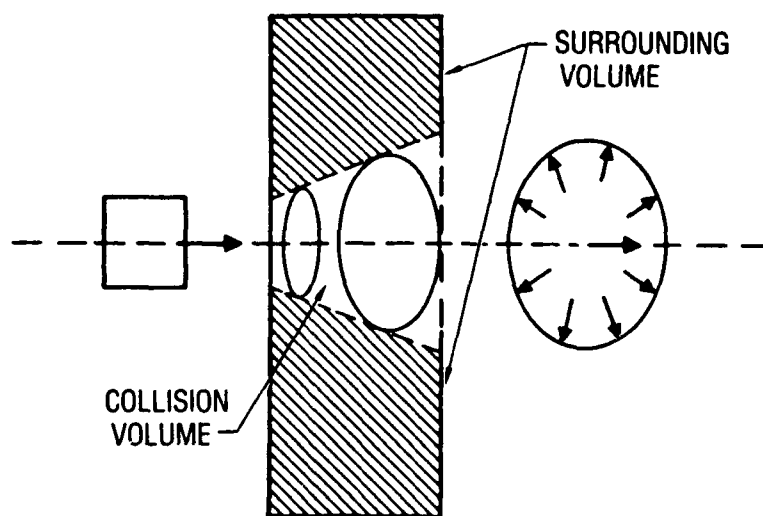


Figure 35. Schematic Depiction of a Collision

The material at the interface behaves as a fluid under pressure; this fluidity has the effect of disassociating the collision volume and the surrounding material of the larger object. Nearly all of the momentum transfer is confined to the collision volume, the material directly in the path of the expanding collision front, where the collision is totally inelastic and the

81

two objects combine to behave as a single mass. Energy is transferred to the noninvolved volume (i.e., the material not directly in the path of the collision) in a secondary interaction that involves shock waves, explosive forces, multiple secondary collisions, and shear forces in a transition region between the two zones.

This process continues until the collision mass exits the larger object, at which point the internal energy of the collision is released in a radial expansion of the now unconfined material in finely divided fragments in the solid, liquid, and gaseous states. The noninvolved volume experiences a lower intensity, explosive breakup into fragments of various sizes, which are accelerated radially from its center of mass and the collision axis by the fraction of collision energy transferred to it. This fraction increases with the ratio of target depth to projectile dimensions along the collision axis. If this ratio is small, the target is fully penetrated, and only a small fraction of the collision energy goes into explosive breakup of the surrounding target volume.

With increasing penetration depth, momentum transfer reduces the relative velocity of the collision front. If the depth ratio is sufficiently large, the collision velocity falls below the elastic wave velocity, and the collision is fully absorbed by the target. For much larger targets, ejection of material from the collision takes the form of cratering, with the collision mass ejected back along the negative collision axis and a net elastic reaction between the target and ejecta.

Empirical demonstration of these properties may be found in a great variety of test cases. Figure 36 clearly shows (a) the differentiation of the collision and surrounding target volumes in a small-scale, hypervelocity penetration; and (b) their contrasting breakup characteristics (that of the collision volume being far more energetic). Figure 37 shows an example from the opposite end of the scale, a head-on collision between a full-sized aircraft and missile observed at White Sands Missile Range in 1978. The

82
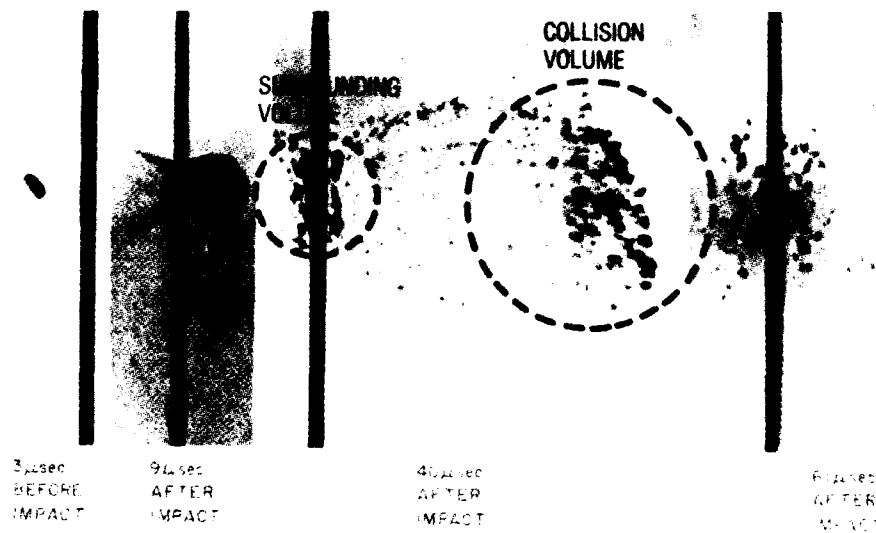
Figure 36.   Flash X-Ray Series, 1-g Titanium Disc (impacting at
~ 4.6 km/sec on 0.100-in. 2014-T6 aluminum target plate)*
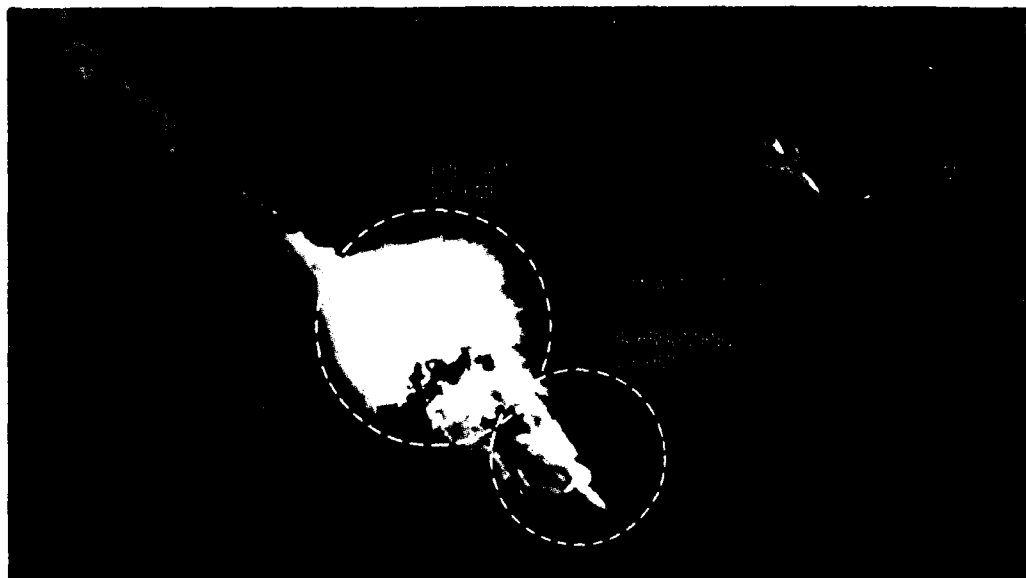


Figure 37.   Aircraft-Missile Test, 1978 (closing velocity 2 km/sec)

*Photograph from Ref. 17

relative velocity of the collision was about 2 km/sec, and the aircraft/missile mass ratio was about 30:1. The missile was inert at the time of the collision, since it had exhausted its fuel and carried no warhead. While a great many subscale hypervelocity collision tests have been conducted and extensively reported in the literature, empirical data on large-scale collisions are very meager. The best-documented examples are ground tests conducted at Arnold Engineering Development Center by PSI (Ref. 13); the ASAT intercept test (Ref. 14); a HOE flight test (Ref. 15); and the Delta-180 flight test (Ref. 16). Because of instrumentation limitations, each of these provided only very limited data with respect to fragment distribution.

Qualitative features common to these examples, and clearly evident in Figures 36 and 37, include a distribution of fragment sizes and velocity components along the collision axis (relative velocity vector) which is very nonsymmetric and dissimilar to the distribution of normal components; the components exhibit some degree of rough cylindrical symmetry about the collision axis. The largest fragments continue close to the trajectory of their parent object (as one would expect, since the fact that they remain intact indicates these are the least disturbed by the collision forces). The fragments basically are organized into two groups: a rapidly expanding radial distribution of large numbers of finely divided fragments about the centroid velocity of the collision mass, and a less energetic expansion of smaller numbers of larger fragments about a centroid close to the target velocity. This suggests a collision model which produces a bimodal fragment distribution incorporating these features and symmetries.

## 7.2   KINEMATIC MODEL

In an inertial reference frame, two objects of mass $M_1$ and $M_2$ approach their joint center of mass at velocities $\vec{V}_1$ and $\vec{V}_2$, respectively, as illustrated in Figure 38. It is convenient to describe the motion of the system of particles relative to the center of mass (CM) of the system.
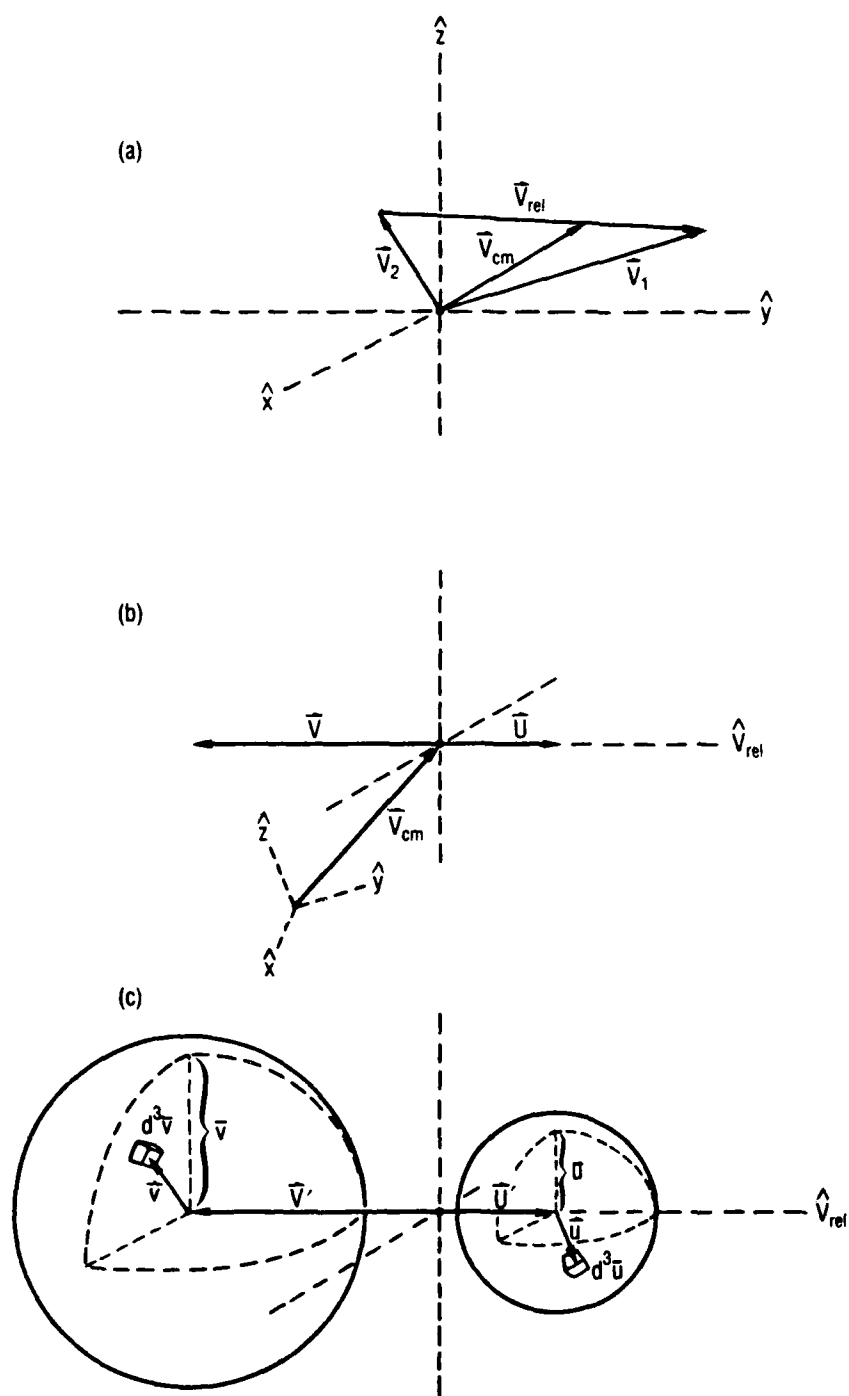
Figure 38. Incident and Resultant Geometries

Taking advantage of symmetry, the CM coordinate system is chosen with one axis oriented along the relative velocity vector, $\vec{V}_{rel} = \vec{V}_1 - \vec{V}_2$. Let $\vec{U}$ be the velocity of $M_1$ and $\vec{V}$ that of $M_2$ in the transformed system. Then

$$\vec{U} = \frac{M_2}{M_1 + M_2} \vec{V}_{Rel} = U\hat{V}_{Rel} \qquad (96)$$

$$\vec{V} = \frac{-M_1}{M_1 + M_2} \vec{V}_{Rel} = V\hat{V}_{Rel} \qquad (97)$$

In CM coordinates, the total linear momentum of the system is zero

$$\sum_i \vec{P}_i = \sum_i m_i \vec{V}_i = M_1\vec{U} + M_2\vec{V} = 0 \qquad (98)$$

and the total system kinetic energy is

$$KE_{sys} = \frac{1}{2} \sum_i m_i \mid \vec{V}_i \mid^2 = \frac{1}{2} (M_1 U^2 + M_2 V^2) \qquad (99)$$

Since the coordinate system is inertial, all velocities prior to and following the collision are constants. Accelerations during the collision are assumed to be instantaneous.

Immediately after the collision, the system is described as consisting of two translating, nonrotating, uniformly expanding spheres, each comprising a constant, continuous, undifferentiated distribution of mass in velocity space. These spheres represent the respective mass distributions of the noninvolved target volume and the collision volume.

Let the quantities $(M_1', \vec{U}', \bar{u},)$ and $(M_2', \vec{V}', \bar{v})$ identify the mass centroid translational velocity and surface radial expansion rate (spread velocity) of each of the two resultant spheres in the CM system (Fig. 38c).* Application of the conservation laws provides the following constraints.

_____

*In this section, the barred notation $(\bar{u}, \bar{v}, \bar{r})$ is used to denote a specified value (e.g., extreme or mean) of a scalar quantity, rather than a vector.

Conservation of mass:

$$M_1' + M_2' = M_1 + M_2 \tag{100}$$

Conservation of linear momentum:

$$M_1' \vec{U}' + M_2' \vec{V}' = 0 \tag{101}$$

Conservation of energy:

$$\frac{1}{2}(M_1 U^2 + M_2 V^2) = \frac{1}{2} M_1' U'^2 + \frac{1}{2} M_2' V'^2$$

$$+ \frac{1}{2} \iiint \rho_1 (\vec{u} \cdot \vec{u})^2 d^3u$$

$$+ \frac{1}{2} \iiint \rho_2 (\vec{v} \cdot \vec{v})^2 d^3v + Q_{loss} \tag{102}$$

In Eq. (102), $\vec{u}$ and $\vec{v}$ are velocities of the volume elements $d^3u$ and $d^3v$ relative to the sphere centroids $\vec{U}'$ and $\vec{V}'$, respectively. The $\rho_1(\vec{u})$ and $\rho_2(\vec{v})$ are mass densities of each sphere as a function of velocity relative to the respective sphere centroids, while $Q_{loss}$ accounts for kinetic energy dissipated in the collision, i.e., converted to other forms (heat, light, etc.). Thus, the first two terms on the right represent the translational kinetic energy ($KE'_{trans}$) of the sphere centroids, and the second two terms represent the respective kinetic energies of spread about the sphere centroids ($KE'_{spread}$):

$$KE_{sys} = KE'_{trans} + KE'_{spread} + Q_{loss} \tag{103}$$

Definition of $\rho_1(\vec{u})$ and $\rho_2(\vec{v})$ presents some difficulty, since no experiments have been conducted which measure distribution of material density in an expanding debris cloud. Some experiments (e.g., Ref. 13) report observations of material distributed throughout the expanding cloud volume, but with no quantitative measurements that would lead to any conclusions as to the specific characteristics of this distribution. For the present, therefore, we

shall assume a uniform statistical distribution of mass density over expansion velocity in the process of cloud formation. This assumption is unlikely to result in drastic errors, even if the "correct" distribution should prove to be different.

$$\rho_1 (\vec{u}) = 3 M_1'/4\pi|\bar{u}|^3 = \rho_1 \qquad (104)$$

$$\rho_2 (\vec{v}) = 3 M_2'/4\pi|\bar{v}|^3 = \rho_2 \qquad (105)$$

Conservation of angular momentum dictates that the spheres be nonrotating, and $KE'_{spread}$ may be rewritten

$$KE'_{spread} = 2\pi \int_o^{\bar{u}} \rho_1 u^4 du + 2\pi \int_o^{\bar{v}} \rho_2 v^4 dv$$

$$= \frac{3}{10} M_1'\bar{u}^2 + \frac{3}{10} M_2'\bar{v}^2 \qquad (106)$$

Then the system energy is

$$\frac{1}{2}(M_1 U^2 + M_2 V^2) = \frac{1}{2} M_1'(U'^2 + \frac{3}{5}\bar{u}^2) + \frac{1}{2} M_2'(V'^2 + \frac{3}{5}\bar{v})^2 + Q_{loss} \qquad (107)$$

## 7.3    TRANSFER FUNCTIONS

We now define a system of transfer functions expressing the post-collision state ($M_1'$, $M_2'$, $U'$,$V'$, $\bar{u}$, $\bar{v}$) in terms of the precollision state ($M_1$, $M_2$, U, V) and a set of independent parameters governing the system degrees of freedom. Assume that $M_1$ is the target mass and $M_2$ is the projectile mass. Define a parameter $\gamma$ as the fraction of $M_1$ directly involved in the collision ($0 < \gamma < 1$). The mass of the noninvolved target volume is

$$M_1' = (1 - \gamma)M_1 \qquad (108)$$

Using Eq. (100), the mass of the collision volume is then

$$M_2' = M_2 + \gamma M_1 \qquad (109)$$

88

Combining Eqs. (108) and (109) with Eq. (101) places upper limits on magnitudes of the resultant centroid translational velocities in the CM system

$$|\vec{U}'| \leq |\vec{U}| \tag{110}$$

$$|\vec{V}'| \leq \frac{(1 - \gamma) M_2}{M_2 + \gamma M_1} |\vec{V}| \tag{111}$$

These upper limits are achieved if, in the collision, no translational kinetic energy is converted to kinetic energy of expansion.

Now, define a momentum transfer parameter $\varepsilon$ such that $1 - \varepsilon$ is the fractional part of positive and negative linear momentum components exchanged in the conversion of translational kinetic energy to kinetic energy of expansion ($0 \leq \varepsilon < 1 - \gamma$). Then

$$|\vec{U}'| = \varepsilon|\vec{U}|/(1 - \gamma) = A|\vec{U}| \tag{112}$$

$$|\vec{V}'| = \varepsilon|\vec{V}|/[1 - \gamma(M_1/M_2)] = B|\vec{U}| \tag{113}$$

with $A = \varepsilon/(1 - \gamma)$ and $B = \varepsilon/[1 + \gamma(M_1/M_2)]$.

The conversion of translational kinetic energy to kinetic energy of expansion must be apportioned between the two resultant masses. To retain maximum freedom in the apportionment, two more parameters, $\alpha$ and $\beta$, are introduced. These parameters govern the kinetic energies of expansion of the resultant masses $M_1'$ and $M_2'$, respectively. Combining Eqs. (108) through (113) with Eq. (107) then gives the following expressions for the spread velocities $\bar{u}$ and $\bar{v}$, respectively, of $M_1'$ and $M_2'$

$$\bar{u} = \alpha(1 - A)|\vec{U}| \tag{114}$$

$$\bar{v} = \beta(1 - B)|\vec{V}| \tag{115}$$

where

$$\alpha^2 \leq \frac{A}{M_2(1 - A)^2} \left\{ \frac{5}{3\varepsilon} \left[ M_1 + M_2 - \varepsilon(M_1 B + M_2 A) \right] - \frac{(1 - B)^2}{B} M_1 \beta^2 \right\} \qquad (116)$$

$$\beta^2 \leq \frac{B}{M_1(1 - B)^2} \left\{ \frac{5}{3\varepsilon} \left[ M_1 + M_2 - \varepsilon(M_1 B + M_2 A) \right] - \frac{(1 - A)^2}{A} M_2 \alpha^2 \right\} \qquad (117)$$

In Eqs. (116) and (117), the equality holds when mechanical energy is fully conserved, i.e., when $Q_{loss} = 0$ in Eq. (107). In this case, $\alpha$ and $\beta$ clearly are not independent; the value of one completely determines the value of the other. This is true for any fixed value of $Q_{loss}$.

Further definition of the new parameters $\alpha$ and $\beta$ is now obtained by accounting for $Q_{loss}$ and then ascribing a balance to $\alpha$ and $\beta$, which are mutually dependent.

Considering Eq. (103), a new parameter $\eta$ is defined as the fraction of energy theoretically available to $KE'_{spread}$ which is actually delivered to $KE'_{spread}$ (i.e., which is not absorbed by $Q_{loss}$). From Eq. (103)

$$\eta = 1 - \frac{Q_{loss}}{KE_{sys} - KE'_{trans}} = \frac{KE'_{spread}}{KE_{sys} - KE'_{trans}} \qquad (118)$$

Combining this with Eqs. (106), (114), and (115)

$$KE'_{spread} = \frac{3}{10} \left[ M_1' \alpha^2 (1 - A)^2 U^2 + M_2' \beta^2 (1 - B)^2 V^2 \right]$$

$$= \eta(KE_{sys} - KE'_{trans}) \qquad (119)$$

Thus, $Q_{loss}$ is accounted for in simultaneously scaling $\alpha$ and $\beta$ by a factor $\eta^{1/2}$. Clearly, $\eta$ always has a value between 0 and 1. Equation (116) can be rewritten as an equality

$$\alpha^2 = \frac{A}{M_2(1 - A)^2} \left\{ \frac{5\eta}{3\varepsilon} \left[ M_1 + M_2 - \varepsilon(M_1 B + M_2 A) \right] - \frac{(1 - B)^2}{B} M_1 \beta^2 \right\} \qquad (120)$$

90

with

$$\beta^2 \leq \frac{5\eta B}{3\epsilon M_1 (1 - B)^2} \left[ M_1 + M_2 - \epsilon(M_1 B + M_2 A) \right] \tag{121}$$

Finally, the values of the expansion parameters $\alpha$ and $\beta$ must be balanced. It has been assumed throughout that the incident bodies are inert, containing no significant energy sources such as explosives or fuel. (Even if such sources are present, they may well be negligible in comparison to the collision energy.) In this idealized system, then, all of the energy of expansion ($KE'_{spread}$) for both the collision volume ($M_2'$) and surrounding volume ($M_1'$) must originate in the collision volume. A proportion of this energy is transferred to the surrounding volume during the collision to account for its expansion, while the remainder accounts for expansion of the collision volume. (This is not intended as a discussion of the local mechanics of interaction between the collision volume and surrounding target volume. Rather, it is a way to describe the net effects of the interaction significant to the resultant far-field distribution of materials.) If no energy is transferred, $\alpha = 0$ and $\beta$ is maximized; likewise for $\bar{u}$ and $\bar{v}$, respectively.

Another parameter, $\lambda$, is now defined as the fraction of $KE'_{spread}$ transferred to $M_1'$ ($0 < \lambda < 1$). Then the inequality (121) is replaced by an equality

$$\beta^2 = \frac{5\eta(1 - \lambda)B}{3\epsilon M_1 (1 - B)^2} [M_1 + M_2 - \epsilon (M_1 B + M_2 A)] \tag{122}$$

Note that $\eta$ and $\lambda$ now have effectively supplanted $\alpha$ and $\beta$ as independent variable parameters.

Equations (108), (109), (112) through (115), (120), and (122) form a system of transfer functions which completely define the post-collision state ($M_1'$, $M_2'$, $U'$, $V'$, $\bar{u}$, $\bar{v}$) in terms of the precollision state ($M_1$, $M_2$, $U$, $V$) and four independent parameters ($\gamma$, $\epsilon$, $\lambda$, $\eta$). These parameters form a simple

expression of the system degrees of freedom in terms wherein physical significance is readily grasped:

| | |
|---|---|
| $0 < \gamma < 1$ | Mass transfer |
| $0 \leq \epsilon < 1- \gamma$ | Momentum transfer |
| $0 < \lambda < 1$ | Energy transfer |
| $0 < \eta < 1$ | Energy dissipation |

The cloud centroid velocities in the original inertial reference frame are then given by

$$\vec{V}_1' = U'\hat{V}_{rel} + \vec{V}_{cm} = U'\hat{V}_{rel} + (M_1\vec{V}_1 + M_2\vec{V}_2)/(M_1 + M_2) \tag{123}$$

$$\vec{V}_2' = V'\hat{V}_{rel} + \vec{V}_{cm} = V'\hat{V}_{rel} + (M_1\vec{V}_1 + M_2\vec{V}_2)/(M_1 + M_2) \tag{124}$$

Assignment of values to the parameters ($\gamma$, $\epsilon$, $\lambda$, $\eta$) for a particular problem is dependent upon the specific geometries and materials involved and the user's assumptions concerning the physics of the collision. Because the physics of collisions of complex bodies are poorly understood and difficult to predict, the best approach might take the form of a statistical or sensitivity analysis, to which the system described here lends itself particularly well.

Application of this model is not restricted to impacts of a small projectile in a large target; it is adaptable to other configurations. For example, a glancing or partial impact of two bodies of comparable dimensions may be handled by executing twice, allowing each body in turn to act as a target, while the involved portion of the other body acts as a projectile.

## 7.4   CALCULATION OF STATE VECTORS

The transition from a continuous mass distribution to discrete fragment states is accomplished in a series of steps. First, the expanding spheres are quantized into a large number of cells of equal mass. These are assigned

92

velocity vectors pseudorandomly such that the uniform, continuous distribution of mass over velocity is replaced by identical, discrete masses distributed randomly with uniform probability.

Consider a uniform sphere of radius R divided into N cells of equal volume. The volume of each cell is

$$W = 4\pi R^3/3N \tag{125}$$

Assume that the cells are subdivisions of M shells of outer radius $r_m$ ($m = 1, 2, \ldots, M$; $r_o = 0$; $r_M = R$) each containing $n_m$ cells. Then

$$W = 4\pi(r_m^3 - r_{m-1}^3)/3n_m \tag{126}$$

$$r_m = \left(\frac{n_m R^3}{N} - r_{m-1}^3\right)^{1/3} \tag{127}$$

The weighted mean radius of a shell of outer radius $r_m$ is then

$$\bar{r}_m = \frac{1}{2}\left(r_m^3 + r_{m-1}^3\right)^{1/3} \tag{128}$$

For the m-th shell, choose $n_m$ sets of direction cosines ($a_{i_m}$, $b_{i_m}$, $c_{i_m}$) as uniformly distributed random numbers between -1 and 1, and their opposites ($-a_{i_m}$, $-b_{i_m}$, $-c_{i_m}$), for $i_m = 1, 2, \ldots, n_m/2$. The uniform sphere is then approximated by the N cells of volume W having position vectors

$\pm r_m(a_{i_m}\hat{i}, b_{i_m}\hat{j}, c_{i_m}\hat{k})$.

A cell mass $\bar{m}$ is selected; the sphere representing the noninvolved volume is then approximated by setting $N = M_1'/\bar{m}$, $R = \bar{u}$. For the collision volume, set $N = M_2'/\bar{m}$, $R = \bar{v}$. This method absolutely conserves momentum and approximately maintains the mass distribution. Mass distribution and energy content cannot be maintained simultaneously in converting from a continuous to

a discrete and finite distribution of masses; therefore, this process necessitates a small loss of system energy. This generally may be accounted for by incorporation in $Q_{loss}$.

Next, a list of discrete fragment masses is generated for each volume (i.e., the collision volume and the noninvolved volume). The approach employed here is based on relationships documented in Reference 18. However, in incorporating this approach in the kinematic model, we have further developed and extended these relationships to form a self-consistent method of calculating a fragment list for any hypervelocity collision. In the process, potential inconsistencies observed in previous applications of these relationships are eliminated.

Reference 18 identifies differing relationships for fragment mass distributions resulting from explosive breakup and collision fragmentation as follows.

Explosion Fragments:

$$N(m > m_o) = K_1 M \exp\left(-K_2 m_o^{1/2}\right) \tag{129}$$

where N is the cumulative number of fragments having mass larger than $m_o$, and M is the total mass of the fragmented object. The constants $K_1$ and $K_2$ are defined differently for the largest fragments and those in a smaller size range, based on empirical data.

$$m_o > 1936 \text{ gm:} \quad K_1 = 1.71 \times 10^{-4}, \quad K_2 = 0.02056$$

$$m_o < 1936 \text{ gm:} \quad K_1 = 8.69 \times 10^{-4}, \quad K_2 = 0.05756$$

Collision Fragments:

$$(m > m_o) = K(M_e/m_o)^p \tag{130}$$

where K and p are constants defined empirically as $K = 0.4478$, $p = 0.7496$.

Here, $M_e$ is the "ejected mass," i.e., the mass which would be excavated from the target in a cratering impact if the target were very much larger than the projectile striking it, defined as

$$M_e = V^2 m_p \qquad (131)$$

where $m_p$ is the projectile mass, and V is the relative velocity magnitude at impact in Km/s.

As stated earlier, some inconsistencies have been found in past applications of Eqs. (127) through (129) to hypervelocity collision problems. Reference 19 notes that the larger fragments of a collision event are distributed per Eq. (129), while the smaller fragments are distributed per Eq. (130), so that the total distribution is a combination of the two. However, no rationale is given as to how the two distributions should be combined. Also problematic is the fact that unless the target has at least $V^2$ times the mass of the projectile, Eqs. (130) and (131) produce more than the available mass in fragments. Reference 18 circumvents this by stating that the target mass must be greater than 10 x $M_e$, but Reference 19 ignores this condition, applying the distribution to a breakup where the target and projectile are of comparable mass. Our integration of these observations with the kinematic breakup model incorporates a proposed resolution of these inconsistencies.

In the kinematic model, the low-intensity explosive breakup Eq. (129) is applied to the noninvolved target mass $M_1'$. To generate a fragment list, a minimal fragment size $m_0$ is identified, and the total number of fragments in a range between $m_i$ and $m_{i+1}$ is identified as follows:

$$n(m_i < m \le m_{i+1}) = K_1 M \left| \exp(-K_2 i^{1/2} m_0^{1/2}) - \exp[-K_2(i+1)^{1/2} m_0^{1/2})] \right|$$

$$= n\,(m_i') \qquad (132)$$

where $m_i = i\,m_0$; $m_i' = (2i+1)m_0/2$. A list is generated with $M = M_1'$ using each set of constants $(K_1, K_2)$. Fragments larger than 1936 gm are kept from

the (m > 1936 gm) list, and fragments from the (m < 1936 gm) list are kept from 1936 gm downward until $\sum$ (m < 1936 gm) = $M_1'$ - $\sum$ (m > 1936 gm). The two lists are then combined.

The collision fragment distribution Eq. (130) is similarly applied to the collision mass $M_2'$. A list is generated by

$$n(m_i') = K(V_{rel}^2 M_2/m_o)^P [i^{-P} - (i + 1)^{-P}] \qquad (133)$$

for very small $m_o$. Then fragment masses are accumulated from i = 0 up to i = I such that

$$\sum_{i=0}^{I} m_i' = M_2' \qquad (134)$$

and the remainder are discarded. This eliminates the problem posed by Eq. (131) when $M_e = V_{Rel}^2 M_2 > M_1 + M_2$.

Note that Eq. (131) is dimensionally incorrect. It is an empirically derived relationship which introduces the effect of collision energy variation into the resultant fragment mass distribution. Without the $V^2$ factor, Eq. (130) would produce the same fragment distribution for any projectile/ target combination, regardless of the kinetic energy of impact. The interpretation employed in the kinematic model preserves the effect of increased collision energy resulting in a breakup into larger numbers of smaller-sized fragments.

The basic cells must be no larger than the smallest fragment of interest from the fragment list. Combinations of cells are now accumulated to produce fragments approximating the fragment masses on the fragment list. This is accomplished by a random selection process which preserves the expected inverse relationships between fragment mass and velocity relative to the incident velocity of the body from which the fragment originates. Each fragment on the fragment list thereby is assigned a velocity which is the vector sum of the velocities of its component cells.

## 7.5    FRAGMENT DISTRIBUTION

As fragment size decreases, the numbers increase geometrically, so that tracking the individual state vectors of fragments becomes very impractical when one is interested in those of very small size. Furthermore, in order to utilize the results for statistical analysis, it is necessary to identify a statistical distribution $n(\vec{v},d)$, i.e., fragment number density as a function of fragment velocity $\vec{v}$ and size d. Although the overall fragment distribution is not (in general) spherically symmetric, often it can be broken down into components which can be treated as spherically symmetric about their own centroids. Then the vector velocity $\vec{v}$ can be replaced by a velocity magnitude $v = |\vec{v}|$ relative to the appropriate centroid, so that the distribution is simplified to a function $n(\vec{v},d)$ of two rather than four variables. The overall fragment distribution can then be constructed by the principle of superposition of the component distributions.

The output of the kinematic model is a distribution of number versus size $n_d(d)$ of all fragments above the minimal size of interest, individual fragment velocities down to the smallest size which is computationally manageable, and the centroid velocities ($\vec{U}'$, $\vec{V}'$) and surface radial expansion rates ($\bar{u}$, $\bar{v}$) for each of two spherical fragment distributions. The larger fragment velocities can be analyzed to obtain their statistical distribution $n_v(\vec{v}, d)$; but this distribution must be inferred for the small fragments, for which only the upperbound velocities ($\bar{u}$, $\bar{v}$) are given. Once a functional form $n_v(v,d_i)$ is identified for each size range $d_i \pm \Delta d$, the fragments of each size category within a velocity range ($v_1$, $v_2$) can be enumerated:

$$n_d(d_i \pm \Delta d) = \int_{v_1}^{v_2} n_v(v,d_i)dv \qquad (135)$$

Figure 39 illustrates an example of a fragment distribution generated by the kinematic model. Velocities are spherically symmetric about the centroid of expansion. A simple three-dimensional approximation of the distribution of fragments larger than 1 mm is obtained by superposition of three

97

isotropically distributed spheres of particles in velocity space having the following characteristics:

| Radius | No. of Fragments |
|--------|------------------|
| $V_1$  | $n_1$            |
| $V_2$  | $n_2 - n_1$      |
| $V_3$  | $n_3 - n_2$      |



Figure 39.  Fragment Distribution

$$n_3 = 3.2 \times 10^6 \text{ FRAGMENTS}$$

$$V_3 = 2000 \text{ m/sec}$$

$$V_2 = 800 \text{ m/sec}$$

$$n_2 = 1.2 \times 10^6 \text{ FRAGMENTS}$$

$$V_1 = 100 \text{ m/sec}$$

$$n_1 = 2 \times 10^5 \text{ FRAGMENTS}$$

$$n_j \; (v, \, d_0 = 1 \text{ mm})$$

$$= \sum_{i \geq 0} \int v_{j0} \; n_v \; (v, \, d_i) \; dv$$

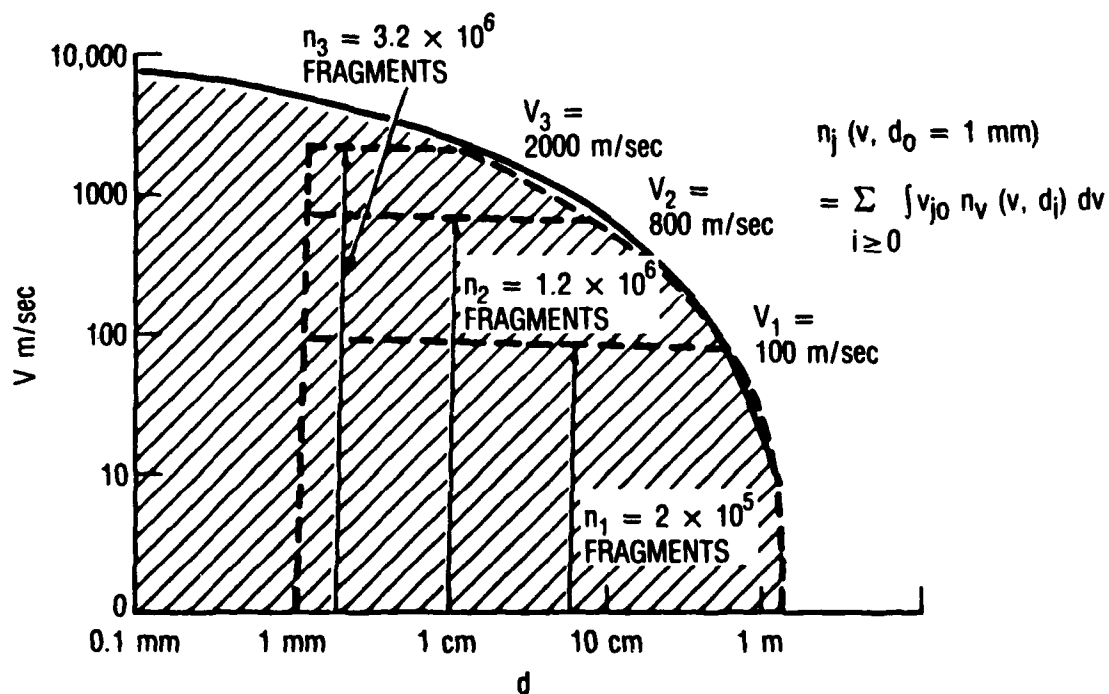## 7.6   EFFECT OF SECONDARY COLLISIONS

So far, it has been assumed that the collision and breakup occur instantaneously, and that the collision fragments emanate radially from a point source. In reality, the colliding bodies have finite dimensions, and the collision occurs over a finite time interval. While these properties can be ignored in describing the general motion of the resultant system of fragments, they do significantly influence the detailed distribution of fragments within the system. This is due to secondary interactions among the different components of the system very early (on the order of milliseconds) after the collision, when the dimensions of the colliding bodies are still significant compared to the distances traveled by the fragments.

Of particular importance is the physical observation that the larger fragments are generated external to the volume of the direct colliding masses. If the spread velocity of the fragments emanating from the hypervelocity collision volume exceed the relative velocity of the centroids of the collision and explosive breakup volumes, some fraction of the hypervelocity collision fragments will overtake and undergo secondary collisions with the explosive fragments. Assuming a fair degree of inelasticity in these secondary interactions, one can expect the collision fragments to give up much of their kinetic energy (thereby lowering their velocities) relative to the generally larger and much more massive explosive fragments. This interaction also will impart momentum to the explosive fragments in directions radial to the collision centroid, but the large total mass ratio of the explosive fragments to the involved collision fragments results only in a small net velocity change to the larger fragments.

Physical evidence of this kind of interaction is found in an unreported observation from the PSI ground tests. In tests that had full penetration of the target, resulting in a collision centroid in positive relative motion along the collision axis from the target body, it was observed that the explosive breakup fragments from the noninvolved portion of the target body received a

net momentum component along the negative collision axis (in the direction from which the projectile had come), and large numbers of collision fragments were found in and around the larger fragments. While no attempt was made to quantify these observations, this negative component in the motion of the large target fragments is difficult to explain except by secondary momentum transfer from the spreading collision fragments.

As a result of such a secondary interaction, it may be expected that the distribution of the involved fraction of the collision fragments will be concentrated in the region of the explosive fragments, increasing the overall fragment density in that region. Calculation of this resultant distribution can be separated into two component problems: calculation of the fraction of collision fragments involved, and calculation of the resultant changes in individual fragment momenta. In both cases, exact solution would represent a very complex problem in statistical mechanics. Since precision and accuracy of results is no better for such a problem than that of the input information (fragment numbers, sizes, shapes, velocities, etc.), which in this case can only be grossly estimated, no such analysis is warranted or attempted here. A first approximation is arrived at by much simpler methods.

Suppose the collision phase of a breakup is completed at time $t = 0$ such that the collision fragments are uniformly distributed within a spherical volume whose surface is expanding uniformly at radial velocity of constant magnitude $\dot{R}$. At $t = 0$ the surface radius is $R_o$. Assume also that a body having apparent cross-sectional area A (as seen from the sphere centroid) is initially at distance $R_o$ from the sphere center and moving radially at constant speed $V < \dot{R}$ relative to the sphere centroid. Then, at any time after $t = 0$, the flux of particles through area S (i.e., colliding with the external body per unit time) is

$$\Phi (t) = \rho(t) \, S \, \Delta V(t) \tag{136}$$

where $\rho(t)$ is the number density collision fragments of per unit volume of the sphere, and $\Delta V(t)$ is the velocity differential between the external body

and fragments at a radius $R_O + Vt$ from the sphere centroid. If N is the total number of collision fragments

$$p(t) = \frac{3N}{4\pi(R_O + \dot{R}t)^3}$$ (137)

$$V(t) = \dot{R}\left[\frac{R_O + Vt}{R_O + \dot{R}t}\right] - V$$ (138)

The fraction of collision fragments involved in secondary collisions with the external body after $t = 0$ is then given by

$$q = \frac{1}{N}\int_O^\infty \Phi(t)dt$$

$$= \int_O^\infty \left\{\frac{3S}{4\pi\ (R_O + \dot{R}t)^3}\ \dot{R}\left[\frac{R_O + Vt}{R_O + \dot{R}T}\right] - V\right\}dt$$

$$= \frac{S}{4\pi R_O^2}\left(1 - \frac{V}{\dot{R}}\right)\ (V < \dot{R})$$ (139)

This assumes that S is constant. Further levels of detail (e.g., time variation of S, oblique orientation of surfaces, perpendicular component of initial displacement) are second-order considerations which do not greatly alter the result, except in the case where V is close to (or exceeds) $\dot{R}$; this would lead to a unique mathematical formulation for each scenario and geometric configuration studied.

The form of the scattering function likewise is unknown, being dependent on a great number of factors such as size, shape, composition, and orientation of the scattering (large) fragments. Elasticity of the scattering should be a function of the scattering angle; scattering near 180° from the direction of incidence is highly inelastic, while scattering at small angles may be highly elastic. From a classical scattering theory, if the scattering is treated as

101

isotropic on the average, then a crude estimate of the resultant velocity distribution can be obtained. If it is assumed that scattering at angles between 100° and 180° is essentially inelastic, the fraction of incident particles scattered in this range is

$$\frac{1}{2} \int_{100°}^{180°} \sin \theta \, d \theta \approx 0.4 \tag{140}$$

Thus, 40% of the scattered particles will give up all momentum relative to the scattering fragments, resulting in their capture within the velocity region of the large fragments. The remainder are assumed to be distributed at relative velocities out to $\dot{R} - V$ from the centroid of the scatterers.

As an example, Figure 40 illustrates the incident and resultant fragment velocities (as seen from above) from a hypothetical glancing collision between two orbiting bodies labeled A and B, whose orbits are mutually inclined at 20°. The bodies are assumed to be generally cylindrical, of similar dimensions, but with a mass ratio $M_A/M_B = 5/3$. The collision is assumed to occur with the body axes oriented parallel to the relative velocity vector and involve $\gamma_A = \gamma_B = 1/3$ the mass of each body. Figure 41 details the relative positions of the collision fragments and those of the lower intensity explosive breakup of the noninvolved portion of object A during the first second after the collision. If, in Eq. (139)

$$R_o = 1 \text{ m}$$

$$\dot{R} = 1.7 \times 10^3 \text{ m/s}$$

$$V = 10^3 \text{ m/s}$$

$$S = 3 \text{ m}^2$$

then the fraction of collision fragments intercepted by A is $q_A \approx 10\%$. From Eq. (140), about 4% of the total might be distributed within the velocity regime of the large fragments. The remaining 6% is estimated to lie within approximately 500 km/s of the centroid of the large fragments.
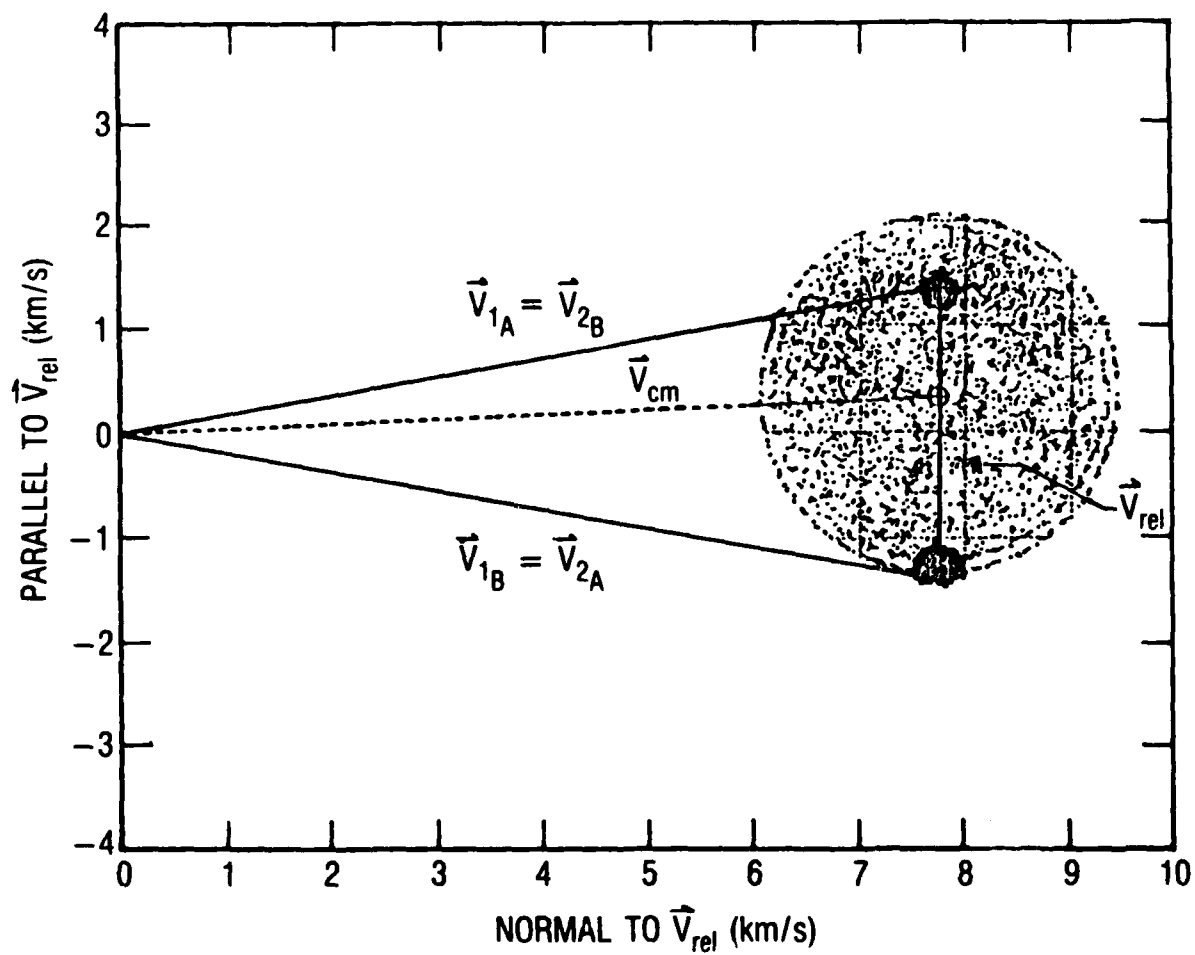
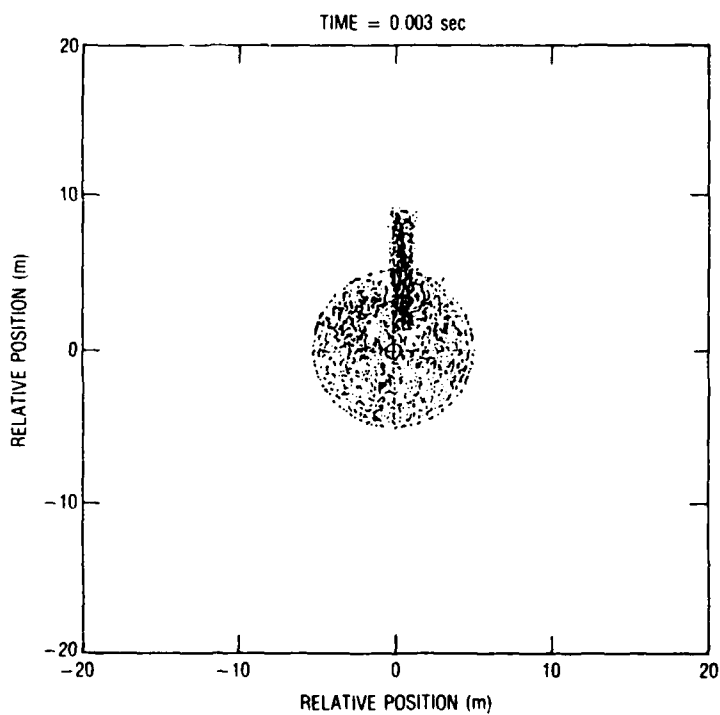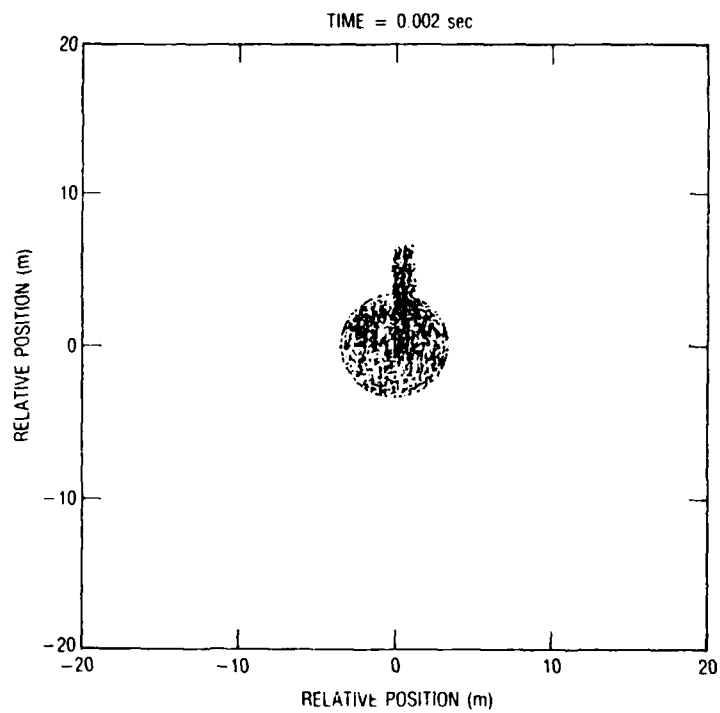Figure 40.   Fragment Distribution for Two Colliding Spacecraft

Figure 41.   Early Evolution of Debris Distribution
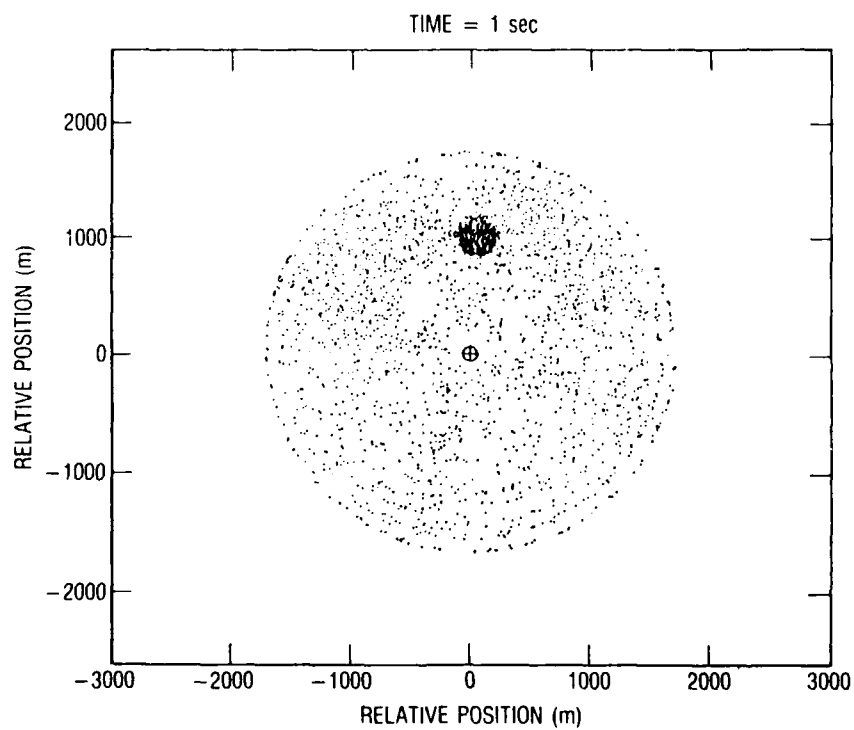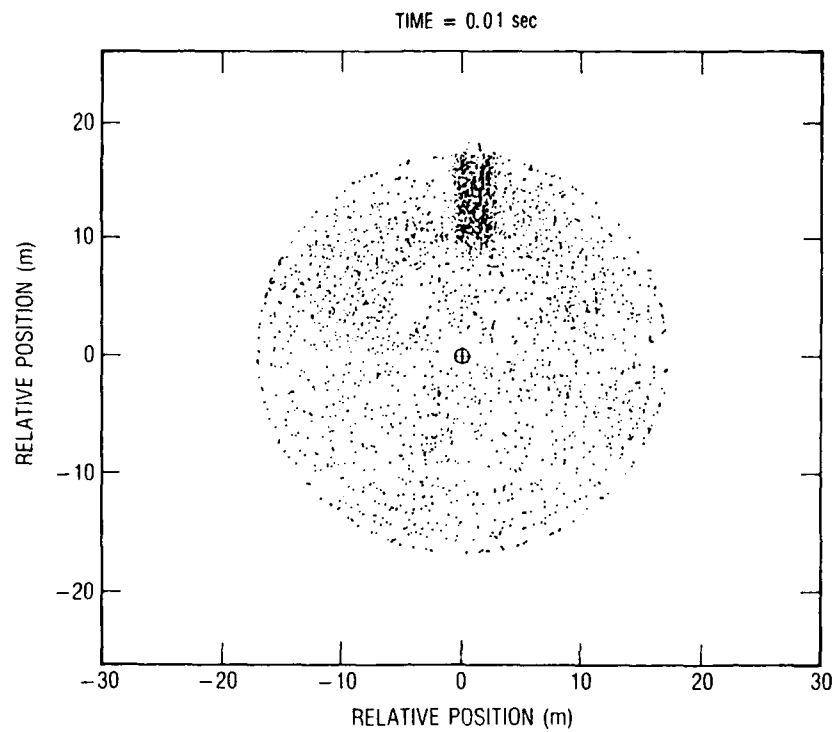
TIME = 0.01 sec

TIME = 1 sec

Figure 41.   Early Evolution of Debris Distribution (Continued)

Clearly, in this scenario, Object B represents a case where $V \approx \dot{R}$ and higher-order effects would dominate.

## 7.7   COMPARISON OF RESULTS WITH OTHER MODELS

The kinematic model has been employed to provide the hazard analysis predictions on two experiments to date involving actual spacecraft collisions: an ASAT test conducted in September 1985 and the Delta 180 test in September 1986. In both cases, analysis of the results showed very good agreement with the kinematic model predictions (Refs. 14, 16, 20, and 21).

In contrasting these results with predictions based on the "NASA" model, some important differences are observed. In Section 2, Tables 1 and 2 are two predictions of the results of the same collision. Table 1 is based on the older "NASA" model, while Table 2 was generated by the kinematic model and reflects Figure 39, neglecting fragments which will not survive one orbit. Figure 42 shows the probability of collision with a fragment larger than 1 mm in diameter for a spacecraft of 20 $m^2$ cross section passing through the centroid of the debris cloud represented by Table 2, at 90° mutual inclination (total angle between the orbit planes) with the centroid orbit. These results were obtained using the propagated cloud hazard model incorporated in the kinematic model companion tool, Program DEBRIS (described in the following section). Figure 42 shows the hazard for a single passage through the debris cloud center at any time during the first 24 hr after the collision event.

The most significant features of Figure 42 are the very large spikes in collision probability encountered at even revolutions, when the cloud is passing through the primary "pinch point," along with lesser rises observed at the half-revolution points. It is clear that time averaging of collision probabilities should be avoided when one is concerned with the actual hazard to be experienced by a spacecraft at a specific location and time. While the "average" hazard quickly falls below the level of hazard posed by the equivalent natural background flux of meteroids (dashed line), the peaks remain several orders of magnitude above this.
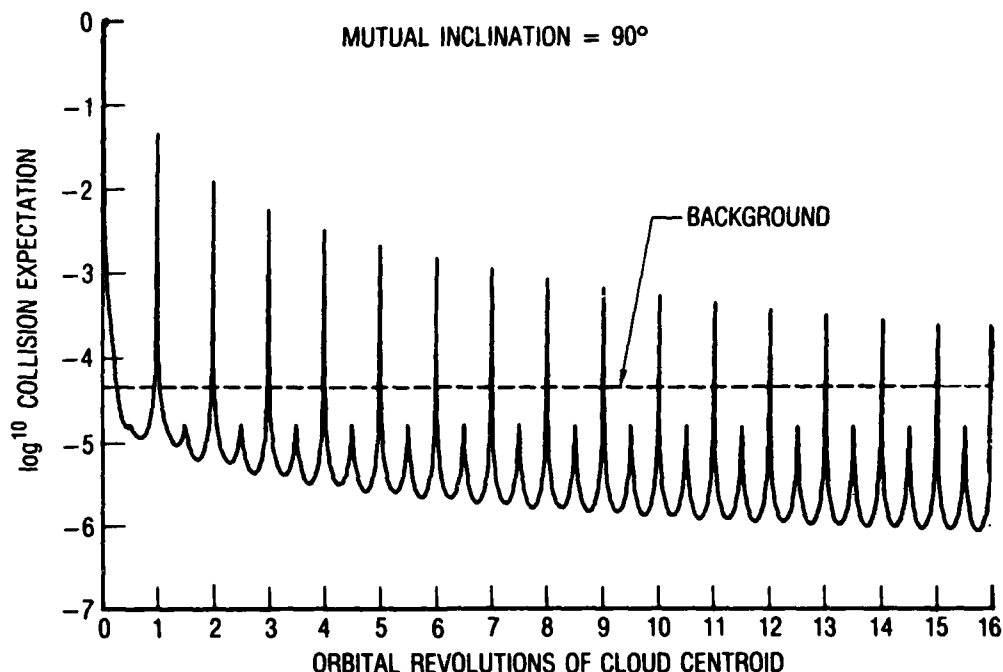
Figure 42. Collision Expectation versus Cloud Position

Figure 43 compares the propagated results based on initial conditions generated by the kinematic model with those of the "NASA" model. The upper curve (kinematic model) of Figure 43 is identical to Figure 42, with the horizontal scale expanded; the lower curve is based on Table 1, similarly propagated. Two significant differences are observed:

a. The overall lower level of hazard predicted by the "NASA" model during this interval, despite predicting a greater number of orbiting fragments, is due to the fact that all but a small fraction of these are assigned very high spread velocities, resulting in their more rapid dispersal.

b. Displacement of the "NASA" model peaks, relative to those of the kinematic model, is due to the "NASA" model forcing the cloud centroid and larger fragments to the system center of mass of the two colliding bodies, while the kinematic model possesses additional degrees of freedom to permit a bimodal distribution of multiple clouds with separate centroids. (In the particular case shown, the second cloud centroid is suborbital, and its associated fragments do not contribute significantly to the on-orbit hazards beyond the initial expansion.)

107
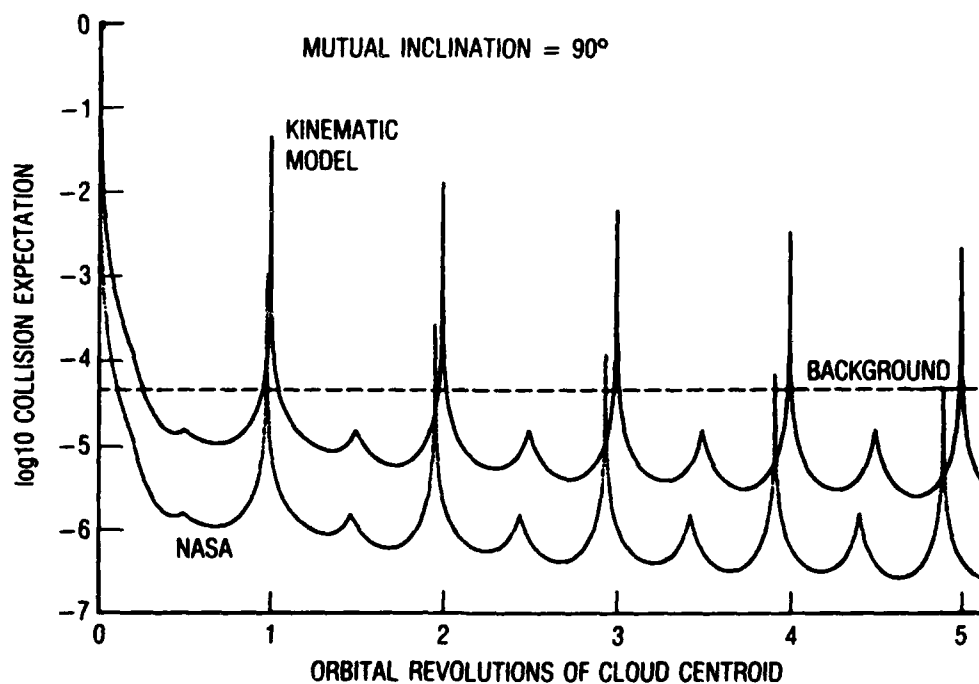
Figure 43. Comparison of Kinematic Model with "NASA" Model

## 7.8 CONCLUSIONS

As stated at the beginning of this section, the calculation of near-term
on-orbit debris hazards resulting from a collision of two spacecraft is highly
sensitive to initial characterization of the breakup.  Improvements in subse-
quent propagation of the debris clouds cannot improve the results if the
initial conditions are wrong.  The results shown in Figure 43 illustrate the
differences produced by differing characterizations of the same event, both in
the overall resultant hazard level and in the location of hazard peaks.

Identification of the "correct" overall or "average" level of hazard is
highly debatable and will remain so until much more definitive experimental
data on large-scale hypervelocity collisions become available.  More work needs
to be done in this area; however, high cost has been a factor in limiting
experimentation of this nature.

Section 7.7 shows plainly, however, that accuracy in locating the narrow regions of peak hazard is of more importance than the particular numerical value obtained. It is passage through these regions that will pose a significant hazard to resident spacecraft, regardless of the precise numerical level of that hazard. Protection of spacecraft from near-term hazards depends on the ability to predict and avoid coincidences with these regions.

Experimental evidence to date indicates that the kinematic model provides credible representations of the distributional structure (and therefore peak hazard regions) of debris clouds resulting from a spacecraft collision. This should be sufficient to justify its further application to such problems.

# 8. DESCRIPTION OF PROGRAM DEBRIS

## 8.1 INTRODUCTION

Program DEBRIS is described in this section. The program determines the intervals during which a given payload satellite travels through an expanding debris cloud and calculates the probability of collision associated with each transit. This section provides a general overview of program execution. Also included are detailed analyses of the algorithms used in DEBRIS. The necessary inputs to use the program are discussed, along with the types of information generated as output.

Program DEBRIS was developed to calculate the short- and long-term probability of collision of a given payload satellite whose orbit is in the vicinity of a newly formed debris cloud. The program determines the intervals during which the satellite travels through the expanding debris cloud and calculates the probability of collision associated with each transit. These probabilities are then combined to obtain the cumulative probability of collision, which is compared against the meteorite background to determine if a significant hazard exists.

An unlimited number of payload satellites may be examined by DEBRIS during program execution. A single maneuvering vehicle, such as the space shuttle, may also be simulated.

The expanding debris cloud is propagated using the model developed in previous sections. A number of sub-clouds, each composed of particles of uniform size, distribution, and separation velocity, have been used to represent a large debris cloud containing a diversity of particles.

## 8.2 PROPAGATION OF THE DEBRIS CLOUD

At time $t_I$, a target spacecraft breaks up, causing the formation of a debris cloud. At any subsequent time t, the debris cloud is modeled as a

111

torus extending along the trajectory of the target orbit with an elliptical cross section of varying dimension (Fig. 44). The center of the debris cloud travels along an orbit with the same elements as the former orbit of the spacecraft. The in-plane arc displacement between the leading and trailing edges of the cloud increases linearly with time until the torus closes. The cross-sectional dimensions of the cloud are functions of the total angular displacement between the point of interest and the point where the target spacecraft disintegrated.

PAYLOAD SATELLITE TRAJECTORY

POINT OF
CLOUD FORMATION
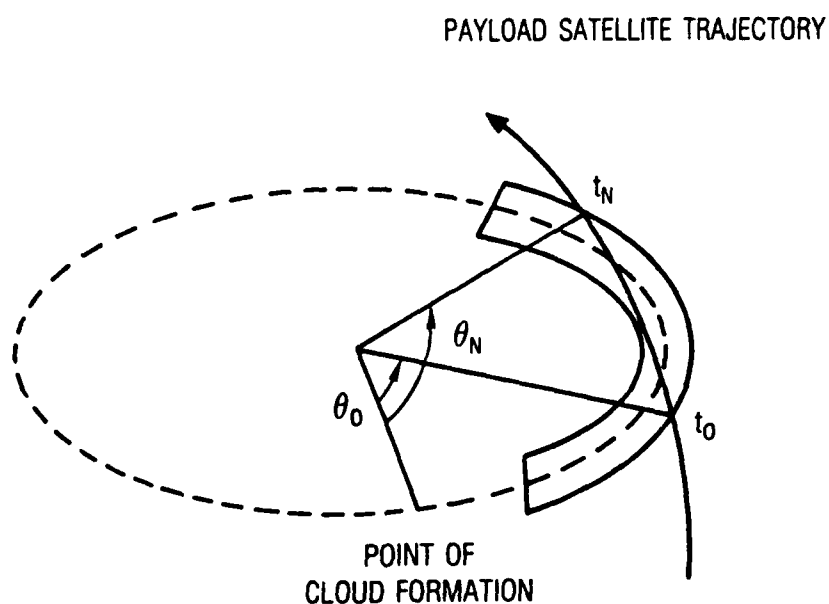
Figure 44. Debris Cloud Propagation Model

The volume of the debris cloud may be calculated using either of two methods. For purposes of calculating the probability of collision associated with the passage of a payload satellite through the cloud, the smaller of the two volumes will be used. This ensures that the collisional hazard due to the cloud is not underestimated.

It is possible to represent a debris cloud as the aggregate of several sub-clouds (Fig. 45). Each sub-cloud is composed of a different number of debris particles, of uniform size and propagation rate. The superposition of

112
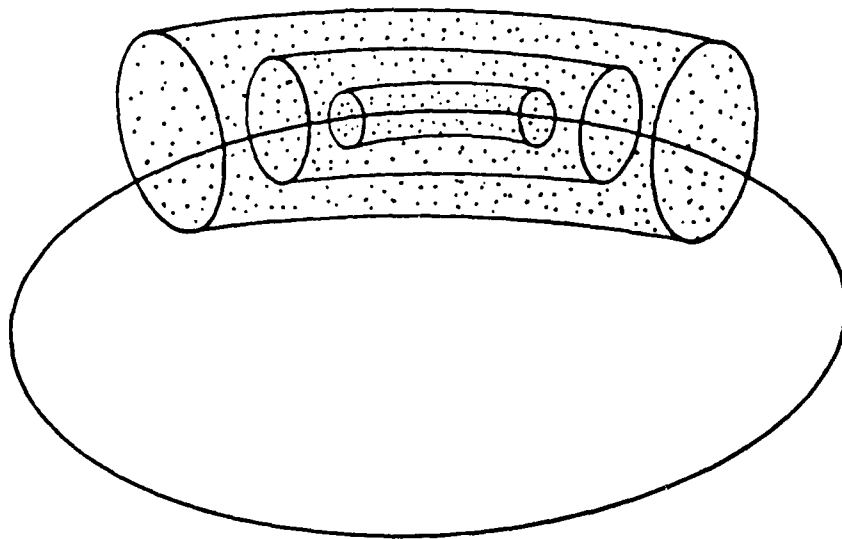
Figure 45.   Combination of Several Debris Clouds to Represent an
Aggregate Cloud of Varying Growth Rates

several sub-clouds, each with a different shape and density, is equivalent to
a larger cloud of nonuniform density.

## 8.3    EQUATIONS FOR DEBRIS CLOUD PROPAGATION AND VOLUME CALCULATION

For any time t measured from the time of cloud formation $t_I$, the
dimensions and volume of the debris cloud may be calculated using the
following equations.

It is assumed that the debris cloud grows at a uniform rate along the trajectory of the target orbit. For times prior to torus closure, the in-plane arc distance between the leading and trailing edges of the debris cloud is equal to

$$L(t) = (\dot{L}_1 + \dot{L}_2)t \qquad (141)$$

where

$\dot{L}_1$ = user-specified, leading-edge growth rate, km/min

$\dot{L}_2$ = user-specified, trailing-edge growth rate, km/min

The circumference C of an ellipse of semi-major axis a and eccentricity e is given by

$$C = 2\pi \sqrt{(1/2)\, a^2 (2 - e^2)} \qquad (142)$$

The time at which the torus closes ($t_{CL}$) may then be calculated as

$$t_{CL} = \frac{C}{(\dot{L}_1 + \dot{L}_2)} \qquad (143)$$

where C is the circumference of the target orbit.

For all times $t \leq t_{CL}$, the length of the torus L is equal to

$$L = (\dot{L}_1 + \dot{L}_2)t_{CL} \qquad (144)$$

At any given point within the leading and trailing edges of the cloud, the boundaries of the elliptical cross section are defined by Reference 22 as

$$a(t,\theta) = \sqrt{[a_{21}(t,\theta)]^2 + [a_{22}(t,\theta)]^2} \left(\frac{\Delta v}{\omega}\right) \qquad (145)$$

114

and

$$b(t,\theta) = a_{33}(t,\theta) \left(\frac{\Delta v}{\omega}\right) \qquad (146)$$

where

$a(t,\theta)$ = semi-major axis of elliptical cross section, km

$b(t,\theta)$ = semi-minor axis of elliptical cross section, km

$\theta$ = total angular displacement from point where target was broken up to point of interest [see Eq. (170)]

$\Delta v$ = expansion velocity of debris particles, km/sec

$\omega$ = orbital mean motion of the reference orbit, rad/sec

$a_{21}, a_{22}, a_{33}$ = functions previously introduced

In order to calculate the probability of collision associated with the passage of a payload satellite through the debris cloud, it is necessary to determine the volume of the cloud at different times. Assume that a satellite enters the cloud at time $t_o$ and angular displacement $\theta_o$, exiting the cloud at $t_N$, $\theta_N$ (Fig. 46). Then, for $t_o \le t \le t_N$ and $\theta_o \le \theta \le t_N$, the cloud volume is

$$VOL_1(t,\theta) = \frac{4\pi}{3} \left\{ |a_{11}(t,\theta) \, a_{22}(t,\theta)| + [a_{21}(t,\theta)]^2 \right\}$$

$$\ast \; a_{33}(t,\theta)\left(\frac{\Delta v}{\omega}\right)^3 \qquad (147)$$

where

$$a_{11}(t,\theta) = -3\omega t + 4 \sin \theta \qquad (148)$$

$$a_{21}(t,\theta) = 2[1 - \cos \theta + g_1(t,\theta) \, (1 + \cos \theta)] \qquad (149)$$

$$a_{22}(t,\theta) = \sin \theta + g_2(t,\theta) \, [SGN(\sin \theta) - \sin \theta] \qquad (150)$$

$$a_{33}(t,\theta) = g_3(t) + |\sin \theta| \qquad (151)$$

and

$$g_1(t) = \text{MIN}\left\{[C_1 t + C_4(\omega t - \sin\theta)], 1\right\} \tag{152}$$

$$g_2(t) = \text{MIN}\left\{\frac{1}{2}C_1 t + \frac{1}{2}C_4(\omega t - \sin\theta), 1\right\} \tag{153}$$

$$g_3(t) = \text{MIN}\left\{C_3 t, (a\,\omega\,\sin i\,)(\Delta v\,)^{-1}\right\} \tag{154}$$

where

$i$ = inclination of reference orbit, rad
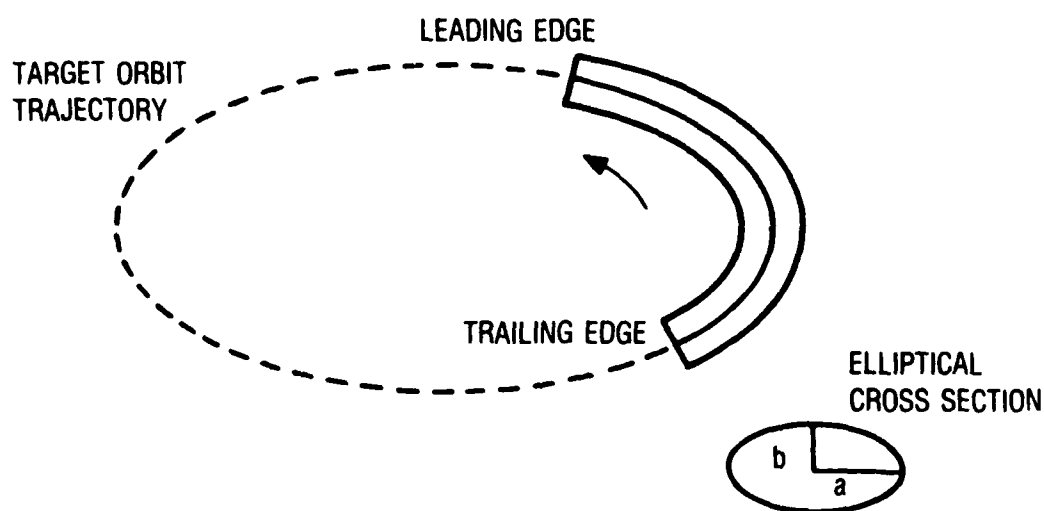
$C_1, C_3, C_4$ = constants discussed in Section 4



Figure 46. Geometry of a Typical Pass Through the Debris Cloud

The function SGN(X) is defined as

$$\text{SGN}(X) = \frac{X}{|X|}, \text{ if } X \neq 0$$

$$\text{SGN}(X) = 0, \text{ if } X = 0$$

116

The functions $g_1$, $g_2$, and $g_3$ model the effects of $J_2$ and drag on cloud propagation. As previously shown in Section 4, the constant $C_1$ incorporates the $J_2$ effect on the line of apsides, $C_3$ shows the $J_2$ effect on the line of nodes, and $C_4$ represents the effect of atmospheric drag. A second method for calculating the volume of the debris cloud for $(t,\theta)$ is

$$VOL_2(t,\theta) = \pi\, a(t,\theta)\, b(t,\theta)\, L(t) \tag{155}$$

where a, b, and L are calculated using Eqs. (141) and (142).

If the difference between the total angular displacement at entry $(\theta_o)$ and exit $(\theta_N)$ is less than $10°$, then the two volume functions are evaluated at entrance and exit and averaged

$$\overline{VOL}_1 = \frac{1}{2}[VOL_1(t_o, \theta_o) + VOL_1(t_N, \theta_N)] \tag{156a}$$

$$\overline{VOL}_2 = \frac{1}{2}[VOL_2(t_o, \theta_o) + VOL_2(t_N, \theta_N)] \tag{156b}$$

Otherwise, the two volumes are calculated from

$$\overline{VOL}_1 = \frac{1}{N} \sum_{i=o}^{N} VOL_1(t_i, \theta_i) \tag{157a}$$

$$\overline{VOL}_2 = \frac{1}{N} \sum_{i=o}^{N} VOL_2(t_i, \theta_i) \tag{157b}$$

where

$$N = 1 + INT\left(\{|\theta_N - \theta_o| + 2\pi\, INT[(t_N - t_o)(T)^{-1}]\} \Big/ \frac{10\pi}{180}\right)$$

$$t_i = t_o + (t_N - t_o)\left(\frac{i}{N}\right) \qquad (i = 0, 1, \ldots N)$$

$\theta_i$ = determined through propagation of payload orbit

T = period of reference orbit

The smaller of $\overline{VOL}_1$ and $\overline{VOL}_2$ is used for the computation of the probability of collision associated with $(t_o, t_N)$. However, if $(t_o + t_N)/2$ is greater than $t_{CL}$, then $\overline{VOL}_2$ is always used as the volume of the debris cloud.

## 8.4 DETERMINATION OF TRANSIT TIMES OF A SATELLITE THROUGH THE DEBRIS CLOUD

The time intervals during which a satellite is within the boundaries of the debris cloud may be determined from the simultaneous solution of two inequalities for all possible values of t

$$q_1 (t) \leq 0 \tag{158}$$

$$q_2 (t) \leq 0 \tag{159}$$

The function of $q_1(t)$ represents the distance from the payload satellite to the leading or trailing edge of the cloud, measured in the orbital plane of the debris cloud (see Fig. 47). The function $q_2(t)$ represents the out-of-plane distance from the payload satellite to the cross-sectional boundary of the debris cloud (see Fig. 48). It is necessary that both of these functions be nonpositive for the satellite to be inside the debris cloud at a given time.
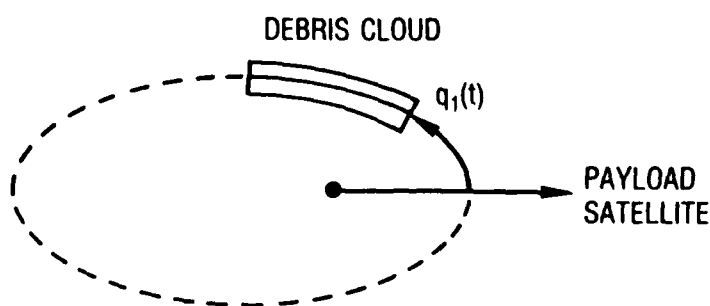


Figure 47. Illustration of $q_1(t)$

118

PAYLOAD SATELLITE

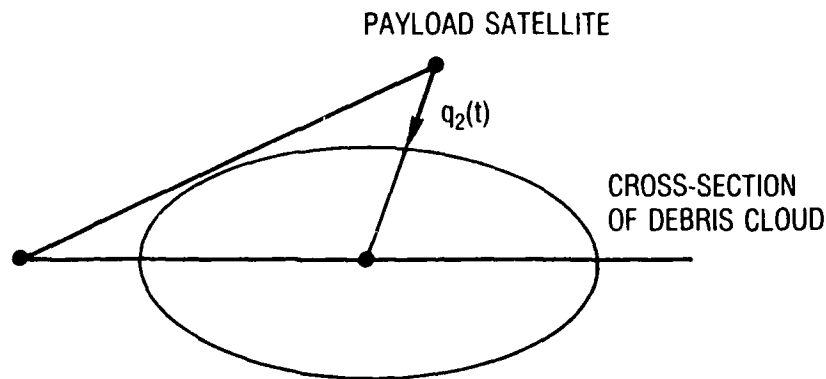$q_2(t)$

CROSS-SECTION
OF DEBRIS CLOUD

Figure 48.   Illustration of $q_2(t)$

The global set of time intervals corresponding to multiple passes of a satellite through the debris cloud may be found by solving Eqs. (158) and (159) separately and taking the intersection of the two sets of intervals as the result.   This is accomplished in Program DEBRIS using a Newton-Raphson iterative method.   The derivatives of $q_1$ and $q_2$ are numerically evaluated, with the convergence tolerance set to $10^{-4}$ km.

For any given time t, the position ($\vec{R}$) and velocity ($\dot{\vec{R}}$) of the center of the debris cloud can be determined by propagating the position and velocity of the target spacecraft from time $t_I$ to t.   A unit-vector normal to the target orbit plane (n) can then be defined as

$$\hat{n} = \frac{\vec{R} \times \dot{\vec{R}}}{|\vec{R}| \; |\dot{\vec{R}}|}$$

(160)

The current position ($\vec{R}_p$) and velocity ($\dot{\vec{R}}_p$) of the payload satellite also can be determined through propagation of the orbital elements specified at epoch for that satellite.   The projection ($\vec{Y}_p$) of the satellite position vector ($\vec{R}_p$) into the plane of the target orbit is defined as

$$\vec{Y}_p = \vec{R}_p - (\vec{R}_p \cdot \hat{n})\hat{n}$$

(161)

119

The angular separation of $\vec{R}$ and $\vec{Y}_p$, measured from $\vec{R}$, can then be calculated

$$\lambda = \left| \cos^{-1} \frac{\vec{Y}_p \cdot \vec{R}}{|\vec{Y}_p| \ |\vec{R}|} \right| \ \frac{\vec{R} \ x \ \vec{Y}_p}{|\vec{R}| \ |\vec{Y}_p|} \cdot \hat{n} \tag{162}$$

Using $\lambda$, the true anomaly of the projection $\vec{Y}_p$ with respect to the perigee of the reference orbit ($f_p$) is then calculated

$$f_p = f + \lambda \tag{163}$$

where f is the true anomaly of target (calculated from $\vec{R}$ and $\dot{\vec{R}}$). The radial distance to the intersection of $\vec{Y}_p$ and the reference orbit trajectory is given by

$$r_p = \frac{a(1 - e)^2}{1 + e \cos f_p} \tag{164}$$

where

        a = semi-major axis of the reference orbit

        e = eccentricity of the reference orbit

To evaluate the function $q_1(t)$, it is necessary to use incomplete elliptic integrals of the second type, which are defined in terms of a central angle rather than a focal angle (see Fig. 49). The central angle $\beta$ corresponding to the true anomaly of the reference f is calculated in three steps:

$$Q_2^2 = (ae)^2 + |\vec{R}|^2 + 2ae|\vec{R}| \cos f$$

$$\sin \gamma = \frac{ae}{2} \sin f$$
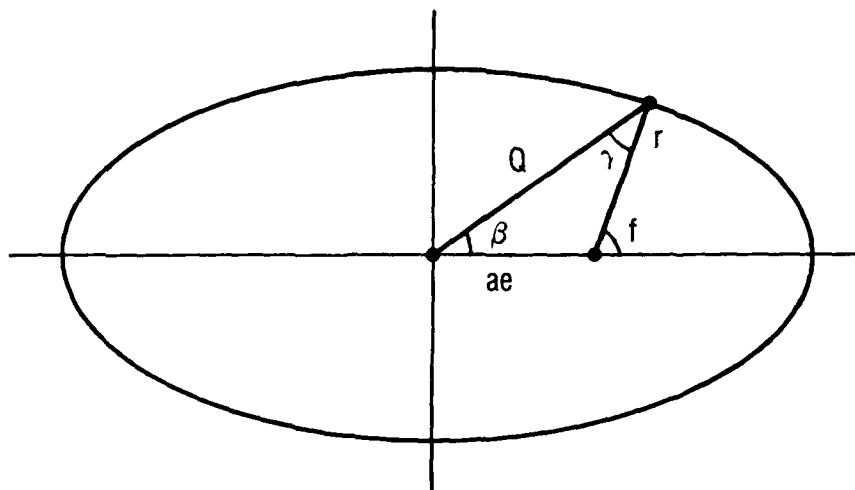
$$\beta = f - \gamma \tag{165}$$

Figure 49.  Relation Between Central Angle and Focal Angle

A similar procedure is used to find the central angle associated with the true anomaly of $\vec{Y}_P$

$$Q^2 = (ae)^2 + (r_p)^2 + 2ae \ r_p \cos f_p$$

$$\sin \gamma = \frac{ae}{Q} \quad \sin f_p$$

$$\beta_p = f_p - \gamma \tag{166}$$

The arc displacement $\Delta L$ between the center of the debris cloud and the projection of the satellite position vector onto the reference orbit plane can then be expressed as

$$\Delta L = a[E(\beta, \ e) - E(\beta_p, \ e)] \tag{167}$$

where the function $E(\beta, \ e)$ is defined as the incomplete elliptic integral of the second type

$$E(\beta, \ e) = \int_{0}^{\beta} \sqrt{1 - e^2 \sin^2 \phi} \ d \phi$$

121

For small values of eccentricity, Reference 22 provides a good approximate method for evaluating the integral

$$E(\beta, e) = \frac{1}{2}(1 + M)^{-1/2}\left[2\beta + \frac{M}{2}\sin 2\beta\right.$$

$$-\frac{M^2}{16}(2\beta + \sin 2\beta \cos 2\beta)$$

$$\left. +\frac{M^3}{48}(2\sin 2\beta + \sin 2\beta \cos^2 2\beta)\right]$$

$$+ 0(e^8) \tag{168}$$

where

$$M = \frac{e^2}{2 - e^2}$$

The function $q_1(t)$ (see Fig. 50) may then be evaluated as

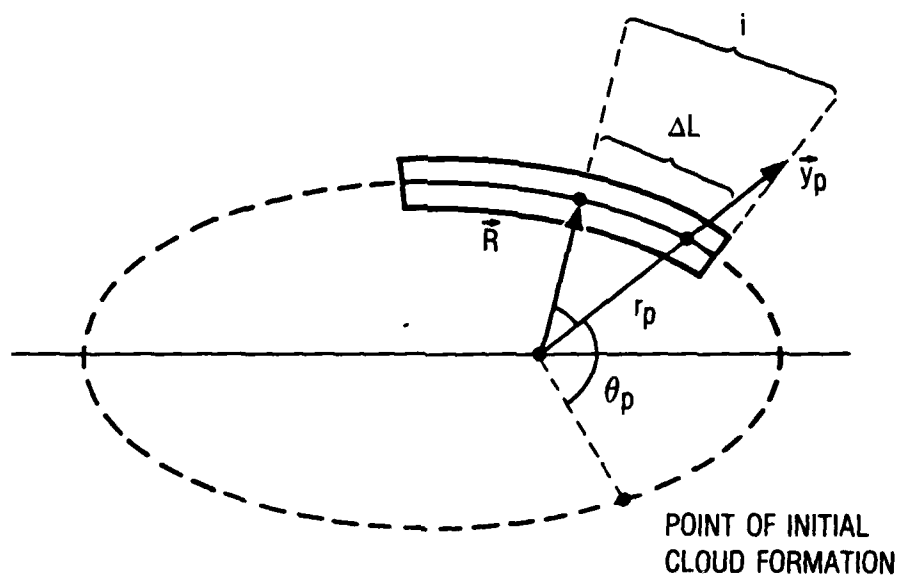$$q_1(t) = |\Delta L| - \dot{L}t \tag{169}$$



Figure 50.    Determination of Satellite Position
Relative to Planar Debris Cloud

122

If the angle $\gamma$ is positive, then the payload satellite is closest to the leading-edge boundary of the cloud and L should be set equal to the leading-edge growth rate, $\dot{L}_1$. If the angle $\gamma$ is negative, then $\dot{L}$ should be set equal to $\dot{L}_2$, the trailing-edge growth rate.

Whenever the function $q_1$ is less than zero, the projection of the payload satellite position vector is within the along-track limits of the debris cloud. Once the torus has closed ($t > t_{CL}$), $q_1$ is always negative.

The second necessary condition for the payload satellite to be inside the debris cloud is that the function $q_2$ be nonpositive. The previously calculated quantities $R_P$, $\vec{Y}_P$, $\vec{f}_P$, $\gamma$, and $r_P$ will be used in the evaluation of $q_2$.

The angular distance ($\Theta_P$) from $\vec{Y}_P$ to the point where the target spacecraft broke up is calculated by

$$\Theta_P = f_P - f^*\tag{170}$$

where $f^*$ is the true anomaly of the point where the spacecraft broke up.

A vector ($\vec{R}_D$) from the intersection of $\vec{Y}_P$ with the target reference orbit trajectory to the position of the payload satellite may be defined as

$$\vec{R}_D = \vec{R}_P - (r_P)\,\frac{\vec{Y}_P}{|\vec{Y}_P|}\tag{171}$$

The elevation angle ($\phi$) between $\vec{R}_D$ and $\vec{Y}_P$ may also be calculated

$$\cos\phi = \frac{\vec{R}_D \cdot \vec{Y}_P}{|\vec{R}_D|\,|\vec{Y}_P|}\tag{172}$$

Using Eqs. (145) and (146), one may calculate the axes of the elliptical cross section $a(t, \theta_p)$ and $b(t, \theta_p)$. The distance ($r_E$) from the reference orbit trajectory along $\vec{R}_D$ to the boundary of the cross section becomes

$$r_E^2 = b^2[1 - (a^2 - b^2)a^{-2} \cos^2 \phi]^{-1} \qquad (173)$$

The function $q_2(t)$ in Figure 51 may then be evaluated as

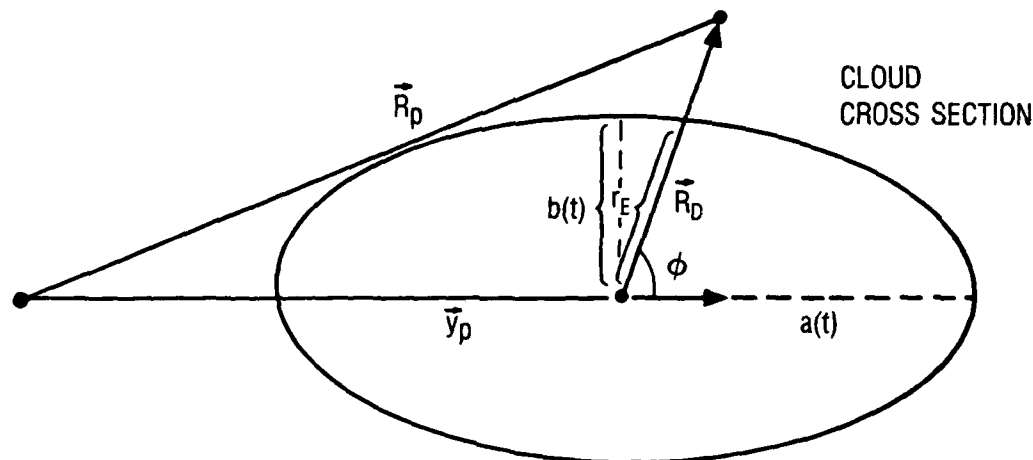$$q_2(t) = |\vec{R}_D| - r_E \qquad (174)$$

Figure 51.   Determination of Satellite Position
             Relative to Debris Cloud Cross Section

## 8.5   DETERMINATION OF COLLISION PROBABILITY

Once the set of time intervals has been determined during which the satellite is within the debris cloud, the probability of collision associated with each transit can be calculated. This probability is a function of satellite cross-sectional area, time spent in the cloud, relative velocity of the satellite with respect to the debris particles, average cloud density, and the total number of debris particles.

124

The cumulative probability of collision $(\bar{P}_i)$ for a satellite which travels through the i-th debris cloud a number of times can be defined as

$$\bar{P}_i = \prod_{j=1}^{M} (1 - P_j) \tag{175}$$

where $P_j$ is the probability of collision associated with the j-th passage through the cloud, and M is the total number of passes through the cloud.

For improved computational accuracy, Eq. (175) may be evaluated as

$$\bar{P}_i = 1 - EXP \left[ \sum_{j=1}^{M} \ln(1 - P_j) \right] \tag{176}$$

If an aggregate of debris clouds is being used to represent a larger cloud, then the procedures described previously must be applied separately to each sub-cloud. The resulting sets of time intervals are then used to calculate a cumulative probability of collision associated with each sub-cloud [Eq. (176)]. The overall probability of collision corresponding to the entire debris cloud (P) may then be calculated as

$$\bar{P} = 1 - EXP \left[ \sum_{i=1}^{N} \ln(1 - \bar{P}_i) \right] \tag{177}$$

where $\bar{P}_i$ is the cumulative probability of collision associated with the i-th sub-cloud, and N is the total number of sub-clouds.

## 8.6    EQUATIONS FOR DETERMINING COLLISION PROBABILITY FOR PASSAGE THROUGH THE DEBRIS CLOUD

This section describes the equations used to calculate the probability of collision associated with a particular passage of a satellite through a debris cloud.

Assume that a satellite enters a debris cloud at time $t_0$ and exits the cloud at time $t_N$. The position vector of the satellite at these two times $[\vec{R}_P(t_0), \vec{R}_P(t_N)]$ can be determined using methods previously described. The difference in true anomaly swept out by passage through the cloud may then be calculated as

$$\alpha = \cos^{-1} \left| \frac{\vec{R}_P(t_0) \cdot \vec{R}_P(t_N)}{|\vec{R}_P(t_0)| \; |\vec{R}_P(t_N)|} \right|$$

$$+ 2\pi \; INT[(t_N - t_0)(T)^{-1}] \tag{178}$$

where T is the period of the reference orbit.

The number of sub-intervals into which $\alpha$ will be divided may then be calculated as

$$N = 1 + INT \left| \alpha \left( \frac{10}{180} \right) \pi^{-1} \right| \tag{179}$$

An interval of 10° was chosen empirically.

The actual distance travelled by the satellite while inside the cloud $(d_S)$ may be approximated as

$$d_S = \frac{1}{N} \sum_{i=0}^{N} \alpha \; |\vec{R}_P(t_i)| \tag{180}$$

where $t_i = t_0 + (i/N) (t_N - t_0)$.

During that same interval, the distance travelled by the cloud $(d_C)$ is approximately equal to

$$d_C = (t_N - t_0) \frac{1}{N} \sum_{i=0}^{N} |v_P(t_i)| \tag{181}$$

126

The quantity $v_p(t_i)$ is the average velocity of debris particles near the satellite at time $t_i$ and is given by

$$v_p(t_i) = \sqrt{\mu(2/r_p - 1/a)} \qquad (182)$$

where a is the semi-major axis of the reference orbit, $\mu$ is the gravitational constant, and $r_p$ is calculated from Eq. (164).

The relative distance traveled by the satellites with respect to the debris cloud ($d_{rel}$) becomes

$$d_{rel} = d_S - \cos(\Delta i)d_C \qquad (183)$$

where $\Delta i$ is the difference in inclination between the satellite and target orbit planes.

The effective volume swept out by the satellite moving through the cloud ($VOL_p$) may then be calculated as

$$VOL_p = A_p|d_{rel}| \qquad (184)$$

where $A_p$ is the cross-sectional area of the satellite. The average volume of the debris cloud associated with the region of passage ($VOL_{CL}$) can be found using either method previously described. These volumes are used to compute the probability of collision associated with this partial passage through the cloud:

$$P = 1 - EXP\left[N_p \ln\left(1 - \frac{VOL_p}{VOL_{CL}}\right)\right] \qquad (185)$$

where $N_p$ is the total number of debris particles in the cloud.

127

# 9. EFFECTS OF ECCENTRICITY ON THE VOLUME OF A DEBRIS CLOUD

## 9.1 INTRODUCTION

During evaluation of the collision hazard posed by the debris from an orbital breakup of a spacecraft, it is necessary to define a region that the debris would occupy. This region is a time-varying volume, with each particle occupying a different orbit and all spreading out relative to each other.

The first approximation to this debris cloud volume assumes that, prior to breaking up, the spacecraft in question is in a circular orbit about the earth. Additionally, the linearized equations of motion are used, remaining valid for small changes in relative velocities and over a small number of orbits.

In this section, small values of eccentricity are added into the equations of motion. By using a differential correction process, similar to the work in Reference 23, one finds new functions involving the circular solution and the changes in that solution due to eccentricity. Additionally, the solution process allows for the orbital breakup to occur at any time throughout the elliptical orbit.

This continuing process to refine the volume model leads to a greater understanding of what is really happening, and allows for a more accurate assessment of the collision hazard posed by the debris.

## 9.2 ANALYSIS

The solution process involves a number of fundamental techniques, as well as some new ideas first introduced for this problem. Initially, the equations of motion from Newton's laws are formulated; from there, the solution is perturbed by adding eccentricity. The equations are linearized, and the state transition matrix relating position and initial relative

velocity is found. This procedure was used by Anthony and Sasaki (Ref. 24). Finally, using a method developed specifically for this problem, one finds the volume of the debris cloud.

Given an inertial frame (I) with origin at the center of the earth, and a rotating frame (R), with Y being in the radial direction and Z being in the out-of-plane direction as seen in Figure 52, the position vector of the target and i-th piece of debris, respectively, is

$$\bar{r} = r \, \hat{J} \tag{186}$$

and

$$\bar{R}_i = X\hat{I} + (Y + r) \, \hat{J} + Z\hat{K} \tag{187}$$

while the vector between the target and the debris is

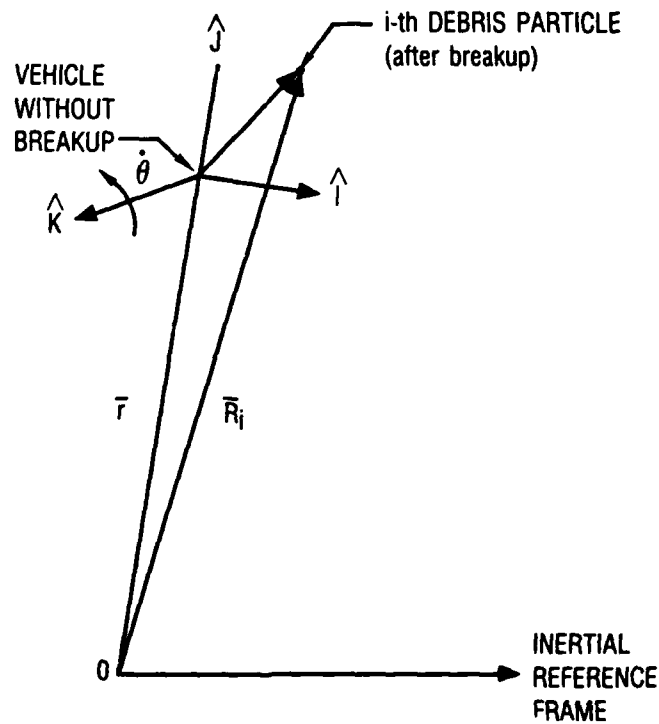$$\bar{R} = \bar{R}_i - \bar{r} = X\hat{I} + Y\hat{J} + Z\hat{K} \tag{188}$$



Figure 52.  Coordinate Frame

The differential equations in the inertial frame for this inverse square field are

$$\frac{d^2 \bar{R}^{(I)}}{dt^2} = m \left[ \frac{\bar{r}}{r^3} - \frac{\bar{R}_i}{R_i^3} \right] \tag{189}$$

The left side of Eq. (189) is obtained by taking the derivative of Eq. (188) in the inertial frame

$$\frac{d\bar{R}^{(I)}}{dt} = \frac{d\bar{R}^{(R)}}{dt} + \bar{\omega} \times \bar{R} \tag{190}$$

where

$$\frac{d\bar{R}^{(R)}}{dt} = \dot{X}\hat{I} + \dot{Y}\hat{J} + \dot{Z}\hat{K} \tag{191}$$

and

$$\bar{\omega} = \dot{\theta}\hat{K} \tag{192}$$

The second derivative of Eq. (190) in the inertial frame is

$$\frac{d^2 \bar{R}^{(I)}}{dt^2} = \frac{d}{dt} \left| \frac{d\bar{R}^{(R)}}{dt} \right| + \frac{d}{dt} (\bar{\omega} \times \bar{R}) \tag{193}$$

When the right-hand side of Eq. (189) is expanded and the individual components, are equated, the equations of motion become

$$\ddot{X} - Y\ddot{\theta} - 2\dot{Y}\dot{\theta} - \dot{\theta}^2 X + \frac{\mu X}{[X^2 + (Y + r)^2 + Z^2]^{3/2}} = 0 \tag{194a}$$

$$\ddot{Y} + X\ddot{\theta} + 2\dot{X}\dot{\theta} - \dot{\theta}^2 Y + \frac{\mu(Y + r)}{[X^2 + (Y + r)^2 + Z^2]^{3/2}} = 0 \tag{194b}$$

$$\ddot{Z} + \frac{\mu Z}{[X^2 + (Y + r)^2 + Z^2]^{3/2}} = 0 \tag{194c}$$

131

Nondimensional terms are introduced such that

$$x = \frac{X}{a} \tag{195}$$

$$y = \frac{Y}{a} \tag{196}$$

$$z = \frac{Z}{a} \tag{197}$$

$$\rho = \frac{r}{a} \tag{198}$$

$$\tau = \left(\frac{\mu}{a^3}\right)^{1/2} t \tag{199}$$

where a is the semi-major axis of the reference orbit, so Eqs. (194) reduce to

$$x'' - y\theta'' - 2y'\theta' - \theta'^2 x + \frac{x}{[x + (y + \rho)^2 + z^2]^{3/2}} = 0 \tag{200a}$$

$$y'' + x\theta'' + 2x'\theta' - \theta'^2 y + \frac{(y + \rho)}{[x^2 + (y + \rho)^2 + z^2]^{3/2}} = 0 \tag{200b}$$

$$z'' + \frac{z}{[x^2 + (y + \rho)^2 + z^2]^{3/2}} = 0 \tag{200c}$$

where ' (prime) represents differentiation with respect to $\tau$. Assuming that the distance between a debris particle and the target is much less than the semi-major axis, one finds that Eqs. (200) further reduce to

$$x'' - y\theta'' - 2y'\theta' + \left(\frac{1}{\rho^3} - \theta'^2\right)x - \frac{3xy}{\rho^4} = 0 \tag{201a}$$

$$y'' + x\theta'' + 2x'\theta' - \left(\frac{2}{\rho^3} + \theta'^2\right)y - \frac{3}{2\rho^4}(x^2 - 2y^2 + z^2) = 0 \tag{201b}$$

$$z'' + \frac{z}{\rho^3} - \frac{3zy}{\rho^4} = 0 \tag{201c}$$

132

For a slightly elliptical orbit, the series for $\theta$ and R are

$$\theta = \left(\frac{\mu}{a^3}\right)^{1/2} \left[1 + 2e \cos M + \frac{5}{2} e^2 \cos 2M + \ldots\right]$$

$$r = \left(\frac{\Delta v}{\omega}\right) \left[1 - e \cos M + \frac{e^2}{2}(1 - \cos 2M) + \ldots\right] \tag{202}$$

where

$$M = \left(\frac{\mu}{a^3}\right)^{1/2} (t - t_p) \qquad \begin{array}{l} (M \quad - \text{ mean anomaly}) \\ (t_p \quad - \text{ time of periapsis passage}) \end{array}$$

Nondimensionally, and retaining only linear terms, Eq. (202) becomes

$$\theta' = 1 + 2e \cos(\tau - \tau_p)$$

$$\rho = 1 - e \cos(\tau - \tau_p) \tag{203}$$

For the circular target orbit, the Clohessy-Wiltshire equations take the form

$$x_c'' - 2y_c' = 0 \tag{204a}$$

$$y_c'' + 2x_c' - 3y_c = 0 \tag{204b}$$

$$z_c'' + z_c = 0 \tag{204c}$$

Now, assuming a new solution for x, y, and z, in the form

$$x = x_c + \delta x \tag{205a}$$

$$y = y_c + \delta y \tag{205b}$$

$$z = z_c + \delta z \tag{205c}$$

When one takes appropriate derivatives, while retaining only linear terms, the new differential equations, in terms of the perturbations on x, y, and z, are

$$\delta x'' - 2\delta y' = e[(4y_c + x_c)\cos(\tau - \tau_p) - 2y_c \sin(\tau - \tau_p)] \tag{206a}$$

$$\delta y'' + 2\delta x' - 3\delta y = e[(10y_c - 4x_c')\cos(\tau - \tau_p) + 2x_c \sin(\tau - \tau_p)] \tag{206b}$$

$$\delta z'' + \delta z = -3ez_c \cos(\tau - \tau_p) \tag{206c}$$

Initially

$$\delta x(0) = \delta y(0) = \delta z(0) = \delta x'(0) = \delta y'(0) = \delta z'(0) = 0$$

Assuming a solution of Eqs. (206) in the form

$$\delta x = e[A_0 + A_1 \sin \tau + A_2 \cos \tau + A_3 \sin 2\tau$$

$$+ A_4 \cos 2\tau + A_5 \tau + A_6 \tau \sin \tau + A_7 \tau \cos \tau] \qquad (207a)$$

$$\delta y = e[B_0 + B_1 \sin \tau + B_2 \cos \tau + B_3 \sin 2\tau$$

$$+ B_4 \cos 2\tau + B_5 \tau + B_6 \tau \sin \tau + B_7 \tau \cos \tau] \qquad (207b)$$

$$\delta z = e[C_0 + C_1 \sin \tau + C_2 \cos \tau + C_3 \sin 2\tau$$

$$+ C_4 \cos 2\tau + C_5 \tau + C_6 \tau \sin \tau + C_7 \tau \cos \tau] \qquad (207c)$$

where

$$A_0 = -3x_o' \sin \tau_p - \frac{1}{2} y_o' \cos \tau_p$$

$$A_1 = 6y_o' \sin t_p$$

$$A_2 = 6x_o' \sin \tau_p + 2y_o' \cos \tau_p$$

$$A_3 = -\frac{3}{2}y_o' \sin \tau_p + 3x_o' \cos \tau_p$$

$$A_4 = -3x_o' \sin \tau_p - \frac{3}{2} y_o' \cos \tau_p$$

$$A_5 = -3y_o' \sin \tau_p - 3x_o' \cos \tau_p$$

$$A_6 = -3x_o' \sin \tau_p$$

$$A_7 = -3x_o' \cos \tau_p \qquad (208)$$

$$B_0 = -3y_o' \sin \tau_p - 4x_o' \cos \tau_p$$

$$B_1 = -x_o' \sin \tau_p - 2y_o' \cos \tau_p$$

$$B_2 = 4y_o' \sin \tau_p + 2x_o' \cos \tau_p$$

$$B_3 = 2x_o' \sin \tau_p + y_o' \cos \tau_p \qquad \begin{array}{l}(209)\\ \text{(cont.)}\end{array}$$

134

$$B_4 = - y_0' \sin \tau_p \cdot 2x_0' \cos \tau_p$$

$$B_5 = 0$$

$$B_6 = 3x_0' \cos \tau_p$$

$$B_7 = - 3x_0' \sin \tau_p \tag{209}$$

$$C_0 = - \frac{3}{2} z_0' \sin \tau_p$$

$$C_1 = - z_0' \cos \tau_p$$

$$C_2 = 2z_0' \sin \tau_p$$

$$C_3 = \frac{1}{2} z_0' \cos \tau_p$$

$$C_4 = - \frac{1}{2} z_0' \sin \tau_p$$

$$C_5 = 0$$

$$C_6 = 0$$

$$C_7 = 0 \tag{210}$$

When Eqs. (208) through (210) are inserted into Eqs. (207), and the results placed in matrix form

$$\delta x = [1 \ \sin \tau \ \cos \tau \ \sin 2\tau \ \cos 2\tau \ \tau \ \sin \tau \ \tau \ \cos \tau]
\begin{bmatrix}
-3e \sin \tau_p & -\frac{1}{2}e \cos \tau_p & 0 \\
0 & 6e \sin \tau_p & 0 \\
6e \sin \tau_p & -\frac{3}{2}e \sin \tau_p & 0 \\
3e \cos \tau_p & -\frac{3}{2}e \sin \tau_p & 0 \\
-3e \sin \tau_p & -\frac{3}{2}e \cos \tau_p & 0 \\
-3e \cos \tau_p & -3e \sin \tau_p & 0 \\
-3e \sin \tau_p & 0 & 0 \\
-3e \cos \tau_p & 0 & 0
\end{bmatrix}
\begin{Bmatrix}
x_0' \\
y_0' \\
z_0'
\end{Bmatrix}$$

$$= \qquad [\phi] \qquad\qquad [AE] \qquad\qquad |X_0'|$$

$$\tag{211a}$$

$$\delta y = [\phi] \begin{bmatrix} -4e\cos\tau_p & -3e\sin\tau_p & 0 \\ -e\sin\tau_p & -2e\cos\tau_p & 0 \\ 2e\cos\tau_p & 4e\sin\tau_p & 0 \\ 2e\sin\tau_p & e\cos\tau_p & 0 \\ 2e\cos\tau_p & -e\sin\tau_p & 0 \\ 0 & 0 & 0 \\ -3e\cos\tau_p & 0 & 0 \\ -3e\sin\tau_p & 0 & 0 \end{bmatrix} \begin{Bmatrix} x_o' \\ y_o' \\ z_o' \end{Bmatrix}$$

$$= [\phi] \qquad [BE] \qquad\qquad \left| X_o' \right| \qquad\qquad (211b)$$

$$\delta z = [\phi] \begin{bmatrix} 0 & 0 & -\frac{3}{2}e\sin\tau_p \\ 0 & 0 & -e\cos\tau_p \\ 0 & 0 & 2e\sin\tau_p \\ 0 & 0 & \frac{1}{2}e\cos\tau_p \\ 0 & 0 & \frac{1}{2}e\sin\tau p \\ 0 & 0 & 0 \\ 0 & 0 & 0 \\ 0 & 0 & 0 \end{bmatrix} \begin{Bmatrix} x_o' \\ y_o' \\ z_o' \end{Bmatrix}$$

$$\qquad\qquad\qquad\qquad\qquad\qquad\qquad\qquad (211c)$$

$$= [\phi]| \qquad [CE] \qquad\qquad \left| X_o' \right|$$

In a more compact form, Eqs. (211) become

$$\begin{Bmatrix} \delta x \\ \delta y \\ \delta y \end{Bmatrix} = \begin{bmatrix} [\phi]\ [AE] \\ [\phi]\ [BE] \\ [\phi]\ [CE] \end{bmatrix} \begin{Bmatrix} x_o' \\ y_o' \\ z_o' \end{Bmatrix} \qquad\qquad (212)$$

Similarly, the Clohessy-Wiltshire equations can be written in the same form

$$
\begin{Bmatrix} x_c \\ y_c \\ z_c \end{Bmatrix} = \begin{bmatrix} [\phi] & [AC] \\ [\phi] & [BC] \\ [\phi] & [CC] \end{bmatrix} \begin{Bmatrix} x_o' \\ y_o' \\ z_o' \end{Bmatrix} \tag{213}
$$

where

$$
[AC] = \begin{bmatrix} 0 & 2 & 0 \\ 4 & 0 & 0 \\ 0 & -2 & 0 \\ 0 & 0 & 0 \\ 0 & 0 & 0 \\ 3 & 0 & 0 \\ 0 & 0 & 0 \\ 0 & 0 & 0 \end{bmatrix} \tag{214a}
$$

$$
[BC] = \begin{bmatrix} -2 & 0 & 0 \\ 0 & 1 & 0 \\ 2 & 0 & 0 \\ 0 & 0 & 0 \\ 0 & 0 & 0 \\ 0 & 0 & 0 \\ 0 & 0 & 0 \\ 0 & 0 & 0 \end{bmatrix} \tag{214b}
$$

$$
[CC] = \begin{bmatrix} 0 & 0 & 0 \\ 0 & 0 & 1 \\ 0 & 0 & 0 \\ 0 & 0 & 0 \\ 0 & 0 & 0 \\ 0 & 0 & 0 \\ 0 & 0 & 0 \\ 0 & 0 & 0 \end{bmatrix} \tag{214c}
$$

137

Combining these two solutions

$$
\begin{Bmatrix} x \\ y \\ z \end{Bmatrix} = \begin{Bmatrix} x_C \\ y_C \\ z_C \end{Bmatrix} + \begin{Bmatrix} \delta x \\ \delta y \\ \delta z \end{Bmatrix} = \begin{bmatrix} [\phi]\ [A] \\ [\phi]\ [B] \\ [\phi]\ [C] \end{bmatrix} \begin{Bmatrix} x_0' \\ y_0' \\ z_0' \end{Bmatrix}
$$

$$
\lvert X \rvert \quad\quad\quad\quad\quad\quad = \quad\quad [M'] \quad\quad \lvert X_0' \rvert
$$

(215)

where

$$
[A] = [AC] + [AE] = \begin{bmatrix}
-3e \sin \tau_p & 2 - \frac{1}{2}\,e \cos \tau_p & 0 \\[4pt]
4 & 6e \sin \tau_p & 0 \\[4pt]
6e \sin \tau_p & -2 + 2e \cos \tau_p & 0 \\[4pt]
3e \cos \tau_p & -\frac{3}{2}\,e \sin \tau_p & 0 \\[4pt]
-3e \sin \tau_p & -\frac{3}{2}\,e \cos \tau_p & 0 \\[4pt]
-3 - 3e \cos \tau_p & -3e \sin \tau_p & 0 \\[4pt]
-3e \sin \tau_p & 0 & 0 \\[4pt]
-3e \cos \tau_p & 0 & 0
\end{bmatrix}
$$

(216a)

$$
[B] = [BC] + [BE] = \begin{bmatrix}
-2 - 4e \cos \tau_p & -3e \sin \tau_p & 0 \\[4pt]
-e \sin \tau_p & 1 - 2e \cos \tau_p & 0 \\[4pt]
2 + 2e \cos \tau_p & 4e \sin \tau_p & 0 \\[4pt]
2e \sin \tau_p & e \cos \tau_p & 0 \\[4pt]
2e \cos \tau_p & -e \sin \tau_p & 0 \\[4pt]
0 & 0 & 0 \\[4pt]
-3e \cos \tau_p & 0 & 0 \\[4pt]
-3e \sin \tau_p & 0 & 0
\end{bmatrix}
$$

(216b)

138

$$[C] = [CC] + [CE] = \begin{bmatrix} 0 & 0 & -\frac{3}{2}e \sin \tau_p \\ 0 & 0 & 1e \cos \tau_p \\ 0 & 0 & 2e \sin \tau_p \\ 0 & 0 & \frac{1}{2}e \cos \tau_p \\ 0 & 0 & -\frac{1}{2}e \sin \tau_p \\ 0 & 0 & 0 \\ 0 & 0 & 0 \\ 0 & 0 & 0 \end{bmatrix} \tag{216c}$$

The volume of a debris cloud

$$V = \frac{4\pi}{3} \det \left| [M'][M']^T \right|^{1/2} \tag{217}$$

This differential correction process is very useful and can be utilized for many other types of perturbations, simply by getting the perturbation in the form of Eq. (211) and adding the 8 x 3 matrices together with the linear solution of Eq. (216).

## 9.3 RESULTS

The effects of location in an elliptic orbit are shown for various values of eccentricity from 0 to 0.25 in Figures 53 through 60. For perigee and apogee breakups, the volume profiles are very similar to a circular case. However, at points halfway between apogee and perigee ($\tau_p$ = 90°, 270°), there is a distinct deviation for different eccentricities. As e approaches 0.25, the analysis deteriorates and produces doubtful results.

## 9.4  CONCLUSIONS

As shown in the results of this analysis, the addition of eccentricity to the initial orbit of a spacecraft prior to orbital breakup has a distinct effect on the evolution of its debris cloud.  For very small changes in eccentricity (from e = 0.01 to e = 0.05), subtle, yet distinctive, characteristics are present.  At apogee and perigee breakups, the half-orbit zero points are the same as the circular case; but when the breakup occurs at some other time, that half-orbit zero point moves away from exactly half an orbit.  Although not obvious for the e = 0.01 case, this half-orbit point shift becomes more apparent as eccentricity increases.  Additionally, as eccentricity reaches 0.25, the assumption that $e^2$ terms are dropped becomes invalid and produces doubtful results.

## Volume vs. Number of Orbits

$\tau_p = 0$
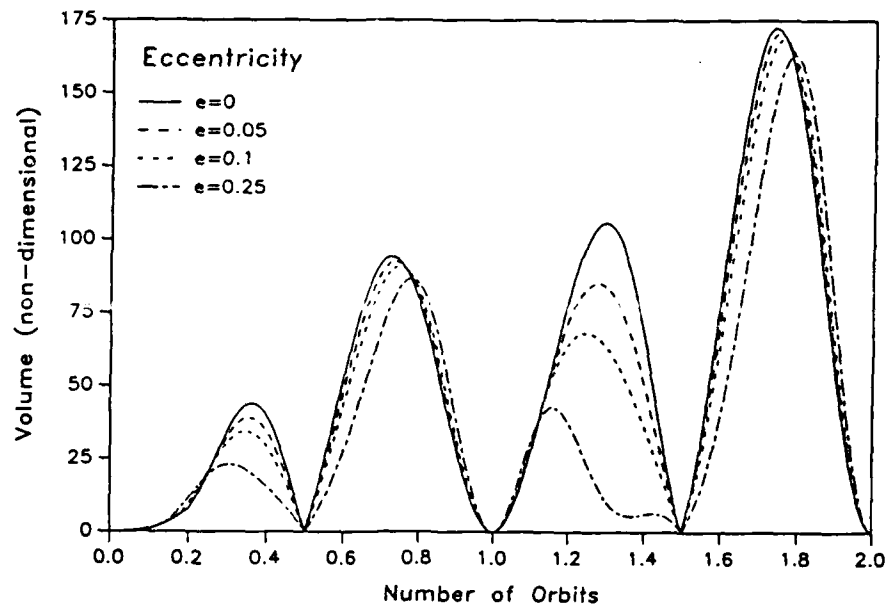


Figure 53. Volume versus Time; $\tau_p = 0°$ (perigee)

## Volume vs. Number of Orbits

$\tau_p = 45$
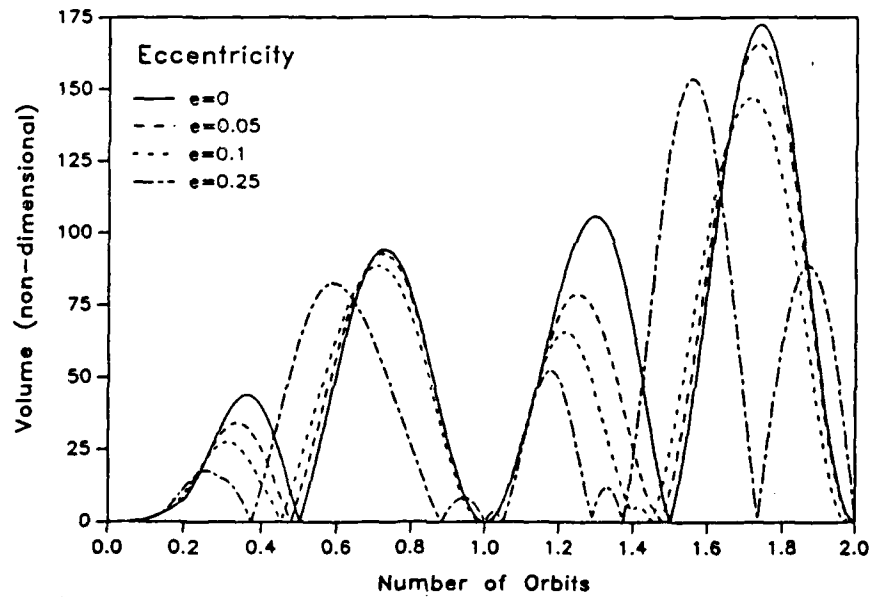


Figure 54. Volume versus Time; $\tau_p = 45°$
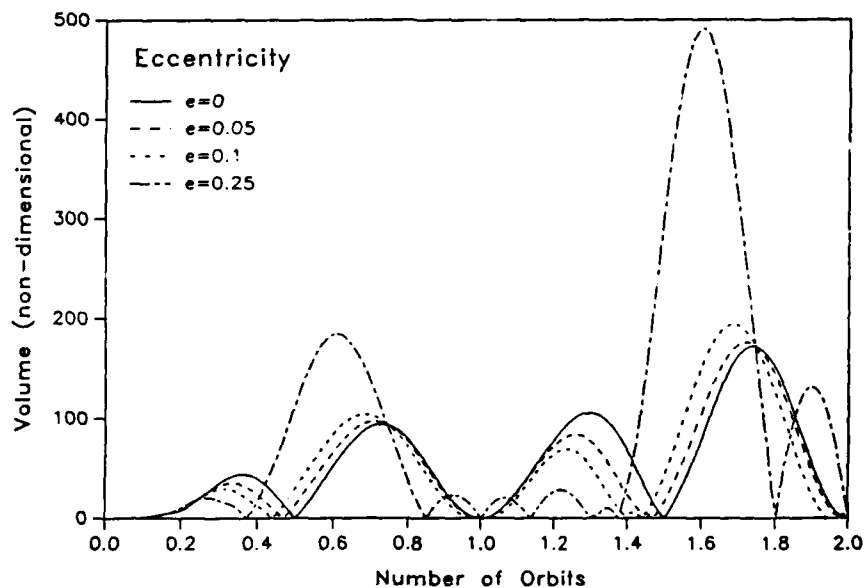
# Volume vs. Number of Orbits

$\tau_p = 90$



Figure 55.   Volume versus Time; $\tau_p = 90°$
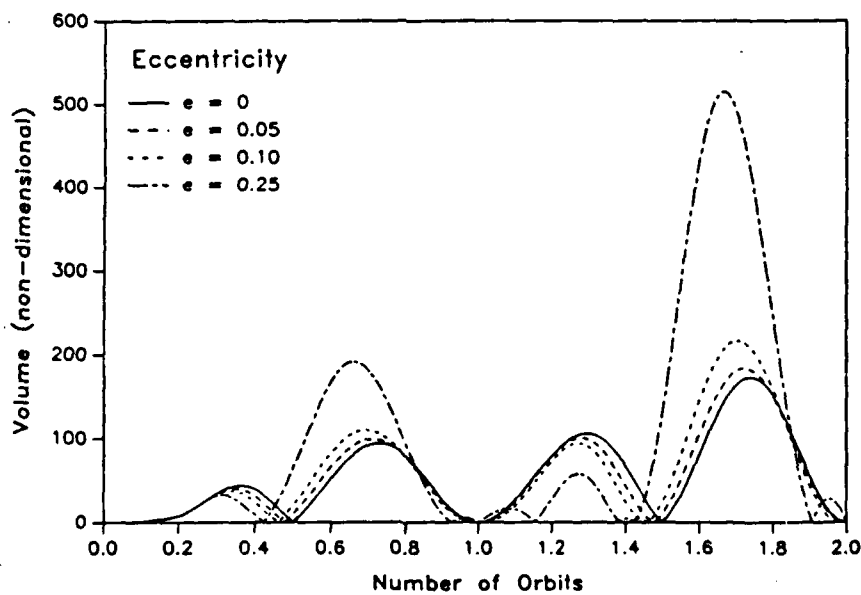
# Volume vs. Number of Orbits

$\tau_p = 135$



Figure 56.   Volume versus Time; $\tau_p = 135°$

# Volume vs. Number of Orbits

$\tau_p = 180$
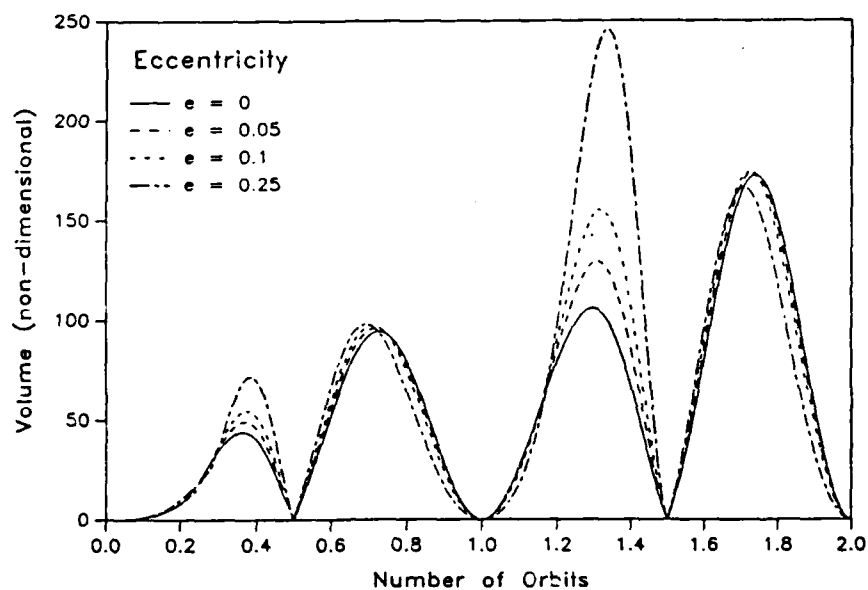


Figure 57. Volume versus Time; $\tau_p = 180°$ (apogee)
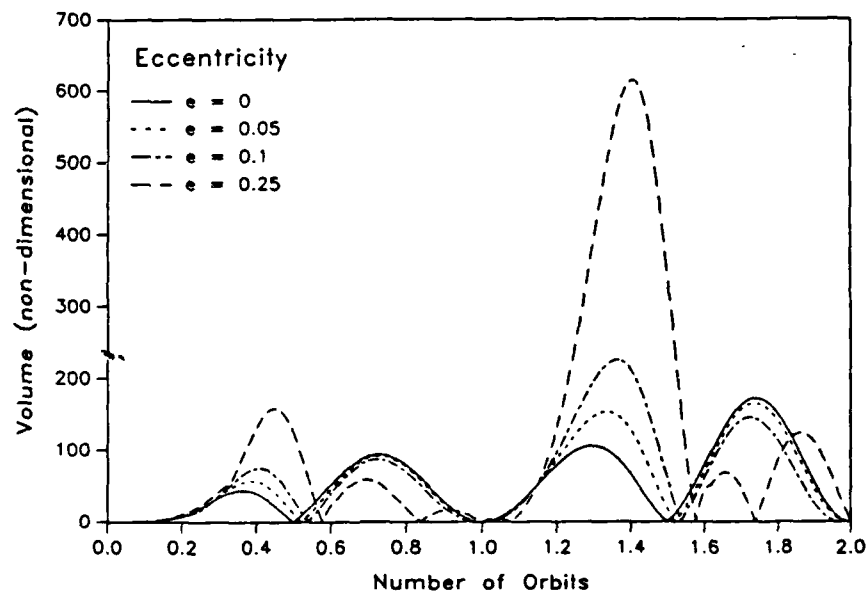
# Volume vs. Number of Orbits

$\tau_p = 225$



Figure 58. Volume versus Time; $\tau_p = 225°$
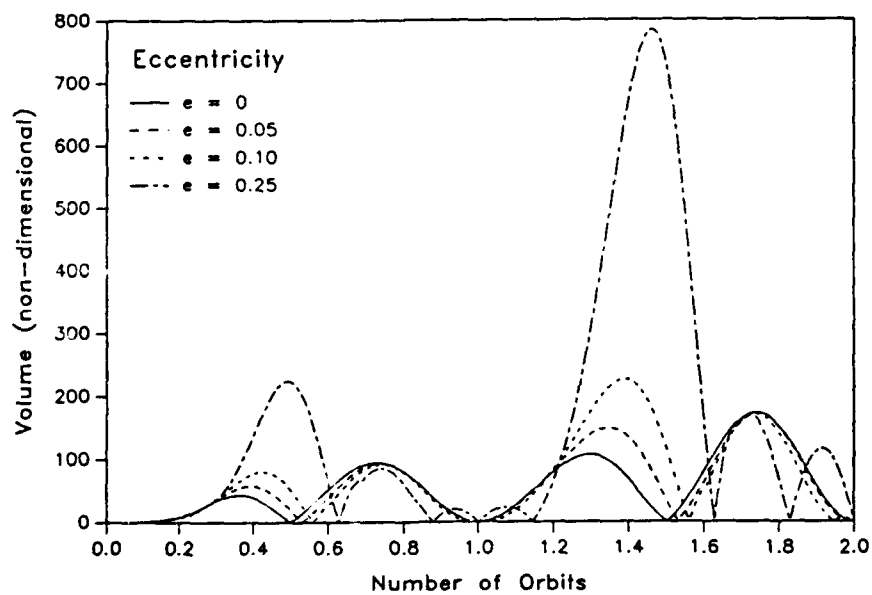
## Volume vs. Number of Orbits

$$\tau_p = 270$$



Figure 59. Volume versus Time; $\tau_p = 270°$

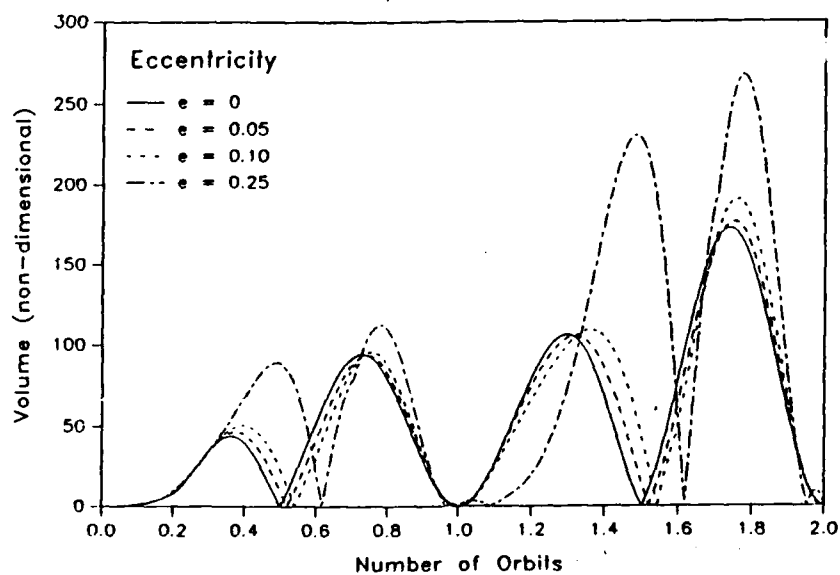## Volume vs. Number of Orbits

$$\tau_p = 315$$



Figure 60. Volume versus Time; $\tau_p = 315°$

## APPENDIX A
## DEBRIS CLOUD VOLUME AS A FUNCTION OF TIME

The determinant of M in Eq. (4) is the volume of a parallelepiped P in three-dimensional space, when the edges of P are obtained from the rows of M as illustrated in Figure A-1 (Ref. A-1). To show this, suppose that all angles in Figure A-1 are right angles or that the edges of P are perpendicular. Then the volume is

$$\text{VOLUME} = 1_1 \ 1_2 \ 1_3 \qquad (\text{A-1})$$

Since the edges of P are the rows of M (or columns with a different P but the same volume) which are mutually perpendicular, the orthogonality of the matrix M yields

$$M \ M^T = \begin{bmatrix} 1_1^2 & 0 & 0 \\ 0 & 1_2^2 & 0 \\ 0 & 0 & 1_3^2 \end{bmatrix} \qquad (\text{A-2})$$

The $1_1^2$ , $1_2^2$ , $1_3^2$ are the squares of the lengths of the rows, and the zeroes off the diagonal are the result of orthogonality of the rows. Taking determinants

$$\det [M^T M ] = [\det M] [\det M^T]$$

$$= [\det M]^2$$

$$= 1_1^2 \ 1_2^2 \ 1_3^2$$

$$= (\text{VOLUME})^2 \qquad (\text{A-3})$$

If the region is not rectangular, M is not an orthogonal matrix and the volume is no longer the product of edge length. However, a transformation can be found which diagonalizes M; this is analogous to finding the "principal" or orthogonal axes for the system. The corresponding elements of the diagonal
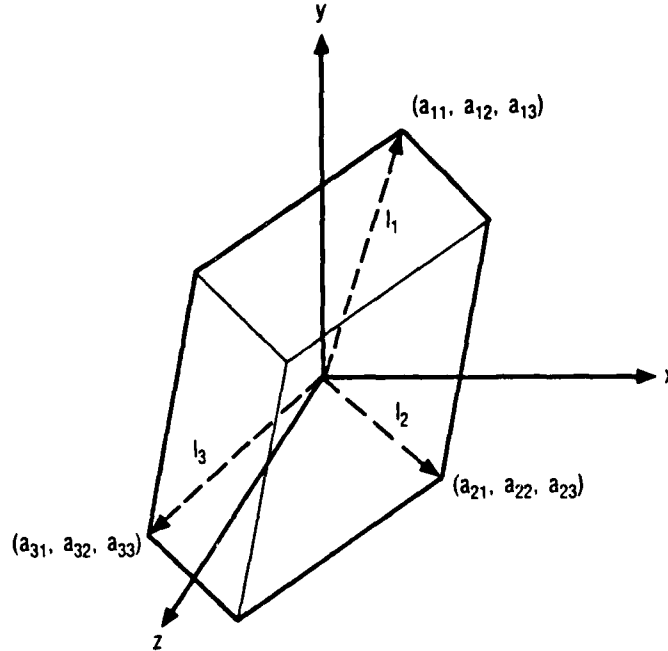
Figure A-1.   Volume of Determinant M

matrix are the required lengths of P.   They can be determined as follows:
find the roots of M by solving the characteristic equation

$$|M - \lambda I| = 0 \tag{A-4}$$

where I is the unit matrix.

For the case in Eq. (5), Section 2, the characteristic equation is of the
form

$$[(a_{11} - \lambda)(a_{22} - \lambda) - a_{12} a_{21}](a_{33} - \lambda) = 0 \tag{A-5}$$

The roots of the characteristic equation are

$$\lambda_1 = a_{33}$$

$$\lambda_{2,3} = \frac{(a_{11} + a_{22}) \pm \left[(a_{11} + a_{22})^2 - 4(a_{11} a_{22} - a_{12} a_{21})\right]^{1/2}}{2}$$

$$\tag{A-6}$$

where the $\lambda_{2,3}$ roots are obtained from the bracketed term in Eq. (A-5). The product of the three roots $\lambda_1$, $\lambda_2$, $\lambda_3$ represents the volume of the cloud. Since the volume is a positive scalar quantity, the product of the roots must be a real positive value. The necessary and sufficient conditions are that

$$\lambda_1 = |a_{33}| \qquad (A-7)$$

and

$$\lambda_2 \cdot \lambda_3 > 0 \qquad (A-8)$$

The second condition can be satisfied if $\lambda_2$ and $\lambda_3$ are complex conjugates (since the product of two conjugate complex systems is positive) or both $\lambda_2$, $\lambda_3$ roots are positive real numbers. Since the roots represent the sides of P, only the condition

$$\lambda_{2,3} > 0 \qquad (A-9)$$

needs to be satisfied. This requires that the terms in the radical satisfy the condition

$$(a_{11} + a_{22})^2 > 4(a_{11} a_{22} - a_{12} a_{21}) \qquad (A-10)$$

or that

$$a_{11} a_{22} - a_{12} a_{21} > 0 \qquad (A-11)$$

In terms of the matrix [Eq. (5), Section 2], it is necessary and sufficient that

$$ad + b^2 > 0 \qquad (A-12)$$

Physically, this means that the area of the cloud in the x,y plane is always finite and positive except at $\theta = 0$, 360°, et cetera, when it is zero. The normalized volume of the cloud is of the form

$$\text{VOLUME} = \frac{4\pi}{3} \det [M] \qquad \text{(A-13)}$$

where

$$\det[M] = |(a_{11} a_{22} - a_{12} a_{21})| \cdot |a_{33}|$$

$$= |(ad + b^2)| \cdot |d|$$

$$= \ell_1 \ell_2 \ell_3$$

Equation (A-13) is the volume of a spheroid with the semi-major axes $\ell_1$, $\ell_2$, $\ell_3$ resulting from the application of a unit velocity impulse to particles with uniform (spherical) distribution in the x,y,z reference frame. By analogy, the area of the cloud in the x,y plane can be expressed as

$$\text{AREA}_{x,y} = \pi \ell_1 \ell_2$$

$$= \pi |ad + b^2| \qquad \text{(A-14)}$$

This is for a circular distribution of the unit velocity impulse in the x,y plane.

UNIFORMLY DISTRIBUTING POINTS ONTO A SPHERE

B.1 INTRODUCTION

In the development of a collision breakup model, a basic problem is to
determine the resulting fragments' directions. In our model, the fragment
directions are chosen randomly from a uniform distribution of directions.
This appendix describes the method for determining the uniform distribution of
directions. These directions are equivalent to points projected onto a
sphere. Uniform distribution then means that all adjacent points on the
sphere are equidistant from one another. The method can be applied to both
collision and explosion models.

Following a description of the method to uniformly spread points onto a
sphere, two examples of its use will be presented using a satellite explosion.
A satellite in an orbit which has a semi-major axis of 4444 nmi is assumed to
explode uniformly, imparting a velocity of 1000 ft/sec on all the fragments.
In the first example, the satellite is in a circular orbit; in the second, it
is in an elliptical orbit. The resulting orbits for each fragment are
computed using the On-Line Orbital Mechanics (OLOM) program.

B.2 ANALYSIS

The method for distributing points uniformly onto a sphere is the same
as that used for constructing geodesic domes. The method starts with the
fifth regular polyhedron (platonic solid): an icosahedron. Convex polyhedra
are considered regular if they have faces that are regular polygons and all
the polyhedral angles are congruent.

An icosahedron has 12 vertices and 20 faces, which are equilateral
triangles (Fig. B-1a). The distance from any vertex to the geometric center
is the same. Hence, if a sphere were circumscribed about an icosahedron, its
geometric centers would coincide and the 12 vertices would all lie on the
surface of the sphere. Since the distances between two adjoining vertices of

a regular polyhedron are equal, it follows that the arc lengths on the surface of the sphere, joining any two adjacent vertices, also are equal. Thus, simply by circumscribing a sphere about an icosahedron, we have found 12 points uniformly distributed on a sphere.

In order to distribute more points about the sphere, first establish the origin of a three-dimensional, rectangular coordinate system at the geometric center of the polyhedron as shown in Figure B-1b (which is Fig. 6 in Ref. B-1). This orientation is for geometrical calculations. Table B-1 lists the coordinates of the 12 vertices of the principal polyhedral triangles (PPT). A PPT is any one of the equal equilateral triangles which forms the face of the regular polyhedron (Ref. B-1).

Table B-1. Coordinates of the PPT's Vertices of an Icosahedron

Vertices: $(0, \pm \sqrt{\tau}/5^{1/4}, \pm 1/5^{1/4} \sqrt{\tau})$

$(\pm 1/5^{1/4} \sqrt{\tau}, 0, \pm \sqrt{\tau}/5^{1/4})$

$(\pm \sqrt{\tau}/5^{1/4}, \pm \sqrt{1}/5^{1/4} \tau, 0)$

where

$$\tau = \frac{1 + \sqrt{5}}{2} = 1.61803$$

$P_1 = (0, \sqrt{\tau}/5^{1/4}, 1/5^{1/4} \sqrt{\tau}) = (0, 0.85065081, 0.52573111)$

$P_2 = (1/5^{1/4} \sqrt{\tau}, 0, \sqrt{\tau}/5^{1/4}) = (0.52573111, 0, 0.85065081)$

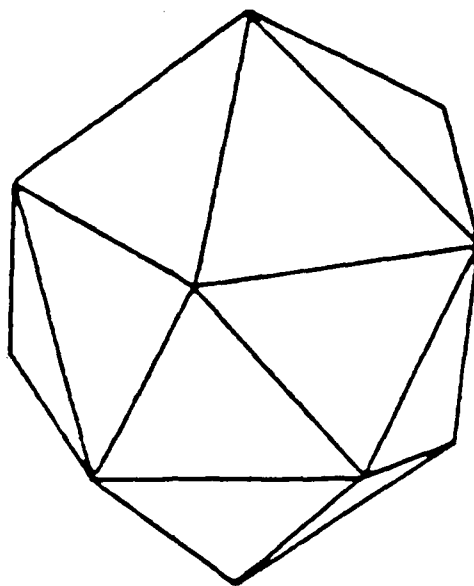$P_3 = (\sqrt{\tau}/5^{1/4}, 1/5^{1/4} \sqrt{\tau}, 0) = (0.85065081, 0.52573111, 0)$
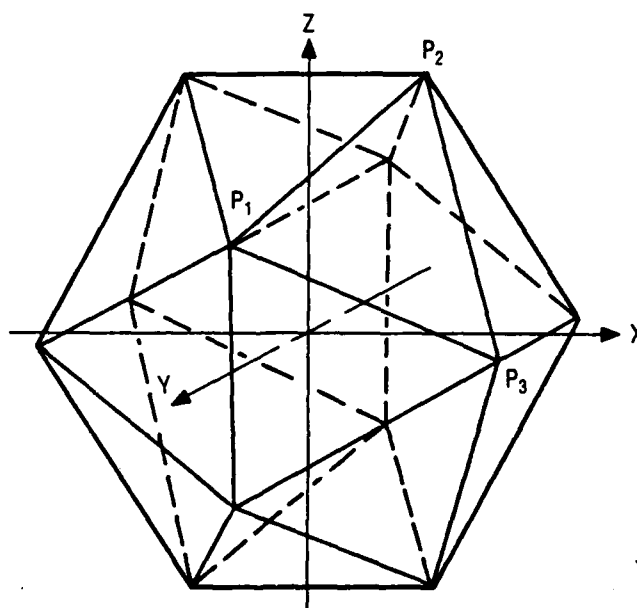
Figure B-1a.  Icosahedron



Figure B-1b.  Three-Dimensional Coordinate System at
the Geometric Center of the Polyhedron

B-3

The next step is to subdivide the PPT into frequency N as shown in
Figure B-2a. The frequency is the number of parts or segments into which a
principal side is subdivided. A principal side is any one of the three sides
of the PPT (Ref. B-1). Figure B-2b shows how each subdivision point is
connected by line segments parallel to their respective sides. A grid of
equilateral subtriangles is generated.

The coordinates of the equilateral subtriangle vertices $(X_{IJ}, Y_{IJ}, Z_{IJ})$ are obtained from Eq. (B-1)

$$X_{IJ} = X_1 + I \frac{X_2 - X_1}{N} + J \frac{X_3 - X_2}{N}$$

$$Y_{IJ} = Y_1 + I \frac{Y_2 - Y_1}{N} + J \frac{Y_3 - Y_2}{N}$$

$$Z_{IJ} = Z_1 + I \frac{Z_2 - Z_1}{N} + J \frac{Z_3 - Z_2}{N} \qquad (B-1)$$

where N is the frequency, $(X_1, Y_1, Z_1)$ $(X_2, Y_2, Z_2)$ $(X_3, Y_3, Z_3)$ are the
coordinates of the PPT vertices, and I and J are integers such that $0 \leq J$
$\leq I \leq N$ (Ref. B-2). The I and J have unique values for each vertex; they
label each vertex as shown in Figure B-3 (which is Fig. 10 in Ref. B-3).

For the purposes of this study, it is necessary only to calculate each
vertex direction from the origin and not the vertex distance from the origin.
This is calculated by doing a coordinate transformation from rectangular to
spherical coordinates for each subtriangle vertex of each PPT. The resulting
spherical coordinates of each vertex direction $(\theta, \phi)$ represent the direc-
tions in which $\Delta v$'s are applied for each particle of the exploded satellite.
These coordinates, along with specified orbital parameters and a specified
$\Delta v$, are input to OLOM. Orbital parameters are computed for each particle
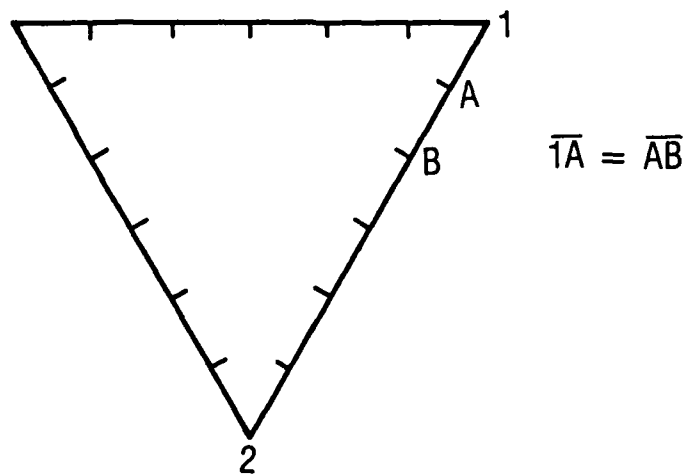from the exploded satellite.

$$\overline{1A} = \overline{AB}$$

Figure B-2a. Subdivided PPT into Frequency N

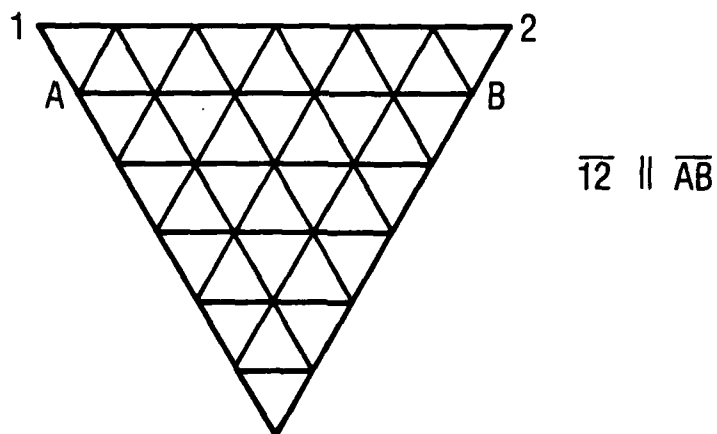

$$\overline{12} \parallel \overline{AB}$$

Figure B-2b. Grid of Equilateral Subtriangles in PPT

## B.3 EXAMPLE 1

In this example, the satellite is assumed to be in a circular orbit with a 1000-nmi (a = 4444 nmi) altitude. The inclination is 28.5°, and the satellite is at its southernmost point when it explodes. The Δv applied to each particle from the explosion is 1000 ft/sec. A frequency of N equal to 7 is used to generate the particles.

One interesting result is obtained by graphing each particle's resulting apogee and perigee against its period (Fig. B-4). This result was originally demonstrated by John Gabbard (Ref. B-3). Figure B-4 has two wings that meet at a point. The upper wing shows the fragment apogees plotted against their periods, and the lower wing shows the perigees versus the periods. Two points are plotted for each fragment. Note, also, the uniform distribution of particles in this figure.

To calculate the number of particles generated by this method, recall that an icosahedron has 12 vertices, 20 faces, and 30 edges. If a PPT is subdivided into frequency N, then the number of particles (NP) generated is

$$NP = 12 + 20 \sum_{i=1}^{N-2} i + 30(N - 1) \qquad (B-2)$$

Thus, for N = 7, NP = $12 + 20 \sum_{i=1}^{5} i + (30 \times 6)$ = 492 particles are generated. However, since Figure B-4 plots apogee and perigee versus period for each particle from the explosion, Figure B-4 has 984 points plotted.

In order to more fully understand the relation between the location of a point on the curve and the actual direction of the Δv that generated that point, Δv's of 1000 ft/sec were applied in 10° increments in three orthogonal planes. The planes are the yaw, pitch, and roll planes shown in Figure B-5. The yaw plane is defined by the velocity vector $\vec{V}$ and the momentum vector $\vec{r} \times \vec{V}$. The pitch plane is defined by the radius $\vec{r}$ and velocity $\vec{V}$ vectors. The roll plane is perpendicular to the other two planes.
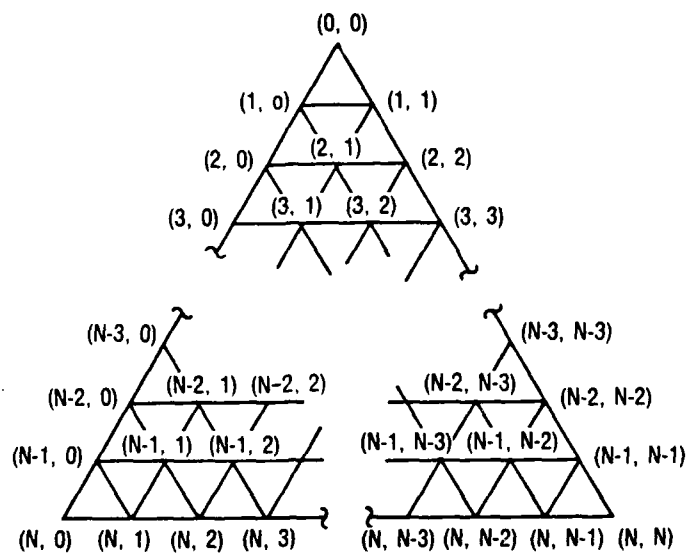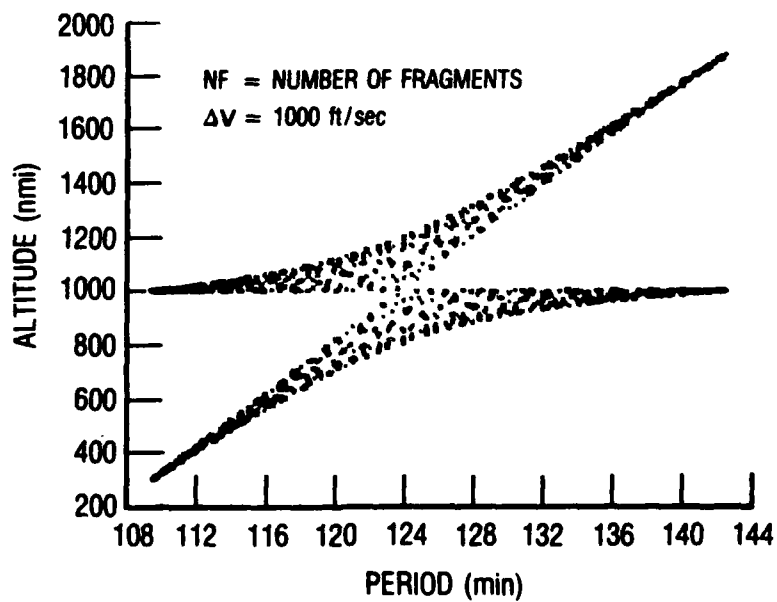
Figure B-3.   Breakdown Numbering



Figure B-4.   Fragment Apogees and Perigees versus Their
Periods from a Satellite Exploding Uniformly
(A = 4444 nmi; ECC = 0; NF = 492)

Figure B-5 also shows that the 0° direction in both the yaw and pitch planes is in the $\vec{V}$ direction. The 0° direction for the roll plane is in the $-\vec{r}$ x $\vec{V}$ direction. For both the roll and pitch planes, the 90° direction is the $\vec{r}$ direction, and for the yaw plane it is the $-\vec{r}$ x $\vec{V}$ direction.

Figure B-6 shows the resulting apogees and perigees from a 1000 ft/sec Δv applied in 10° increments in the three orthogonal planes shown in Figure B-5. Notice first that the results in both the yaw and pitch planes are symmetric about 180°; the results are the same, for example, whether the angle is 130° or -130°. The roll plane is symmetric about 90° and 180°; the results are the same, for example, whether the angle is 50°, -50°, 130°, or -130°.

Also note that, as expected, the Δv applied in the $\vec{V}$ direction (yaw and pitch direction is 0°) yields the highest energy orbit. When the Δv is applied solely in the roll plane, the resulting orbit period is nearly that of the parent body.

The final point is made by comparing Figures B-4 and B-6. The outline in Figure B-4 that contains all points is the same outline in Figure B-6 that was produced from a Δv applied in the yaw and pitch planes. The thickness of the outline is determined in the roll plane. Thus, an idea of the pitch, yaw, and roll angles of the applied Δv can be determined for any specific point in Figure B-4.

## B.4 EXAMPLE 2

The assumptions in this example are the same as those in the first, except that this orbit has an eccentricity equal to 0.05. The semi-major axis is 4444 nmi, the inclination is 28.5°. The Δv applied to each particle from the explosion is 1000 ft/sec. Finally, the frequency used to distribute the particles is 7.
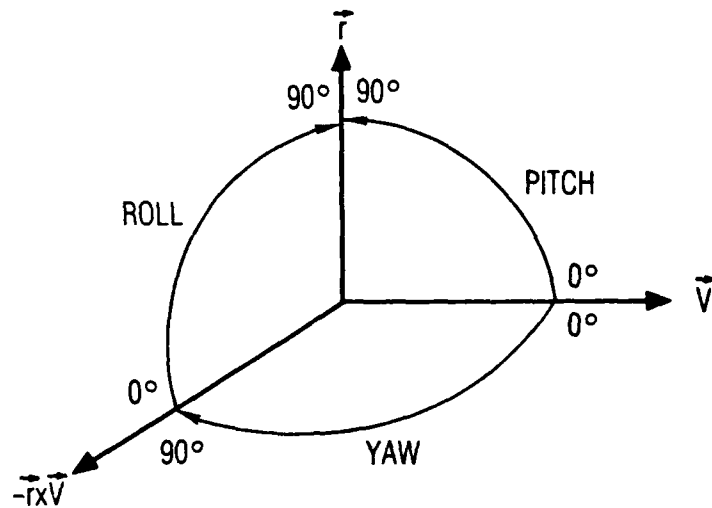
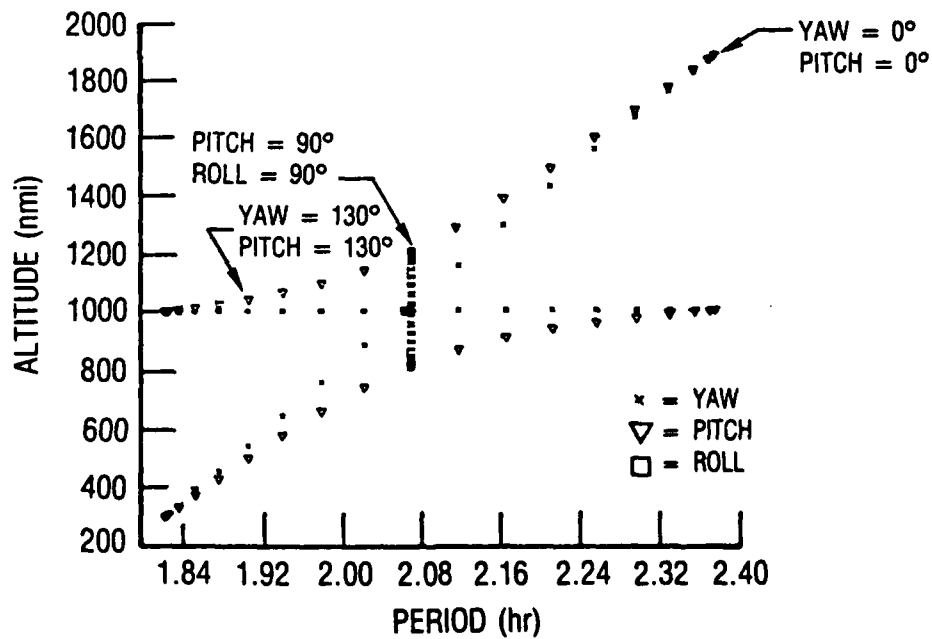Figure B-5.   Angles in Three Orthogonal Planes



Figure B-6.   Apogees and Perigees versus Period for Δv = 1000 ft/sec
Applied in Three Orthogonal Planes to an Object in
1000 nmi Circular Orbit

Figures B-7 and B-8 show the resulting apogees and perigees of the exploded fragments versus their periods at two positions in the orbit. Figure B-7 shows the resulting altitudes if the explosion occurs at perigee (h = 778 nmi), while Figure B-8 shows the altitudes if the explosion occurs at apogee (h = 1222 nmi).

An interesting observation can be made by comparing the two figures. Figure B-7 shows that the altitude range of the fragment perigees (resulting from the explosion at perigee) varies from 490 to 778 nmi. Figure B-8 shows that the altitude range of fragment perigees (resulting from the explosion at apogee) varies from 100 to 1222 nmi. The median perigee altitude for both cases is near 650 nmi. The observation to be made is that the perigee altitudes go much lower in Figure B-8 than in Figure B-7. Thus, some of the particles in Figure B-8 will reenter the atmosphere relatively quickly, whereas no particles will reenter quickly in Figure B-7. Therefore, from a debris hazards standpoint, if a satellite is to be exploded in orbit, a case can be made for exploding it at apogee rather than perigee.

## B.5 SUMMARY

This appendix presents a geometric method for uniformly distributing points onto a sphere. Two applications of its use are presented using a satellite explosion. The first application is a satellite explosion in a circular orbit, and the second is an explosion in an elliptical orbit. Graphs are presented showing the apogees and perigees of the resulting fragments versus their periods.
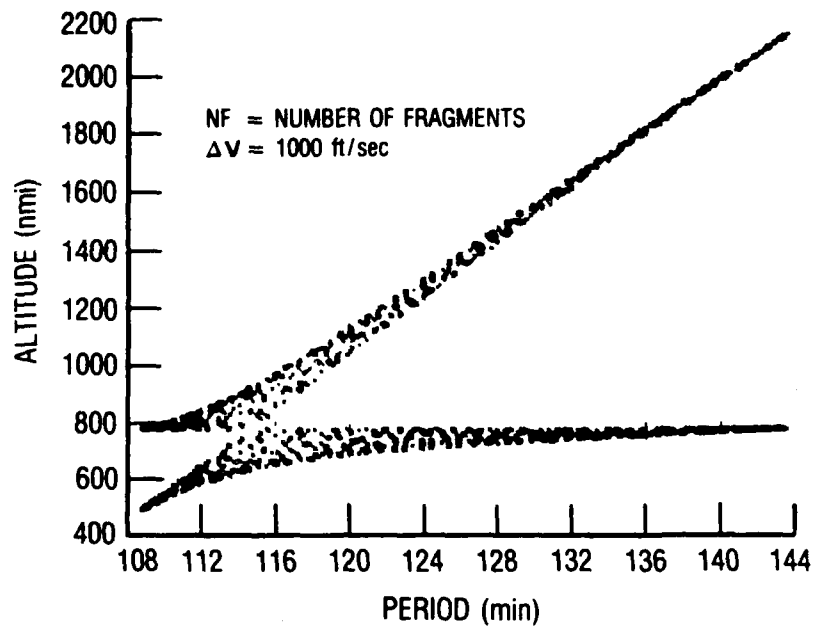
Figure B-7.  Fragment Apogees and Perigees versus Their Periods
from a Satellite Exploding Uniformly at its
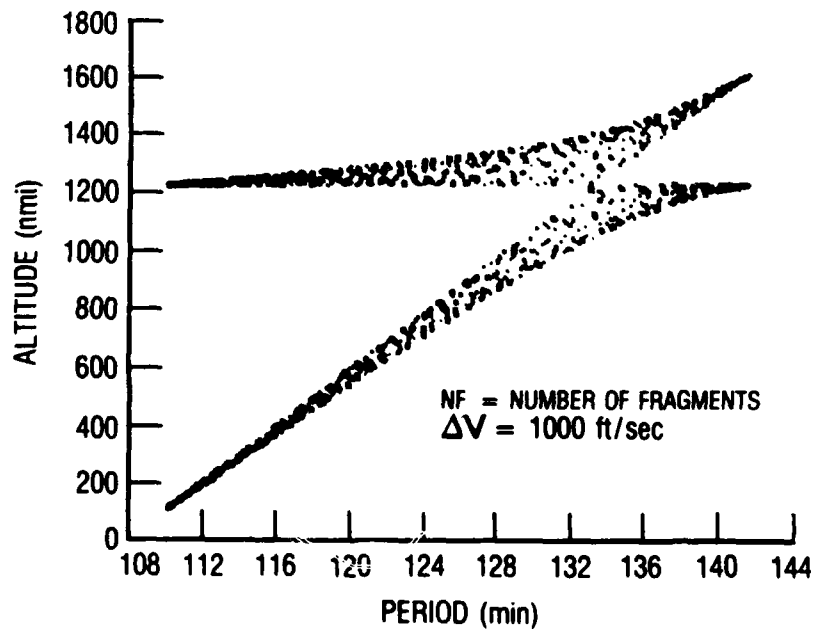Perigee (A = 4444 nmi; ECC = 0.05; NF = 492)



Figure B-8.  Fragment Apogees and Perigees versus Their Periods
from a Satellite Exploding Uniformly at its
Apogee (A = 4444 nmi; ECC = 0.05; NF = 492)

# REFERENCES

1. Kessler, D. J. and Cour-Palais, B. G., "Collision Frequency of Artificial Satellites: The Creation of a Debris Belt," Journal of Geophysical Research, Vol. 83, No. A6, 1 June 1978, p. 2637.

2. Chobotov, V. A., "The Collision Hazard in Space," Journal of Astronautical Sciences, Vol. XXX, No. 3, July–September 1982, p. 191.

3. Chobotov, V. A., "Classification of Orbits with Regard to Collision Hazard in Space," Journal of Spacecraft, Vol. 20, No. 5, September–October 1983, pp. 484–490.

4. Dasenbrock, R., Kaufman, B. and Heard, W., "Dynamics of Satellite Disintegration," Naval Research Laboratory Report 7954, 30 January 1976.

5. Eggleston, J. M., and Beck, M. D., "A Study of the Positions and Velocities of a Space Station and Ferry Vehicle During Rendezvous and Return," NASA TR-87, Langley Research Center, Langley, VA, 1961.

6. Nebolsine, P. E., Lord, G. W., and Leguer, H.H., "Debris Characterization," PSI TR-399, December 1983.

7. Karrenberg, H. K., Levin, E., and Lewis, D. H., "Variation of Satellite Position with Uncertainties in the Mean Atmospheric Density," presented at the National IAS/ARS Joint Meeting, Los Angeles, CA, 13–16 June 1961.

8. Henry, I. G., "Lifetimes of Artificial Satellites of the Earth," Jet Propulsion, Volume 27, No. 1, January 1957, pp. 21–27.

9. Greenwood, D. T., Principles of Dynamics, p. 135, 1965.

10. Miyamoto, J. Y., "On-Line Orbital Mechanics (OLOM) An APL Version," Aerospace Report No. TOR-0078(3317)-2, The Aerospace Corporation, El Segundo, CA, 16 June 1978.

11. Miyamoto, J. Y., "EZPLOT User's Manual," (pending publication).

12. Steffan, K. F., "PECOS2 – Parametric Examination of the Cost of Orbit Sustenance," Aerospace Report No. TOR-1001(2107-60)-1, Revision 1, The Aerospace Corporation, El Segundo, CA, 30 November 1967.

13. Nebolsine, P. E., et al., "Test Report 1, Kinetic Energy Mechanisms Program (U)," Physical Sciences Inc., Woburn, MA, TR-178, June 1979 (SECRET).

14.* Hast, S. L. "Analysis of Satellite Debris," ATM-86(6423-02)-8, The Aerospace Corporation, El Segundo, CA (SECRET).

---

*Aerospace internal correspondence. Not available for external distribution.

REFERENCES (Continued)

15. "HOE Final Report Volume 3 (U)," Lockheed LSMC-L066288, 31 December 1984 (SECRET).

16. Kusper, R. L. and Young, N. A., "Delta-180 Collision and Fragmentation Analysis (U)," Xontech, Inc., Report Number 84359-87-1389, July 1987 (SECRET).

17. Kreyenhagen, K. N., and Zernow, L., "Penetration of Thin Plates," Proceedings of the Fifth Symnposium on Hypervelocity Impact, Vol. I, Part 2, Denver, CO, 31 October and 1 November 1961.

18. Su, S. Y. and Kessler, D. J., "Contribution of Explosion and Future Collision Fragments to the Orbital Debris Environment," Advance Space Rev., Vol. 5, No. 2, 1985.

19. "Delta-180 Program On-Orbit Safety Analysis Report (U)," (Draft), JHU/APL XZX-86-006, 30 July 1986 (SECRET).

20. Knapp, D. T., Presentation to the USAF Scientific Advisory Board, Washington, D.C., 8 July 1986.

21. "Current and Potential Technology to Protect Air Force Space Missions from Current and Future Debris," Report of the USAF Scientific Advisory Board, December 1987.

22. Kennedy, E. C., "Approximation Formulas for Elliptic Integrals," The American Mathematical Monthly, Vol. 61, No. 8, 1954, pp. 613-619.

23. Karrenberg, H. K., Discussion and Extension of "An Exact and a New First-Order Solution for the Relative Trajectories of a Probe Ejected from a Space Station."

24. Anthony, M. L., and Sasaki, F. T., "Rendezvous Problem for Nearly Circular Orbits," AIAA J., Vol. 3, 1666-1673, 1965.

A-1. Strang, G., Linear Algebra and Its Applications, New York, Academic Press, 1980.

B-1. Clinton, J. D., "Advanced Structural Geometry Studies, Part I - Polyhedral Subdivision Concepts for Structural Applications," NASA CR-1734, September 1971.

B-2. Nayfeh, A. H., and Hefzy, M. S., "Geometric Modeling and Analysis of Large Latticed Surfaces," NASA CR-3156, April 1980.

B-3. Gabbard, J. R., "The Explosion of Satellite 10704 and Other Delta Second Stage Rockets," Technical Memorandum 81-5, Directorate of Analysis NORAD/ADCOM, May 1981.